Development and Phenotypic Characterisation of a CRISPR/Cas9 Model of Riboflavin Transporter Deficiency in Zebrafish

Catherine Choueiri

Thesis submitted to the University of Ottawa in partial fulfillment of the requirements for the Master's degree in Science, specialising in Human and Molecular Genetics

Department of Cellular and Molecular Medicine
Faculty of Medicine
University of Ottawa

Abstract

Riboflavin transport is mediated, in part, by riboflavin transporter proteins 2 and 3, encoded by *SLC52A2* and *SLC52A3*, respectively. Biallelic mutations in *SLC52A2* and *SLC52A3* impair riboflavin transporter protein function and riboflavin transport, causing disruptions to mitochondrial metabolism which result in sensory and motor neurodegeneration and give rise to riboflavin transporter deficiency (RTD) in humans. RTD is a rare neurodegenerative disease characterised by respiratory compromise, muscle and limb weakness, and vision and hearing impairments. RTD patients are treated with high-dose riboflavin supplementation which is effective in over 70% of cases but can be ineffective due to rapid excretion of riboflavin when its plasma concentration exceeds 0.5 μM. To address the need for alternative or supplemental RTD treatment, this study generated morpholino-mediated knockdown and CRISPR/Cas9 models of RTD in zebrafish. An RTD-like phenotype is observed in these RTD models including hearing loss, decreased motor axon length, and impaired locomotor activity. The *slc52a3* morphant phenotype was found to be specific via coinjection of *slc52a3* morpholino/human *SLC52A3* mRNA, which achieved effective rescue of the morphant phenotype, as well as *slc52a3* morpholino/*p53* morpholino coinjection, which maintains the *slc52a3* morphant phenotype. In line with clinical findings, riboflavin supplementation resulted in some improvement of the morphant phenotype. Probenecid was selected as a candidate drug due to its inhibitory effect on OAT-3, which mediates riboflavin excretion. However, supplementing riboflavin treatment with probenecid provided no additional benefit to the *slc52a3* knockdown model. Further development of CRISPR/Cas9-knockout lines of *slc52a2* and *slc52a3*, as well continued therapeutic screening of riboflavin and probenecid and consideration of alternative therapeutics will provide more opportunities to uncover novel therapeutic strategies to improve RTD treatment.

Acknowledgements

Firstly, I would like to thank my supervisor, Dr. Hanns Lochmüller, for providing me with the opportunity to conduct this exciting research and for his consistent support throughout all the ups and downs along the journey. Next, I would like to thank Dr. Alex MacKenzie and Dr. Marc Ekker for agreeing to be on my thesis advisory committee and for offering their valuable input at our meetings. Thanks to Dr. Emily O'Connor for her mentorship and for familiarizing me with everything from PCR to zebrafish microinjections. I would also like to extend my appreciation to Jarred Lau for always being a reliable source of knowledge for all things zebrafish-related and beyond. Additionally, I want to thank the Lochmüller lab's research associate Dr. Sally Spendiff and lab technicians Daniel O'Neil and Ricardo Carmona for their hard work keeping the lab running smoothly behind the scenes. I would like to express my gratitude to the rest of the Lochmüller lab for also being a part of such an encouraging team: Dr. Alberto Aleman, Alexa Derksen, Dr. Amanda Yaworski, Emilie Hill-Smith, Dr. Emily Freeman, Dr. Erin Beattie, Dr. Hugh McMillan, Isabelle Fisette-Paulhus, James Davis, Jessica MacGregor, Josh Zeldin, Kaela O'Connor, Kelly Ho, Dr. Kiran Polavarapu, Laura Thompson, Liz Duff, Malaichamy Sivasankar, Dr. Marc-Olivier Deguise, Miriam Maisababi, Ofosu Adjei-Afriyie, Ozge Aksel-Kilicarslan, Rohan Ray, Dr. Romane Idoux, Stephen Holland, and Dr. Rachel Thompson. I want to give thanks to everybody else at the Children's Hospital of Eastern Ontario Research Institute who works tirelessly to assist us in our research efforts. Thanks to my friends and family for their endless support and belief in me during this process.

Table of Contents

List of Tables

List of Figures

List of Abbreviations

ACVS	Animal Care and Veterinary Services
BSA	Bovine serum albumin
cDNA	Complementary DNA
CNS	Central nervous system
CSF	Cerebrospinal fluid
d	Diameter
DEPC	Diethyl pyrocarbonate
dH2O	Distilled water
DMEM	Dulbecco's Modified Eagle's Medium
DNA	Deoxyribonucleic acid
dpf	Days post-fertilization
FAD	Flavin adenine dinucleotide
FBS	Fetal bovine serum
FMN	Flavin mononucleotide
gDNA	Genomic DNA
GSH	Reduced glutathione
GSSG	Oxidized glutathione
GR	Glutathione reductase
HEK-293T	Human embryonic kidney 293T cells
HMA	Heteroduplex mobility assay
hpf	Hours post-fertilization
HS	Horse serum
HTT	Huntingtin (human)
Htt	Huntingtin (mouse)
htt	Huntingtin (zebrafish)
iPSCs	Induced pluripotent stem cells
M	Molar
mL	Millilitre
mM	Millimolar
mm	Millimetre
MO	Antisense morpholino oligonucleotide
MTF	Mitochondrial folate transporter
mU	Milliunits
ng	Nanogram
nl	Nanolitre
NMJ	Neuromuscular junction
oat-3	Organic anion transporter 3 (zebrafish)
OAT-1	Organic anion transporter 1 (human)
OAT-3	Organic anion transporter 3 (human)
PBS	Phosphate-buffered saline
PBS-T	Phosphate-buffered saline with Tween detergent
PCR	Polymerase chain reaction
PFA	Paraformaldehyde
pLDDT	Predicted local distance difference test

PTU	N-Phenylthiourea
PANX-1	Pannexin-1 (human)
RFVT1	Riboflavin transporter protein 1
RFVT2	Riboflavin transporter protein 2
RFVT3	Riboflavin transporter protein 3
ROS	Reactive oxygen species
Rpm	Revolutions per minute
RTD	Riboflavin Transporter Deficiency
RTD-2	Riboflavin Transporter Deficiency type 2
RTD-3	Riboflavin Transporter Deficiency type 3
RT-PCR	Reverse transcriptase polymerase chain reaction
rmsd	Root-mean-square deviation
sgRNA	Single-guide RNA
slc22a6l	Solute carrier family 22, member 6l
SLC22A8	Solute carrier family 22, member 8
SLC25A32	Solute carrier family 25, member 32
SLC52A1	Solute carrier family 52, member 1 (human)
SLC52A2	Solute carrier family 52, member 2 (human)
Slc52a2	Solute carrier family 52, member 2 (mouse)
slc52a2	Solute carrier family 52, member 2 (zebrafish)
SLC52A3	Solute carrier family 52, member 3 (human)
Slc52a3	Solute carrier family 52, member 3 (mouse)
slc52a3	Solute carrier family 52, member 3 (zebrafish)
SV2	Mouse synaptic vesicle glycoprotein 2A
tyr	Tyrosinase
v	Volume
α-BT	Alpha bungarotoxin
μg	Microgram
μL	Microlitre
μM	Micromolar
ΔG	Gibbs free energy

1. Introduction

Riboflavin transporter deficiency (RTD) is a rare and progressive neurodegenerative disease caused by mutations in the genes encoding riboflavin transporter proteins. RTD can cause sensorimotor and cranial impairments resulting in sensorineural deafness, muscle weakness, bulbar palsy, and respiratory difficulty due to paralysis of the diaphragm. RTD patients are currently treated with high-dose riboflavin supplementation which has ameliorated symptoms in over 70% of cases. However, some patients do not respond to riboflavin supplementation due to rapid excretion of riboflavin from the body when plasma concentrations exceed 0.5 μM. Therefore, there is a need for an alternative or supplemental treatment to enable the additional retention of riboflavin in the body. This study utilizes antisense morpholino oligonucleotide (MO) knockdown and CRISPR/Cas9 genome editing technologies to develop RTD models in zebrafish for use in therapeutic screening to identify novel therapeutic combinations for this severe disease.

1.1 Riboflavin and Human Health

1.1.1 Functions of Riboflavin

Riboflavin (vitamin-B2) is an essential water-soluble vitamin which plays a multitude of crucial roles throughout the human body. Over evolutionary time, higher-order mammals have lost the ability to synthesize their own riboflavin, meaning the vitamin can now only be obtained through dietary consumption and to a lesser degree, through production by intestinal bacteria[1,2]. Riboflavin can be obtained from a variety of foods as well as dietary supplements[1]. Foods rich in riboflavin include milk and dairy products, meat, fish, and dark green vegetables[3]. In dietary sources, riboflavin exists either in its free form or as one of two derivatives which are biologically active, protein-bound coenzymes: flavin adenine dinucleotide (FAD) and flavin mononucleotide (FMN)[2].

90 genes in the human genome are known to collectively encode the human flavoproteome, comprising flavin-dependent proteins – flavoenzymes – that play different roles in various biological pathways[4]. In addition to aiding in the metabolism of other B vitamins such as folate and vitamin B6, flavoenzymes FAD and FMN are involved in multiple physiological processes, such as the protection of cells against oxidative stress[1,5]. Complex I of the mitochondrial electron transport chain contains FMN and complex II contains FAD[4]. Within these complexes, FAD and FMN act as electron carriers in the redox reactions of mitochondrial metabolism, such as the oxidative decarboxylation of glucose and amino acids, as well as fatty acid β-oxidation[6]. FAD and FMN are therefore crucial for redox homeostasis and oxidative stress control[3,7]. FAD is also a coenzyme for glutathione reductase (GR), an enzyme that catalyzes the conversion of oxidized glutathione (GSSG) to reduced glutathione (GSH)[1,7]. GSH and riboflavin are important free radical scavengers, and the maintenance of an optimal GSH:GSSG ratio is crucial for the protection of cells from the damage inflicted by oxidative stress[1,8]. GR activity is widely used in clinical and research settings as an indicator of riboflavin status in humans and other organisms[3,6,7,9,10].

Furthermore, riboflavin is involved in the modulation of homocysteine, an amino acid by-product of methionine metabolism which can be metabolised by vitamin B6, vitamin B12, or vitamin B2 (riboflavin)[3]. Increased plasma homocysteine concentration has been highlighted as a risk factor for cardiovascular disease[3]. FAD acts as a cofactor for methylenetetrahydrofolate reductase, the enzyme which converts folate into the appropriate form enabling homocysteine methylation and subsequent decrease in homocysteine concentration[3]. Therefore, a lack of FAD can lead to disrupted homocysteine methylation and a resulting increase in homocysteine concentration. Previous work has established riboflavin status as a regulator of homocysteine concentrations in adult humans[3].

In addition, riboflavin helps to increase both the absorption of iron and hemoglobin concentration in the blood[1]. Riboflavin also enhances ferritin – an iron storage protein – mobilization from tissues[1,11]. Previous work has established an association between riboflavin deficiency and anemia risk, and highlighted the potential for increased riboflavin intake to help protect against anemia[12].

1.1.2 Riboflavin Transport

Riboflavin is transported around the body by riboflavin transporter proteins 1-3 (RFVT1-3), which are predicted to be comprised of 10 (RFVT1 and RFVT2) or 11 (RFVT3) transmembrane domains and are encoded by solute carrier family 52, members 1-3 (*SLC52A1-3*), respectively (Fig. 1)[6,13]. *SLC52A1-3* and, in turn, RFVT1-3 are differentially expressed across various tissues[6,14]. First, free riboflavin is absorbed into the small intestine via a saturable process by RFVT3, after which it can either be metabolised into FMN or FAD for use by epithelial cells in the gastrointestinal tract or transported into the bloodstream by either RFVT1 or RFVT2[3,4,14]. From the bloodstream, free riboflavin is then distributed around the body by RFVT1-3, according to the tissue-specific expression of these transporter proteins[14].

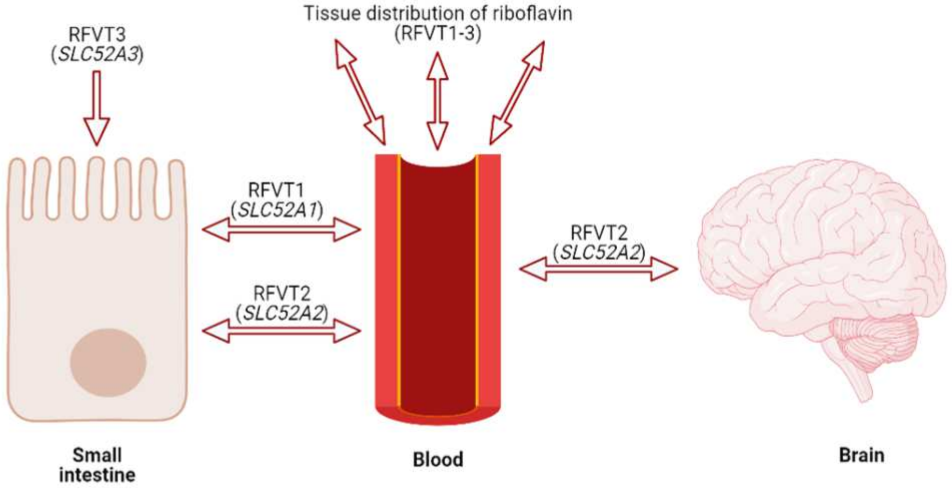

Created with BioRender.com

Figure 1.01 Riboflavin transport throughout the human body. This process is mediated by riboflavin transporters 1-3 (RFVTs 1-3).

While RFVT1 is more highly expressed in the placenta and the small intestine, RFVT2 − although ubiquitously expressed in the body − is predominantly expressed in the brain, endocrine tissues, and liver, and RFVT3 is more highly expressed in the small intestine and the prostate[4,14]. Intracellularly, riboflavin can be phosphorylated into FMN by riboflavin kinase, and FMN can be metabolised into FAD by FAD synthase, after which these derivatives are available to engage in their various roles in the body[1,4]. Within the mitochondria, the mitochondrial folate transporter (MTF) − encoded by solute carrier family 25, member 32 (*SLC25A32*) − transports FMN and FAD[13].

Riboflavin transport to and from the central nervous system (CNS) is mediated by organic anion transporter-3 (OAT-3), a transmembrane transporter protein encoded by solute carrier family 22, member 8 (*SLC22A8*) and located in the choroid plexus, a brain structure of epithelial cells that produce cerebrospinal fluid (CSF) and regulate the secretion of CSF into the ventricles of the brain[15–19]. The epithelial cells comprising the choroid plexus form tight junctions between each other, resulting in the formation of the blood-CSF barrier[15]. Elsewhere, the brain and spinal cord are also infiltrated by capillaries lined with endothelial cells, forming the blood-brain barrier which mediates blood-brain transport of compounds[16]. Together, the blood-CSF barrier and blood-brain barrier maintain homeostasis of the brain microenvironment and separate the CNS from any harmful agents that may exist in the bloodstream[15]. Riboflavin is able to enter the blood-CSF barrier and the blood-brain barrier[20]. In a previous study investigating riboflavin transport in the rabbit CNS, it was found that riboflavin passes from the blood into the CSF via the choroid plexus, and can accumulate in brain cells via a saturable active transport process[20]. Low riboflavin concentration in the plasma stimulates increased riboflavin transport from the plasma into the choroid plexus, CSF, and brain[20]. This system becomes saturated at high plasma riboflavin concentrations, causing less transport of riboflavin into the choroid plexus, CSF, and brain[20]. OAT-3 is also strongly expressed in the renal proximal tubules, where it mediates the excretion of riboflavin into the urine[18].

1.2 Riboflavin Transporter Deficiency

1.2.1 Pathophysiology

Riboflavin transporter deficiency (RTD) arises due to homozygous recessive or compound heterozygous mutations in *SLC52A2* and/or *SLC52A3* causing RTD type 2 and RTD type 3, respectively[6,21]. The disease is extremely rare, with a prevalence of less than 1 in 1,000,000, and age of onset can range from early childhood to adulthood, with 50% of cases arising in early childhood and 95% of cases arising before adulthood[6,13]. Cases are genetically heterogeneous and can arise due to several types of pathogenic mutations including missense, nonsense, single-nucleotide substitution, and frameshift mutations due to nucleotide insertions or deletions[6]. These pathogenic mutations impact the amino acid residues that comprise the C-termini, transmembrane domains, and intracellular and extracellular loops of RFVTs[6]. Mutations in *SLC52A2/3* cause impaired expression and sequestration of RFVT2/3 to the ER, leading to impaired riboflavin absorption and transport throughout the body which usually manifests as an abnormality in FAD and/or FMN plasma levels, but not always an abnormality in riboflavin plasma levels[6,22–24]. As a result, RTD patients can present with symptoms such as muscle weakness, sensorineural hearing loss, bulbar palsy, vision loss due to optic nerve atrophy, sensory ataxia, and respiratory difficulty due to diaphragmatic paralysis[6,25,26]. Typically, most symptoms arise approximately 2 years after the onset of sensorineural hearing loss, which is often the first sign of RTD[6,13,24]. Due to the tissue-specific expression of RFVT2 and RFVT3, some symptoms in the RTD phenotype are more frequently observed in either RTD-2 or RTD-3[6,26]. For example, sensory ataxia and optic atrophy are more commonly observed in RTD-2 patients, while bulbar palsy is more commonly observed in RTD-3 patients[6,26,27]. It has also been observed that while the age of onset of RTD can range from childhood to adulthood, adult-onset RTD cases have exclusively been classed as RTD-3[6,27].

Bulbar palsy in RTD patients has been attributed to neurodegeneration in cranial nerves III, IV, IX, X, and XII, while sensorineural deafness and vision loss have been attributed to neurodegeneration in cranial nerves VIII and II, respectively[6,25]. Neuronal loss has additionally been shown to affect the midbrain, brainstem, cerebellum, and spinal cord of RTD patients[6,25]. RTD-associated neurodegeneration is likely a result of oxidative stress induced by disrupted riboflavin homeostasis in the body[13,28]. Protection against reactive oxygen species (ROS) is dependent on redox homeostasis, which is maintained by antioxidants and antioxidant enzymes[13]. Tissue riboflavin deficiency leads to a decrease of FMN and FAD, disrupting their participation in mitochondrial redox reactions and also preventing FAD-dependent glutathione reductase from scavenging free radicals, thereby increasing oxidative stress[13]. Increased oxidative stress can also impair polymerization of actin microfilaments, neurofilaments, and microtubules in the neural cytoskeletal network and can disrupt axonal growth as shown in studies utilizing RTD patient-derived iPSCs[13,29,30].

The importance of riboflavin derivatives FAD and FMN in fatty acid β-oxidation is reflected in the worsening of oxidative stress in response to RTD-related riboflavin deficiency[13,31]. The combination of increased oxidative stress and impaired free radical scavenging activity contributes towards the disruption of fatty acid β-oxidation[13]. Dysfunctional β-oxidation leads to accumulation of fatty acids which are then targeted by lipid peroxidation, the process by which excess ROS production leads to the oxidation of unsaturated lipids by free radicals[13,32]. Increased lipid peroxidation due to increased fatty acid accumulation can disrupt proper organelle functioning and result in necrosis or apoptosis[13]. Furthermore, the combination of disrupted free-radical scavenging activity and the accumulation of polyunsaturated fatty acids in the membranes of neurons potentially exposes the CNS to oxidative stress-induced injury, which has been shown to play a key role in contributing towards defective neuronal functioning in other neurodegenerative diseases[13].

1.2.2 High-Dose Riboflavin Supplementation

The primary treatment provided to RTD patients is oral high-dose riboflavin supplementation, which has ameliorated symptoms in over 70% of RTD patients as of 2019[4,6]. Patients that do not improve may alternatively demonstrate stabilisation of the disease course, while others are not responsive to this treatment, due to the rapid excretion of riboflavin in the urine by OAT-3 when its concentration in the plasma exceeds 0.5 μM[6,17,27,33]. Riboflavin is well-tolerated at high dosages with minimal side effects, although some gastrointestinal symptoms have been reported[1,4,6,34]. Effective riboflavin dosages typically range from 10-80 mg/kg (body weight)/day, and since prior research has found that riboflavin absorption levels decrease significantly above dosages of 30 mg, it is likely that rapid excretion of the vitamin occurs in most patients[3,6]. To address this limitation, alternative or supplemental treatments are needed to retain riboflavin in the body for a longer duration, thereby allowing it to exert a more beneficial effect on the RTD phenotype in patients.

1.2.3 Current RTD Models

There is currently a limited number of published *in vitro* and *in vivo* RTD models. Two previous studies reprogrammed fibroblasts taken from RTD-2 patients into induced pluripotent stem cells (iPSCs), and then used these iPSCs to derive motor neurons in which to test the effectiveness of various antioxidant drugs on the RTD phenotype[28,35]. These studies led to the identification of antioxidants EPI-743 and N-acetylcysteine as potential therapeutics in RTD due to their beneficial effects on the RTD phenotype in the motor neurons, such as increased neurite length, reduced lipid oxidation, amelioration of calcium dysmetabolism, and reduced mitochondrial damage[28,35]. EPI-743 was able to achieve this on its own, while N-acetylcysteine was able to achieve this effect in conjunction with riboflavin treatment[28,35]. This *in vitro* iPSC model of RTD is advantageous for the purposes of high-throughput therapeutic screening of drugs, as demonstrated by these aforementioned studies[28,35]. However, this *in vitro* model only captures the neuronal RTD phenotype and lacks the complexity of an *in vivo* model, which would allow for a more comprehensive study of multiple facets of the RTD phenotype and its response to treatment.

Previously reported attempts to generate a long-term *in vivo* mouse model of RTD were unsuccessful. Heterozygous *Slc52a2*-mutated embryos were bred to produce *Slc52a2*-knockout mice which were found to be unsuitable for long-term analysis due to early embryonic mortality, while *Slc52a3*-knockout mice demonstrated neonatal lethality[36,37]. Although *Slc52a2*-knockout mice died before any analysis was possible, heterozygous *Slc52a2*-mutant mice exhibited normal body weight and macroscopic appearance for up to 3 weeks following birth, and plasma and tissue riboflavin levels were also comparable to wild-type riboflavin levels[37]. Heterozygous *Slc52a2*-mutant mice can act as a representative model of human heterozygous carriers of RTD-causing mutations who do not exhibit the RTD phenotype[37].

On the other hand, *Slc52a3*-knockout mice were analysed to reveal that most died up to 48 hours following birth due to hyperlipidemia and hypoglycemia – potentially reflective of the crucial role of riboflavin in metabolising fatty acids and carbohydrates[17]. *Slc52a3*-knockout mice also had lower riboflavin levels in the tissues and the plasma, as well as a decreased capacity for riboflavin transport via the placenta, compared to their wild-type littermates[17]. The mortality rate and metabolic disorders observed in the *Slc52a3*-knockout mice were ameliorated by riboflavin supplementation[17]. Another research group used the Cre/Lox technique to generate an intestinal-specific RFVT3 conditional knockout mouse model which survived until 6-12 weeks of age, allowing for the observation of RTD-like symptoms over a longer duration[13]. The conditional knockout mice demonstrated growth retardation, decreased body weight compared to wild-type littermates, hunched backs, and ocular impairments[13]. Although these conditional knockout mice survived for longer than the constitutive *Slc52a3*-knockout mice, RTD affects RFVT2 and/or RFVT3 expression in all tissues expressing these proteins, rather than exclusively in specific tissues. Constitutive knockouts are more representative of the nature of the human disease and may therefore demonstrate a phenotype more representative of human RTD. The same research group has also shown that *Slc52a3*-knockout mice exhibit aberrant development of the cerebral cortex[13].

To address the short lifespan associated with RTD mouse models, an RTD model was developed in fruit fly *Drosophila melanogaster* via knockdown of *SLC52A3* Drosophila homolog *drift* (Drosophila riboflavin transporter), which is ubiquitously expressed in the fruit fly body[38,27]. The knockdown fruit flies exhibited decreased riboflavin levels and decreased activity of electron transport chain complex I[38,27]. As a result, knockdown fruit flies demonstrate altered locomotor activity and 99% of them die by 4 days post-eclosion[38,39]. Treatment with esterified riboflavin derivative riboflavin-5'-lauric acid monoester led to partial rescue of the knockdown phenotype[38,27]. However, a major limitation to the use of invertebrates such as *Drosophila* for modeling RTD is the difference in the anatomy and function of their nervous systems compared to humans, while vertebrate nervous system characteristics share more similarities with humans[40]. Ensuring the comparability of the nervous system between the chosen model organism and humans is crucial when developing a model of a neurodegenerative disease affecting the human body, such as RTD. Therefore, a vertebrate model of RTD would produce findings that are more applicable to humans.

Due to the high mortality rates observed in mouse models of RTD at early developmental timepoints, analyses in these models are limited, and other vertebrate *in vivo* models are needed to enable longer-term study of the RTD phenotype. Given the shortcomings associated with high-dose riboflavin supplementation treatment and the need for alternative or supplemental RTD treatment, the ideal RTD model should also enable high-throughput therapeutic screening which is costly to perform in mice[41].

1.3 Modelling RTD in Zebrafish

Employing zebrafish as a model organism for RTD has the potential to address some of the limitations of previous models. Zebrafish have gained prominence as non-mammalian vertebrate model organisms for the study of human genetic diseases due to a myriad of factors[42]. Firstly, 76-82% of human disease-linked genes have at least one zebrafish ortholog, meaning there are multiple opportunities to model human diseases in zebrafish via manipulation of these disease-linked gene orthologs[42]. In the case of RTD, both human RTD disease genes *SLC52A2* and *SLC52A3* have 1 ortholog each in zebrafish (*slc52a2* and *slc52a3*). Zebrafish are highly fecund and can lay up to 200 eggs per litter, making them a cost-effective model organism enabling large sample sizes for experimental use[42]. These large litter sizes allow for high throughput therapeutic screening which is highly advantageous in the search for new RTD treatments[43]. Additionally, zebrafish embryos are transparent and develop externally, enabling easy determination of survival and easy observation of treatment effects on general morphology and development, even in embryos that do not survive[42]. Zebrafish are also easy to genetically manipulate using various methods including CRISPR/Cas9 and MO microinjection[42,44].

Although more genetically divergent from humans than mice are, it has been shown that in several cases, zebrafish can better cope with genetic manipulation compared to mouse alternatives[42]. For example, previous attempts to create a mouse knockout of huntingtin (*Htt*) – a gene implicated in Huntington's disease – by constitutively knocking out huntingtin (*HTT*) have resulted in embryonic lethality[45]. Conversely, zebrafish *htt* knockouts were successfully grown into adulthood, allowing for in-depth longitudinal study of the *htt* knockout phenotype[45]. The genetic divergence between humans and zebrafish may in fact be an advantage during disease model development, as zebrafish may have a greater number of compensatory mechanisms to better handle the RTD-like phenotype, which could reduce the chances of early mortality previously observed in response to *Slc52a2* and *Slc52a3* knockout in mice[36,37].

Several features of the human RTD phenotype have previously been successfully recapitulated in zebrafish models of other neurological diseases such as amyotrophic lateral sclerosis, congenital core-rod myopathy, and congenital myasthenic syndromes[46–48]. RTD-like characteristics that have been observed in zebrafish models of these diseases include motor axon shortening as a result of neurodegeneration, decreased eye size as a result of optic atrophy, decreased acoustic startle response and otic vesicle area as a result of sensorineural hearing impairment, and altered swimming ability due to muscle weakness[48–54]. Based on analysis of these characteristics, a zebrafish model of RTD can be assessed for its representativeness of the human RTD phenotype.

Generating a model of RTD in zebrafish can be accomplished via antisense morpholino oligonucleotide (MO)-mediated knockdown or CRISPR/Cas9-mediated genome editing technologies, which both present their own advantages and disadvantages when it comes to model development[55]. MOs are single-stranded nucleic acid analogues designed to induce transient knockdown of target gene expression upon microinjection into zebrafish embryos between the 1-4 cell stage[55]. MOs achieve gene knockdown by blocking gene translation or alternatively by binding to splice junctions to block splicing in the pre-mRNA[56]. Aberrant splicing can result in atypical intron inclusion or exon exclusion in the mature mRNA, which can cause a frameshift[56]. This frameshift may bring a premature stop codon in-frame and lead to activation of nonsense-mediated decay of the transcript, thereby silencing gene expression[56]. However, CRISPR/Cas9 genome editing involves direct editing of the DNA sequence targeted by a single-guide RNA (sgRNA) molecule and cleaved by the Cas9 nuclease which binds to the protospacer adjacent motif (PAM) sequence downstream of the sgRNA target[55]. Non-homologous end joining repair occurs following DNA cleavage, generating random insertions and deletions that can lead to frameshift mutations, introduction of a premature stop codon and activation of nonsense-mediated decay[55]. This can ultimately alter target gene expression[55]. A synthetic DNA template can also be included to instead achieve homology-directed repair following DNA cleavage and generate a specific predetermined mutation at a specific location in the genome[55]. The sgRNA/Cas9 complex is microinjected into zebrafish embryos to generate the F0 “crispant” generation which can be grown to sexual maturity and outcrossed with wild-type zebrafish to generate the F1 generation of fish harbouring heterozygous target gene mutations in the germline[55,57]. At this point, sexually mature F1 zebrafish can be bred together to create the F2 generation of homozygous knockouts[44].

MOs efficiently achieve gene knockdown and can cause more severe phenotypes to emerge compared to those observed in CRISPR/Cas9 knockout models, which may be prone to compensatory mechanisms that result in milder phenotypes[55]. However, MOs only achieve transient knockdown lasting a few days as MO is diluted through cell division[55]. MOs can also cause off-target effects on gene expression, including the potential activation of the p53 apoptotic pathway which can be suppressed by microinjection of a p53 MO along with the experimental MO[55]. Conversely, CRISPR/Cas9-mediated knockout zebrafish models are more stable genetic models that can be grown into adulthood and phenotypically analysed over a longer duration, although they are significantly more time-consuming to develop compared to MO knockdowns[55,57]. CRISPR/Cas9 technologies also offer the opportunity to introduce specific mutations within the zebrafish genome[55]. Both methods of genetic manipulation are valuable and worth exploring for the purpose of RTD modelling. MO models can be rapidly developed and analysed to characterise the knockdown phenotype and assess its short-term response to therapeutic intervention while a more stable CRISPR/Cas9 model can be generated to allow for longitudinal analysis of the disease phenotype and its response to treatment.

1.4 Probenecid as a Therapeutic Candidate for RTD

Probenecid [p-(dipropylsulphamoyl) benzoic acid)] is a drug that increases uric acid excretion from the body while simultaneously decreasing the excretion of other drugs by acting as a competitive inhibitor of active transport across the body, including in the brain, kidney, and liver tissues[58]. Probenecid is commonly used to treat gout, which arises from high levels of uric acid in the body[59,60]. OAT-3, the transporter responsible for riboflavin excretion, is inhibited by probenecid to reduce riboflavin excretion and subsequently increase plasma riboflavin concentration[61,62]. This inhibitory effect of probenecid on riboflavin excretion has been previously demonstrated in rats and rabbits, indicating the potential for similar effects in humans[20,62]. Successful inhibition of riboflavin excretion in human RTD patients and prolonged retention of high-dose riboflavin supplementation in the body may have a more beneficial effect on the disease phenotype than treatment with only riboflavin, which could increase the responsiveness of RTD patients to riboflavin treatment. Since no long-term animal model of RTD exists, a zebrafish model which recapitulates the human RTD phenotype will allow for high throughput therapeutic screening of riboflavin and probenecid to identify any potential beneficial effects of probenecid on the RTD-like phenotype in zebrafish. Employing a zebrafish RTD model in therapeutic screening of probenecid and riboflavin can offer insight into the potential effectiveness of probenecid on the human RTD phenotype.

1.5 Rationale

RTD is a rare but severe neurodegenerative disease with detrimental implications on sensorimotor and cranial functioning[6]. Although high-dose riboflavin supplementation has ameliorated the RTD phenotype in over 70% of patients as of 2019, many patients remain riboflavin non-responsive and continue to deteriorate[6,33]. This is because riboflavin absorption is a saturable process which drastically decreases above dosages of 30 mg, and riboflavin is rapidly excreted from the body when its plasma concentration exceeds 0.5 μM[2,3,17]. There is therefore a need for an alternative or supplemental treatment enabling the additional retention of riboflavin in the body, potentially increasing the beneficial effects of high-dose riboflavin supplementation on the RTD phenotype. Previous efforts to model RTD in mice have resulted in embryonic and neonatal lethality, meaning these models do not enable long-term analysis of the RTD phenotype in response to therapeutic intervention and are therefore unsuitable for use in therapeutic screening[36,37]. Alternatively, zebrafish are attractive model organisms in which to study the RTD phenotype due to their cost-effectiveness, ease of genetic manipulation, and high fecundity, which allows for high-throughput therapeutic screening[42,43].

This study employed MO-mediated knockdown and CRISPR/Cas9 genome editing technologies to generate and characterise zebrafish models of RTD including morphant zebrafish and F0 "crispant" zebrafish. MOs were used to create knockdown RTD models in zebrafish for therapeutic screening using various combinations of riboflavin and/or probenecid. Morphant zebrafish were screened for beneficial treatment outcomes, indicated by improvements in RTD-like symptoms previously observed in other zebrafish models of neurological disease.

1.6 Aims

1. Generate a zebrafish model of riboflavin transporter deficiency which recapitulates the human phenotypes resulting from *SLC52A2* and/or *SLC52A3* knockout.
    a. Generate the F0 generation of a CRISPR/Cas9 model individually targeting *slc52a2* and *slc52a3.*
    b. Generate MO-mediated knockdowns of *slc52a2* and/or *slc52a3.*
2. Conduct therapeutic drug screening on *slc52a3* knockdown zebrafish and *slc52a2*/*slc52a3* combined knockdown zebrafish using riboflavin and probenecid.

2. Methods

2.1 SLC52A2/slc52a2, SLC52A3a/slc52a3a, and SLC22A8/slc22a6 Protein Sequence Alignment

Protein sequences for the human and zebrafish protein ortholog pairs (SLC52A2/slc52a2 and SLC52A3a/slc52a3a) were retrieved from Uniprot and aligned using Clustal Omega[63]. Human SLC52A2 (Uniprot accession number: Q9HAB3) was aligned with zebrafish slc52a2 (Uniprot accession number: Q7SXU6), and human SLC52A3a (Uniprot accession number: Q9NQ40-1) was aligned with zebrafish slc52a3a (Uniprot accession number: B0S5Y3). The human protein sequence for OAT-3 (SLC22A8, Uniprot accession number: Q8TCC7) was also aligned with the sequence for its zebrafish protein ortholog, oat-3 (slc22a6, Uniprot accession number: Q6NYN7). Alignments were visualized using Jalview[64].

2.2 Zebrafish Husbandry

Adult zebrafish of the AB strain were grown at a constant pH and temperature of 28°C and were kept on a light-dark cycle (14 hours light, 10 hours dark). The fish were maintained by the University of Ottawa's Animal Care and Veterinary Services (ACVS) and were fed twice a day with pellet food and blood worms. Adult zebrafish were bred according to an Animal Care Committee (ACC)-approved protocol (CHEOb-3169), whereby breeding tanks were set up containing 1 male and 1 female zebrafish per tank, separated by a plastic barrier. A plastic mesh insert was also placed in each breeding tank to allow for egg collection. At the onset of the light cycle, the barrier was removed, and the resulting eggs were collected with a mesh sieve. The eggs were split into groups of no more than 50, and each group was moved to its own petri dish containing embryo media (0.01% methylene blue in system water). According to ACC-approved protocol CHEOe-3170, eggs were microinjected at the 1-4 cell stage with a MO or a combination of MO and mRNA, and at the single-cell stage with a single-guide RNA (sgRNA)/Cas9 complex[44,47]. Embryos were then grown at 28.5°C in a dark incubator until the age of 7 days post-fertilization (dpf) at the latest. Between 1-7 dpf, embryos were euthanised using an ACVS-approved 2-part method of rapid chilling and permanent freezing. Embryos to be euthanised were first rapidly chilled on ice at 0-4°C for 12 hours, followed by permanent freezing of the embryos at -80°C. Embryos that were not yet hatched were dechorionated prior to euthanasia using 10 mg/mL pronase (Sigma), which was directly applied to the embryos and left for 10 minutes. The embryos were then washed by transferring them to three embryo media-filled petri dishes consecutively, leaving them in each dish for 3 minutes.

2.3 Morpholino-Mediated Knockdown of *slc52a2* and/or *slc52a3*

2.3.1 Antisense Morpholino Oligonucleotide Design

2 MOs – one targeting each of the zebrafish RTD disease gene orthologs *slc52a2* and *slc52a3* – were designed by Gene Tools, LLC to be complementary to a splice junction target (*slc52a2*: exon 3/intron 3 junction; *slc52a3*: intron 1/exon 2 junction) in the pre-mRNA, using transcript sequences retrieved from Ensembl (Table 2.1). The MO functions by binding to its target site to block proper splicing which causes exon exclusion and nonsense-mediated decay of the transcript, ultimately resulting in knockdown of gene expression. A standard MO targeting a mutated form of the human beta-globin (*HBB*) gene was also ordered from Gene Tools, LLC and used as a negative control MO throughout this study (Table 2.1)[65,66]. Additionally, a morpholino targeting *p53* expression was ordered from Gene Tools, LLC (Table 2.1). The *p53* MO suppresses the *p53* apoptotic pathway in zebrafish to enable the assessment of phenotypic specificity in morphant zebrafish (Table 2.1)[67]. The reverse complement of each MO sequence was searched on NCBI BLAST to identify potential off-target binding sites in the *Danio rerio* genome assembly GRCz11, and no off-target sites were predicted.

Gene	**MO Sequence (5'→3')**	**Target Junction**	**Transcript I.D.**
slc52a2	ACCTTAGTACGCTCAATTACCTTAG	Exon 3/Intron 3	ENSDART00000045675.7
slc52a3	ATGAACTGGAAGAGATTCATATGCT	Intron 1/Exon 2	ENSDART00000062716.7
HBB	CCTCTTACCTCAGTTACAATTTATA	N/A	N/A
p53	GCGCCATTGCTTTGCAAGAATTG	N/A	N/A

Table 2-1 Antisense morpholino oligonucleotide sequences. Each MO sequence is listed alongside its corresponding target gene, target junction, and transcript I.D. retrieved from Ensembl.

2.3.2 Antisense Morpholino Oligonucleotide Preparation

Diethyl pyrocarbonate (DEPC)-treated water was used to reconstitute MOs from 300 nmol to 3 mM, after which they were stored at -20°C. Injection mixtures of 10 μL each were prepared by diluting the respective MO(s) to a concentration of 0.5 mM using 1x Danieau's buffer (58 mM NaCl, 0.7 mM KCl, 0.4 mM $MgSO_4$*7H2O, 0.6 mM $Ca(Na_3)_2$, 5 mM HEPES buffer), followed by the addition of 0.05% phenol red. To ensure that any precipitate is dissolved prior to the addition of the MO to the injection mixture, the MO solution was heated to 65°C for 10 minutes.

2.3.3 Antisense Morpholino Oligonucleotide Microinjection

Filamented glass capillary tubes (Sutter Instrument Co., #BF100-50-10) and a needle puller (Sutter Instrument Co., Model: P-87; Parameters: Heat=590, Pull = 40, Vel = 50, Time = 150) were used to make micropipettes, which were used to perform embryonic microinjections with a Narishige IM 300 Microinjector. 3 μL of MO injection mixture were loaded into a micropipette, which was then inserted into a micromanipulator. To calibrate the MO dosage, finetipped forceps were used to break the micropipette tip until the desired droplet diameter was obtained. Droplet diameter was measured by injecting the MO into a droplet of mineral oil on a micrometer and visualising the droplet under a Leica MZ75 dissecting microscope. The calculation used to determine the appropriate droplet diameter is as follows:

$$V = \frac{4}{3}\pi r^3$$

Where V is the volume of a sphere in mm^3 and r is the radius of the sphere (mm).

Assume 1 mm^3 = 1µl of MO solution at final concentration (FC) in mM.

Therefore, V mm^3 = V µl per injection

MO molecular weight = MMw = 1 M

$$FC = \frac{MMw}{\left(\frac{1M}{FC}\right)}\ \mathrm{g/L} = \left(\frac{\mathrm{ng}}{\mathrm{nl}}\right) \bullet V\ \mathrm{nl} = \mathrm{ng\ MO\ per\ drop}$$

Once embryos are laid, they were collected and lined up along a microscope slide placed inside a petri dish lid. Under the Leica MZ75 dissecting microscope, each embryo was injected with the chosen dosage of MO in the yolk sac behind the cell mass at the 1-4 cell stage. Following microinjection, embryos were grown at 28.5°C in a dark incubator until needed for behavioural and morphological assays.

2.3.3 RNA Extraction and cDNA Synthesis

Following euthanasia at 3 dpf as described in section 2.2, 20 zebrafish embryos of a given condition were pipetted into a 1.5 mL Eppendorf tube and all the liquid was removed. 600 µL of buffer RLT (RNeasy Mini kit, Qiagen, Germany) was added to the embryos along with a single stainless-steel bead. The tissues were then homogenized by placing the tube into chilled Tissue

Lyser II (Qiagen) tube adaptors, followed by lysis for 2 minutes at 25 Hz. The steel bead was then removed, and RNA was isolated and purified using the RNeasy Plus Mini kit (Qiagen) according to the manufacturer's instructions. The ND-100 Spectrophotometer was then used to measure RNA purity and concentration, and RNA was stored at -80°C until required for use. A cDNA synthesis kit (Applied Biological Materials #G592) was used to make cDNA for reverse transcription-PCR (RT-PCR) using 1 μg of RNA.

2.3.4 Primer Design and RT-PCR

Primer sets were designed in Primer3 using transcript sequences retrieved from Ensembl to detect gene expression/knockdown of zebrafish orthologs *slc52a2* (ENSDART00000045675.7) and *slc52a3* (ENSDART00000062716.7) in wild-type zebrafish harvested from 1-5 dpf, morpholino-injected fish harvested at 3 dpf, and morpholino/mRNA co-injected fish harvested at 3 dpf (Table 2.2). Primers were also designed to profile expression of human *SLC22A8* zebrafish ortholog *slc22a6l* (ENSDART00000077887.6) in zebrafish embryos collected from 1-5 dpf (Table 2.2). The genes used as positive controls for RT-PCR experiments were *ef1α* – a eukaryotic translation elongation factor ubiquitously expressed in zebrafish throughout larval development and into adulthood – and *lsm12b* – a gene stably expressed in the brain and spinal cord of zebrafish up to 1 week post-fertilization (Table 2.2)[68,69]. Primers were searched on NCBI BLAST to identify potential off-target primer binding in the *Danio rerio* genome assembly GRCz11, and no off-target binding was predicted. The MyTaq^{TM} DNA Polymerase kit (Meridian Bioscience) was used for RT-PCR reactions using cDNA harvested from wild-type zebrafish between 1-5 dpf, and 3-day old morpholino-injected fish. RT-PCR reactions were conducted in a thermocycler according to a standard PCR protocol (Table 2.3). RT-PCR products were run on agarose gels to visualize the bands using GelRed nucleic acid stain (Biotium), 6x loading dye (Froggabio), and GeneRuler 1 kb DNA ladder (Thermo Scientific).

Gene	**Forward (5'→ 3')**	**Reverse (5'→ 3')**	**Product size (bp)**	**Annealing temperature (°C)**
slc52a2	GCCATCCACATCATACAAGCG	TCCAGGACAAAATCACTAGAGCA	880	57
slc52a3	CATGTTTTTCCCCAAACGTTCA	GACAGCAGACCCGTGAAGAA	177	58
slc22a6l	CTCAGTGCTGTCTGGTTCTCC	TGAGATGGCCGTCGTCCTA	170	62
ef1α	CTGGAGGCCAGCTCAAACATGG	CTTGCTGTCTCCAGCCACATTAC	387	57-62
lsm12b	GTATTTCAGTGTCGGGAGCCA	CTGGAGGAAGGACATTTCAGAGTC	120	57-62

Table 2-2 Primers used for gene expression/knockdown detection. Each primer set is listed alongside its target gene, product size, and annealing temperature used for RT-PCR.

Step	**Temperature (°C)**	**Time (minutes)**	**Cycles**
Initial denaturation	95	3	1
Denaturation	95	0:15	35
Annealing	(See Table 2-2)	0:15	
Extension	72	0:30	
Final Extension	72	5	1

Table 2-3 Standard PCR protocol.

2.3.5 *p53/slc52a3* morpholino coinjection

To assess the specificity of the *slc52a3* morphant phenotype, sections 2.3.2 and 2.3.3 above were followed to prepare and co-inject the *slc52a3* MO and *p53* MO into each zebrafish embryo. Following microinjection, embryos were grown at 28.5°C in a dark incubator until needed for behavioural and morphological assays.

2.3.5 *SLC52A3* mRNA coinjection for rescue of *slc52a3* morpholino knockdown

2.3.5.1 *SLC52A3* mRNA preparation

An agar stab containing Stbl3 bacteria transformed with a *SLC52A3*-expressing plasmid was purchased from addgene (pDONR221_SLC52A3, plasmid #132181), where it was deposited by the RESOLUTE Consortium. The agar stab was used to streak a kanamycin-resistant (50 μg/mL) LB agar plate. The plate was incubated at 37°C for 16 hours, at which point 3 single colonies were picked and inoculated into 3 separate 5 mL volumes of LB broth with kanamycin (50 μg/mL). The 3 cultures were then incubated at 37°C for 16 hours in a shaking incubator. 2 mL of each culture were used to perform plasmid DNA isolation and purification using the QIAprep Spin Miniprep kit (Qiagen). The ND-100 Spectrophotometer was then used to measure DNA purity and concentration. The purified DNA from each of the 3 cultures was then used to conduct diagnostic digests using a variety of restriction enzymes corresponding to the restriction sites found in the *SLC52A3*-expressing plasmid to confirm that the resulting fragment sizes matched the predicted fragment sizes determined from the plasmid map. The diagnostic digests were run on agarose gels by gel electrophoresis to reveal that all 3 DNA samples demonstrated the same fragment sizes as predicted, therefore validating the plasmid structure. To determine plasmid insert (*SLC52A3*) orientation, *Xba*I (New England Biolabs) and *Sph*I-HF (New England Biolabs) were used to perform a double digest, resulting in fragment sizes that revealed the *SLC52A3* insert was cloned into the plasmid in the reverse orientation. The plasmid map indicating the determined insert orientation is shown in Figure 2.1.

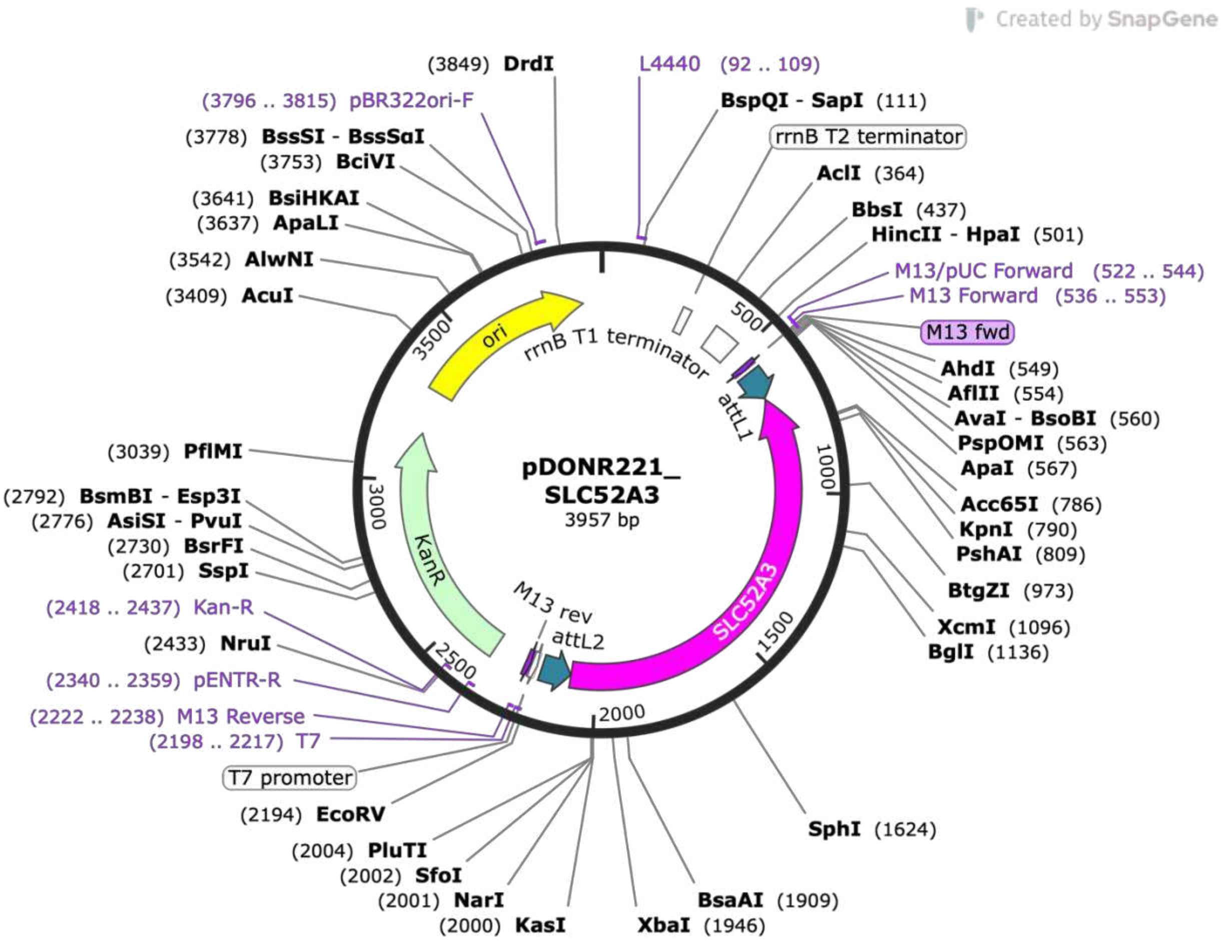

Figure 2.01 Plasmid map of pDONR221_SLC52A3, plasmid #132181. The SLC52A3 insert is shown in the reverse orientation as determined by the diagnostic double digest using *Xba*I and *Sph*I-HF.

Once the plasmid was validated, 1 mL of culture #1 was diluted 1:500 in LB broth with kanamycin (50 µg/mL). 1 mL of this new culture was then inoculated into 249 mL of LB broth with kanamycin (50 µg/mL) and incubated at 37°C for 16 hours in a shaking incubator. The Qiagen Plasmid Midi kit was then used to isolate and purify plasmid DNA. DNA purity and concentration was measured using the ND-100 Spectrophotometer. The plasmid DNA was linearized by performing a restriction digest using *Apa*I (New England Biolabs) and purifying the product using a PCR Purification kit (Qiagen), followed by measurement of DNA purity and concentration using the ND-100 Spectrophotometer. Finally, 1 µg of linearised plasmid DNA was used to perform 4 transcription reactions following the manufacturer's instructions for the mMESSAGE mMACHINE™ T7 Transcription kit (Invitrogen). The resulting capped RNA from all 4 reactions was pooled together and RNA purification was performed using the MEGAclear Transcription Clean-up kit (Invitrogen). The RNA was precipitated using 5 M ammonium acetate and resuspended in 30 µL of nuclease-free water. Measurement of RNA purity and concentration was then performed using the ND-100 Spectrophotometer, and the RNA was stored at -80°C.

2.3.5.2 *SLC52A3* mRNA/*slc52a3* morpholino coinjection

To further assess the specificity of the *slc52a3* morphant phenotype, sections 2.3.2 and 2.3.3 above were followed to prepare and co-inject 8 ng of *slc52a3* MO and 40 ng/µL of full-length *SLC52A3* mRNA into each zebrafish embryo. Following microinjection, embryos were grown at 28.5°C in a dark incubator until needed for behavioural and morphological assays.

2.4 CRISPR/Cas9-mediated mutation of *slc52a2* and/or *slc52a3*

2.4.3 sgRNA Target Site Selection

The online predictor tool CRISPRscan was used to select 4 CRISPR/Cas9 targets each for *slc52a2* and *slc52a3*, searching within the *Danio rerio* genome assembly GRCz11. The chosen targets were synthesized into DNA oligonucleotides for sgRNA synthesis (Table 2-4).

Gene	Target Sequence	Locus	CRISPRscan Score
slc52a2	taatacgactcactataGGGTGCATTGAGAAATCCAAgttttagagctagaa	Chromosome 19: 22338122-22338145	61
slc52a2	taatacgactcactataGGTGTGGTCGCTTTGGGACAgttttagagctagaa	Chromosome 19: 22338158-22338181	59
slc52a2	taatacgactcactataGGGATGGCTGAATGAGCGATgttttagagctagaa	Chromosome 19: 22338417-22338440	72
slc52a2	taatacgactcactataGGTTGGGAATTTGGGACCAGgttttagagctagaa	Chromosome 19: 22338468-22338491	84
slc52a3	taatacgactcactataGGGGGTAAGTCCCAGCCCTCgttttagagctagaa	Chromosome 8: 28469754-28469777	69
slc52a3	taatacgactcactataGGGTCACCAGCAGAGGGCCAgttttagagctagaa	Chromosome 8: 28469807-28469830	67
slc52a3	taatacgactcactataGGTGGTCATTACAGCGAGGAgttttagagctagaa	Chromosome 8: 28470256-28470279	62
slc52a3	taatacgactcactataGGGGCAGACGGTTTAATATGgttttagagctagaa	Chromosome 8: 28470296-28470319	56

Table 2-4 *slc52a2* and *slc52a3* target sequences modified with a 5’ T7 promoter sequence and a 3’ tail annealing sequence. Each target sequence is listed alongside its locus and CRISPRscan score.

Each target sequence was located within a single exon in each gene (*slc52a2*: exon 3, *slc52a3*: exon 1) in an attempt to create larger deletions in both genes[70]. According to CRISPRscan, no off-target effects were predicted for any of the 8 sgRNAs, and all targets had a CRISPRscan score – a rating indicating the predicted *in vivo* editing efficiency of the sgRNA – ranging from 56-84, with higher scores indicating higher predicted efficiency up to 100. Target sequences provided by CRISPRscan were modified prior to ordering by adding a T7 promoter sequence on the 5’ end (5’-TAATACGACTCACTATA-3’) and a tail annealing sequence on the 3’ end (5’-GTTTTAGAGCTAGAA-3’) to create the DNA oligonucleotide. A published target sequence against *tyr*, encoding tyrosinase in zebrafish, was chosen as a positive control for successful sgRNA/Cas9 microinjection[71] (5’-GGACTGGAGGACTTCTGGGG-3’). Tyrosinase mediates pigmentation development in zebrafish and successful CRISPR/Cas9-targeting of the *tyr* gene using the chosen target sequence has previously been shown to result in varying degrees of hypopigmentation in the F0 injected embryos[71]. Finally, a universal bottom strand Ultramer (5′-AAAAGCACCGACTCGGTGCCACTTTTTCAAGTTGATAACGGACTAGCCTTATTTT AACTTGCTATTTCTAGCTCTAAAAC-3′) was also ordered for use in sgRNA synthesis.

2.4.4 sgRNA Synthesis

The 8 modified target sequences for *slc52a2* and *slc52a3,* along with the published *tyr* target sequence and a universal bottom strand Ultramer were ordered as 100 μM DNA oligonucleotides from Integrated DNA Technologies to be used for *in vitro* transcription of 9 sgRNAs (8 total for *slc52a2* and *slc52a3*, 1 for *tyr).* MyTaq (5x) buffer and MyTaq DNA polymerase were used to anneal each target sequence oligonucleotide to the bottom strand Ultramer. To accomplish this, 6 reactions were set up for each of the 8 DNA oligonucleotides, and a specific thermocycler protocol was followed to anneal and extend the oligonucleotides (Table 2-5)[72]. All 6 reactions for each DNA oligonucleotide were then pooled and PCR-purified using the PCR Purification kit (Qiagen), eluting in 30 μL of nuclease-free water. Each PCR-purified product was measured using the ND-100 Spectrophotometer to confirm a minimum yield of 60-100 ng/μL. 2 μL of each PCR-purified product was then run on a 4% agarose gel to confirm the correct product size of 120 bp. The resulting 9 double-stranded DNA templates were then used for *in vitro* transcription of 9 sgRNAs using the MEGAshortscript T7 kit (Invitrogen). 2 transcription reactions for each of the 9 templates were set up using 8 µL of DNA template per reaction and incubated at 37°C overnight. TURBO DNase was added to each reaction, followed by an additional 15 minutes of incubation at 37°C. Each pair of transcription reactions was then pooled together prior to sgRNA purification using the *mir*Vana™ miRNA Isolation Kit (Invitrogen), which was used according to the manufacturer's instructions. The 9 resulting sgRNA samples were measured for using the ND-100 Spectrophotometer, and 2 µL of each sample was run on a 1% agarose gel to identify potential RNA degradation. The sgRNA samples were then stored at -80°C until needed for microinjection.

Temperature (°C)	**Time (minutes)**
95	5
89	0:15
83	0:15
77	0:15
71	0:15
65	0:15
59	0:15
53	0:15
50	10:00
72	10:00
4	∞

Table 2-5 Thermocycler protocol used to anneal target sequences to Ultramer bottom strand sequence.

2.4.5 sgRNA/Cas9 preparation

Two injection mixtures of 4.55 µL were prepared for *slc52a2*- and *slc52a3*- targeted injections. Injection mixes were prepared by adding 0.75 µL of 2 M KCl, 0.5 µL 10x Cas9 buffer, and 0.5625 µL of each of the 4 sgRNAs (800-3000 ng) synthesized against either *slc52a2* or *slc52a3*. A positive control injection mixture was also prepared for *tyr* using the same volume of KCl and 10x Cas9 buffer, but using 3000 ng of sgRNA and making up the remaining volume (if any) with RNase-free water. On the day that the microinjections are performed, 1 µL of EnGen Cas9 NLS Protein (20µM, New England Biolabs) and 0.5 µL of 0.05% phenol red were added to the injection mixtures prior to beginning the microinjection process. Mixtures were then incubated at 28.5°C for 5 minutes immediately prior to needle set-up[73].

2.4.6 sgRNA/Cas9 Microinjection

Embryos were injected with sgRNA/Cas9 at the single-cell stage as described in section 2.3.3. The droplet diameter used for sgRNA/Cas9 microinjections was 0.13 mm.

2.4.7 Genomic DNA Extraction

Zebrafish were euthanized at 5 dpf as described in section 2.2 prior to genomic DNA (gDNA) extraction. 5 embryos of a given condition were pooled together and the DNeasy Blood and Tissue kit (Qiagen) was used according to the manufacturer's instructions for gDNA extraction from tissue. The gDNA sample was then measured for yield and purity using the ND-100 Spectrophotometer.

2.4.8 Primer Design for *slc52a2* and *slc52a3* crispant PCR genotyping

Primers for amplification of *slc52a2* and *slc52a3* CRISPR/Cas9 target sites from gDNA were designed in Primer3 using the DNA sequences for *slc52a2* (Gene ID: 323832) and *slc52a3* (Gene ID: 678609) retrieved from NCBI within the *Danio rerio* genome assembly GRCz11 (Table 2-6). 2 sets of primers – 1 flanking each pair of sgRNA targets – were designed for each gene.

sgRNA Target Pair	Forward (5’→ 3’)	Reverse (5’→ 3’)	Product Size (bp)	Annealing Temperature (°C)
slc52a2 61 and 59	TGTGGCCGAAATTACAAGCA	TGCTGCACTTCCAATGTCAC	246	58
slc52a2 72 and 84	ACCTGGGACCAAAATAGAGCA	AGGATGGAATTTGCCTGCCT	180	58
slc52a3 69 and 67	TTAATGGCTTGTGGGTGGAG	CAGGATGCAGGCTACAACAC	206	58
slc52a3 62 and 56	CTCCCGCCAAATTTCTCCAC	ACAGTTTGTCTTGGGGTCCA	198	58
gne	CTTTGACATCGGCTCCAAAT	CCAGATGCAATATCCGAATG	206	56

Table 2-6 Primers used for PCR amplification of *slc52a2*, *slc52a3*, and *gne* sgRNA target sites from gDNA. Each primer set is listed alongside its product size, as well as its target gene and amplified sgRNA target site pair. sgRNA target sites are named according to the sgRNAs’ respective CRISPRscan scores.

2.4.9 Heteroduplex Mobility Assay

F0 zebrafish injected with sgRNA/Cas9 were genotyped at 5 dpf using the heteroduplex mobility assay (HMA) for screening of CRISPR/Cas9-mediated mutagenesis efficiency using a protocol adapted from Sorlien et al. (2018)[74]. Each pair of target sites was amplified from both wild-type gDNA and gDNA collected from sgRNA/Cas9-injected embryos. 50 µL PCR reactions were prepared using MyTaqTM DNA Polymerase (Meridian Bioscience) and run in a thermocycler according to the protocol outlined in Table 2-3. F0 zebrafish from an unpublished CRISPR/Cas9 model of GNE myopathy were used as a positive control, as these fish are confirmed to harbour CRISPR/Cas9-mediated mutations. F0 gDNA extracted from 4 dpf gne-targeted zebrafish as well as gDNA extracted from 4 dpf wild-type zebrafish was used for PCR amplification of the gne sgRNA target site (Table 2-6). PCR products were purified using the PCR Purification kit (Qiagen), eluted in 30 μL of nuclease-free water, and measured using the Nanodrop ND-1000. 250 mL of double-distilled water were boiled in a 600 mL glass beaker on a hot plate to create a boiling water bath in which all 30 μL of the PCR products were placed in a foam floatable test tube rack for 3 minutes. PCR products were then removed from the water bath and left to cool to room temperature for 1 hour. 6x loading dye was added to the PCR products and 500 ng of each PCR product were run on a 15% polyacrylamide gel using 1xTBE buffer and the Mini-PROTEAM TETRA electrophoresis system. The gel was then stained in 3x GelRed on a benchtop orbital shaker for 1 hour, after which DNA bands were visualized to screen for heteroduplex bands indicating successful CRISPR/Cas9-mediated mutations.

2.5 Phenotypic characterisation of zebrafish RTD models

2.5.1 Behavioural Assays

2.5.1.1 Spontaneous Chorion Movement Assay

Spontaneous movements are characterised by alternating trunk contractions performed by zebrafish embryos within the chorion starting at 17 hours post-fertilization (hpf), peaking at 19 hpf, and gradually decreasing until 27 hpf[75]. The spontaneous movement period is an early marker of neurodevelopment and corresponds to the axon outgrowth process[47,75]. In this study, the frequency of spontaneous movements performed by each zebrafish per minute was measured at 24 hpf as described by O’Connor et al. (2019)[47]. A Leica EZ4 W microscope was used to record 1-minute long MP4 videos of zebrafish embryos, and these videos were then used to manually count spontaneous movement frequency per minute for all conditions.

2.5.1.2 Light-Dark Activity Assay for Voluntary Swimming

To assess locomotor ability in the zebrafish at a later developmental timepoint of 5 dpf, the Zantiks MWP Behaviour system (Zantiks Ltd., United Kingdom) was used to employ a light-dark activity test adapted from Glazer and Brennan (2021)[76], whereby embryos were individually plated into 24-well plates with 800 µL of embryo media per well and subjected to alternating cycles of light and dark conditions. Within the Zantiks MWP unit, which is held at a constant interior temperature of 28.5°C, the fish were first acclimated for 5 minutes in the dark, followed by 6 alternating 5-minute light and dark cycles[76]. The plates were recorded during the 30-minute period post-acclimation with an infrared camera, and voluntary movement performed by each fish was tracked and measured[76]. These measurements were exported into a spreadsheet for each plate, and Microsoft Excel was used for the calculation of total distance travelled (mm), total distance travelled in either light or dark conditions (mm), total distance travelled during the 30-second transitions between conditions (mm), and velocity (mm/s) for each fish, as well as average distance travelled per second across the 30-minute test period by all fish (mm).

2.5.1.3 Acoustic Startle Reflex Assay

To test for a potential sensorineural hearing defect in the zebrafish, the acoustic startle reflex assay was performed between 5-7 dpf using a protocol adapted from Chen et al. (2020)[51]. The acoustic startle reflex in zebrafish is displayed from 5 dpf onwards in response to an acoustic stimulus[51]. The response is characterised by a C-shaped bend by the larva, after which it swims away from the direction of the stimulus[51]. The acoustic startle reflex assay was performed by placing an individual fish in a petri dish filled with embryo media against a white background, tapping the side of the petri dish using a metal rod, and observing whether the larva exhibited the acoustic startle reflex[51]. The assay was performed in ambient light, and it was ensured that the stimulus was only provided when the fish were mostly motionless and away from the walls of the petri dish[51]. 15 stimuli were provided to each larva, 2 minutes apart to prevent desensitization to the stimulus[51]. The percentage of positive responses exhibited was calculated for each fish[51].

2.5.2 Morphological Assays

2.5.2.1 Gross Morphology and Phenotype Scoring

Zebrafish were plated into 24-well plates filled with 800 µL of embryo media per well, and larva were individually imaged at 3 dpf with a Leica EZ4 W microscope using the 8X, 16X, and 25X objective lenses in the Leica Application Suite X software. In Fiji Image J, the fish in these images were measured for body length (mm) from the top of the head to the end of the tail, eye area (mm^2), and otic vesicle area (mm^2). Prior to capturing the images, a ruler was imaged at 8X, 16X, and 25X in order to calibrate the scale in Fiji Image J.

Images collected at 3 dpf were also used to assign 2 scores from 0-3 (normal to severe) to each fish based on edema and spinal curvature severity (Figure 2.02). The 2 scores were then added together, resulting in a total phenotype score for each fish.

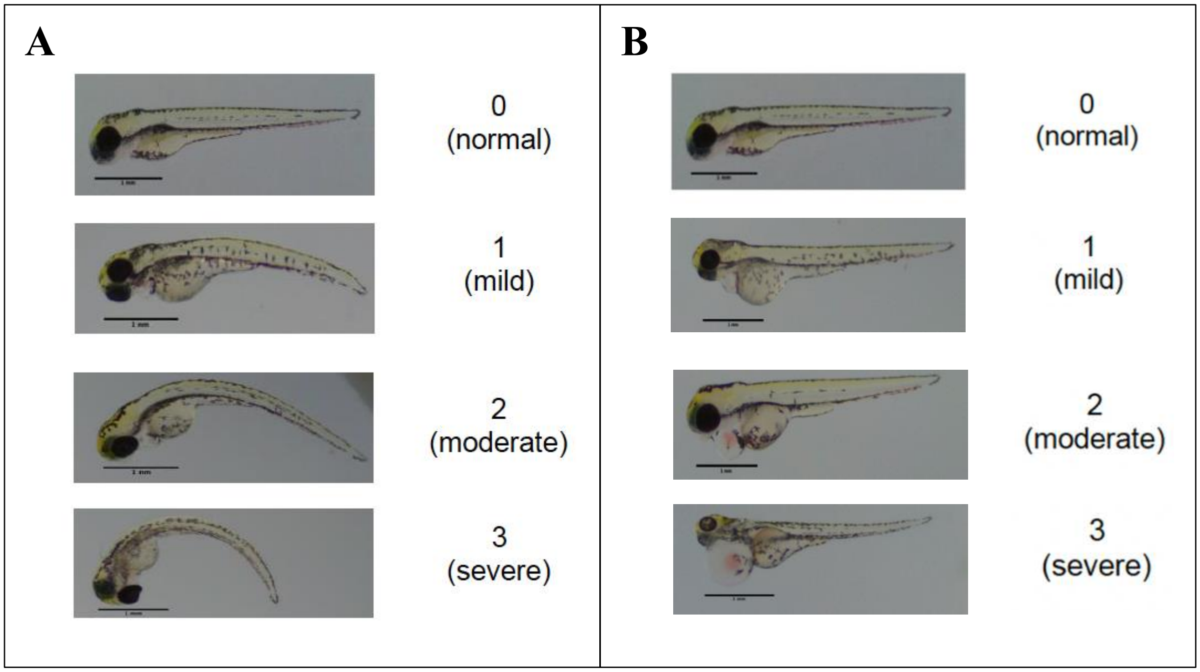

Figure 2.02 Phenotypic scoring scales. These scales were used to rank severity of (A) Spinal curvature and (B) Edema in zebrafish at 3 dpf. All scale bars are equivalent to 1 mm.

2.5.2.2 Immunological Staining

To inhibit pigment development in zebrafish embryos, N-Phenylthiourea (PTU) (Sigma, dissolved in DMSO) was diluted to 0.003% with embryo media and added to embryos on the day of fertilization. At either 24 hpf or 48 hpf, the embryos were dechorionated and euthanised as described in section 2.2, and were then fixed in 4% paraformaldehyde (PFA) in phosphate-buffered saline (PBS) for 4 hours at room temperature. Embryos were then washed twice for 5 minutes each with PBS. 100% ice cold acetone was applied to the embryos to permeabilize them at -20°C for 7 minutes, followed by 2 5-minute washes using PBS. The embryos were then blocked for 1 hour using 5% horse serum (HS) in 0.1% PBS-Tween (PBST) at room temperature. A solution of 1:500 synaptic vesicle protein 2 (SV2, Developmental Studies Hybridoma Bank) in HS-PBST was then applied to the embryos, and they were incubated on an orbital shaker at 4°C overnight. Embryos were washed 5 times in PBS-T for 20 minutes per wash and incubated in a solution of 1:1000 α-Bungarotoxin, Alexa Fluor conjugate 488 (Invitrogen) and 1:500 647 Alexa Fluor donkey anti-rabbit IgG (Invitrogen) in HS-PBST for 2 hours at room temperature. Embryos were then washed twice in PBST for 20 minutes per wash and left overnight on an orbital shaker at 4°C. Prior to mounting, embryos were washed in PBS for 20 minutes. Microscope slides were prepared for mounting with electrical tape which was cut to expose a window within which the embryos were mounted. The embryos were placed within the microscope slide window, which was filled with Vectashield mounting medium without DAPI (Vector Laboratories) and PBST. Clear nail polish was used to apply a coverslip over each slide window. Finally, a Zeiss Axio Imager M2 microscope was used to capture Z-stacks of each embryo using the 20X objective lens.

2.5.2.3 Image Preparation and Analysis

Fiji ImageJ was used to prepare and analyze Z-stack images captured by the Zeiss Axio Imager M2 microscope. The red and green channels were split for each Z-stack file, followed by generation of a maximum intensity projection image for further analysis. Myotomes were outlined using the freehand tool and labelled as regions of interest for colocalization analysis with the "Coloc2" plugin, which calculates Pearson's correlation coefficient as a measure of the linear correlation between fluorescence intensities in the red (presynaptic) and green (postsynaptic) channels[77].

For both the presynaptic and postsynaptic channels, the freehand tool was used to outline individual myotomes and measure myotomal area. Using the "analyze particles" command, mean presynaptic vesicle cluster area and mean postsynaptic acetylcholine receptor cluster area were calculated for each myotome. This was performed by first inverting the selected myotome and deleting the inverted selection to leave the myotome only. The image is then thresholded and made binary, resulting in a white background and black clusters. The image is then despeckled and the "analyze particles" command is applied, resulting in a measured area for each cluster and a mean cluster area for the myotome. Finally, the freehand tool was used to measure the length of each axonal projection from its initial origin point at the spinal cord until the end of the j-like shape marking the trajectory of the caudal primary motor neurons[78].

2.6 Therapeutic Screening of Riboflavin and Probenecid

2.6.1 OAT-3 and oat-3 Protein Structure Prediction and Comparison

Determining the structural similarity between human OAT-3 and zebrafish oat-3 would help to better understand whether probenecid will exert similar effects in zebrafish as it does in humans. Since no experimentally-confirmed structures exist for either human OAT-3 or zebrafish oat-3, these protein structures were predicted using the AlphaFold2_mmseqs2 Jupyter notebook within ColabFold version 1.5.2, which combines the MMseqs2 homology server with AlphaFold2 and Alphafold2-multimer[79]. Using a protein sequence encoding the protein of interest as the input, (OAT-3 Uniprot accession number: Q8TCC7; oat-3 Uniprot accession number: F1R8S7), related proteins are found using the MMSeqs2 server, which searches the UniRef100 and PDB70 databanks as well as an environmental sequence set[79]. These related protein sequences are then used for multiple sequence alignments[79]. Together with the MMseqs2 server, a Python library then uses the generated multiple sequence alignments to infer and visualize the 3D structure of the protein of interest[79]. For each predicted protein structure, a predicted local distance difference test (pLDDT) score is generated, which is AlphaFold2's per-residue confidence metric that ranges from 0-100, with higher scores indicating higher confidence[80]. The pLDDT score is generated using the local distance difference test, which assesses the stereochemical quality of the predicted protein structure based on the local distance differences of its atoms[81]. Ultimately, the pLDDT score estimates how closely the predicted protein structure would align with an experimentally confirmed structure[80]. Following the prediction of human OAT-3 and zebrafish oat-3 protein structures, these structures were superimposed in PyMOL using the "super" command, which generates a visual superimposition of both structures as well as a root-mean-square deviation (rmsd) score, representing the degree of similarity between the two structures[82]. A rmsd score of 0 Å represents identical structures, while scores up to 2.0 Å indicate good structural similarity and scores of 3.0 Å and above represent weak similarity[83–85].

2.6.2 OAT-3 and oat-3 Ligand Docking

SwissDock was employed to determine whether probenecid and riboflavin may bind to the same region in both human OAT-3 and zebrafish oat-3. SwissDock is a web server that can perform "docking", which is the virtual prediction of the interactions between two molecules, including protein-ligand binding[86]. Using the previously obtained predicted protein structures for OAT-3 and oat-3 as target proteins, SwissDock was used to predict the binding sites of probenecid and riboflavin onto each of the two target proteins. Both docking experiments generated multiple poses, each representing a different binding interaction of probenecid onto OAT-3 or oat-3. These poses were visualized in the UCSF Chimera software, and the top 5 poses were considered for each protein-ligand interaction were considered. The most favourable protein-ligand interaction for each of the OAT-3-probenecid, OAT-3-riboflavin, oat-3-probenecid, and oat-3-riboflavin experiments was deemed the interaction with the lowest Gibbs free energy change (ΔG) value, given that the ΔG of the system must be negative for protein-ligand binding to take place, and the stability of protein-ligand binding is reflected by the ΔG, such that the more negative the ΔG, the more stable the protein-ligand interaction[87–89].

2.6.3 Toxicity Screening in HEK-293T Cells

To establish non-toxic dose ranges for riboflavin and probenecid, various concentrations of each therapeutic were individually tested on human embryonic kidney 293T cells (HEK-293T), followed by cell viability measurement using the trypan blue assay[90]. Dose ranges were chosen based on previously reported dosages that were either non-toxic or beneficial for the prevention of riboflavin excretion[91–93]. HEK-293T cells were seeded in 24-well plates at a density of 5×10^5 cells/mL using High Glucose Dulbecco's Modified Eagle's Medium (DMEM) (Invitrogen). The DMEM was composed of 10% fetal bovine serum (FBS) (Sigma), 1% glutamine (Gibco), and 1% penicillin/streptomycin (Gibco). Riboflavin-treated cells were treated with 0 µM (ddH_2O), 0.1 µM, 1 µM, 10 µM, and 100 µM of riboflavin (Sigma R7649, dissolved in ddH_2O to a concentration of 1 mM), and cells were then harvested either 1.5 hours or 24 hours later for use in the trypan blue assay. Probenecid-treated cells were treated with 0 µM, 1 µM, 10 µM, 100 µM, 1 mM, and 10 mM of probenecid (VWR 76482-994, dissolved in sterile PBS to a concentration of 250 mM), and cells were harvested 24 hours later for the trypan blue assay. All drug dilutions were prepared using DMEM with the same composition as the DMEM used to seed the cells. Mean percent cell viability was graphed for all tested concentrations of riboflavin and probenecid.

2.6.4 Toxicity Screening in Wild-Type Zebrafish

To establish non-toxic dose ranges for riboflavin and probenecid in zebrafish, the same dose ranges tested in HEK-293T cells were also individually tested in wild-type zebrafish from 0 dpf to 4 dpf. For all *in vivo* drug testing, stock solutions were prepared by dissolving probenecid in PBS to a concentration of 250 mM and dissolving riboflavin in system water to a concentration of 1 mM. Immediately after fertilization (0 dpf), eggs were plated individually into 96-well plates along with 200 µL of a given drug dilution, prepared with embryo media. The fish were treated every 24 hours after the initial treatment until 3 dpf, totalling 3 treatments per drug. Treatments were provided by removing all media in each well and replacing it with a newly prepared 200 µL volume of drug solution. Survival was noted for each tested concentration of riboflavin and probenecid from 24 hours after the first treatment was provided until 4 dpf. Survival curves from 0-4 dpf were generated for riboflavin and probenecid.

2.6.5 Therapeutic Screening in *slc52a3* Morphants

Using the non-toxic dose ranges of riboflavin and probenecid identified in wild-type zebrafish, both drugs were then tested individually and in combination with each other on *slc52a3* morphants. Individually, riboflavin was tested at a concentration of 100 µM and probenecid was tested at 100 µM, 200 µM, 400 µM, and 800 µM. Once 200 µM was selected as the optimal probenecid dose for phenotypic rescue, 100 µM riboflavin supplementation was combined with 200 µM of probenecid. Each therapeutic screening experiment consisted of an untreated standard control MO-injected group, an untreated *slc52a3* MO-injected group, and a treated *slc52a3* MO-injected group. Zebrafish embryos were plated into 24-well plates and treated with 800 µL of a given drug dilution immediately after fertilization (0 dpf). Embryos were retreated every 24 hours until 5 dpf and from 1-5 dpf, embryos are used at the timepoints needed for various morphological and behavioural assays.

2.7 Statistics

Groups within datasets chosen for statistical comparison were assessed using the Anderson-Darling, Shapiro-Wilk, Kolmogorov-Smirnov, and D'Agostino-Pearson tests for normality. Datasets were deemed normal if all normality tests were positive, after which either an unpaired t-test or a one-way ANOVA with multiple comparisons was used to compare the chosen groups. Datasets were deemed non-normal if at least one of the normality tests were negative, after which either a Mann-Whitney U test or a Kruskal-Wallis test with multiple comparisons was conducted to compare the chosen groups. Normal datasets were described using mean (SD) and non-normal datasets were described as median (Q_1, Q_3). Statistical significance was determined using a threshold of $p < 0.05$.

3. Results

3.1 SLC52A2/slc52a2, SLC52A3a/slc52a3a, and SLC22A8/slc22a6l protein sequence alignment indicates adequate sequence identity

To determine whether *slc52a2* and *slc52a3* knockdown or knockout may result in an RTD-like phenotype in zebrafish, protein sequences for SLC52A2/slc52a2 and SLC52A3/slc52a3 were aligned. Protein sequences for SLC22A8 and slc22a6l, encoding human OAT-3 and zebrafish oat-

3, respectively, were also aligned to indicate whether zebrafish oat-3 may share functional similarity with human OAT-3. Sequence alignment of human SLC52A2 and zebrafish slc52a2 revealed a sequence identity of 51.94%, while protein sequence alignment of human SLC52A3a and zebrafish slc52a3a revealed a sequence identity of 56.73% (Fig. 3.01). Protein sequences for human SLC22A8 and zebrafish slc22a6l, encoding human OAT-3 and zebrafish oat-3, respectively, were also aligned to each other, resulting in a protein sequence identity of 49.54% (Fig. 3.02). SLC52A2/slc52a2 and SLC52A3/slc52a3 protein sequence alignments revealed adequate sequence identity between protein orthologs, providing evidence for functional similarity between orthologs. SLC22A8/slc22a6l share a sequence identity slightly lower than 50%, meaning that functional similarity between these orthologs may be likely, but drug screening of probenecid in the RTD zebrafish model is required to determine whether the drug interacts with zebrafish oat-3 similarly to how it interacts with human OAT-3.

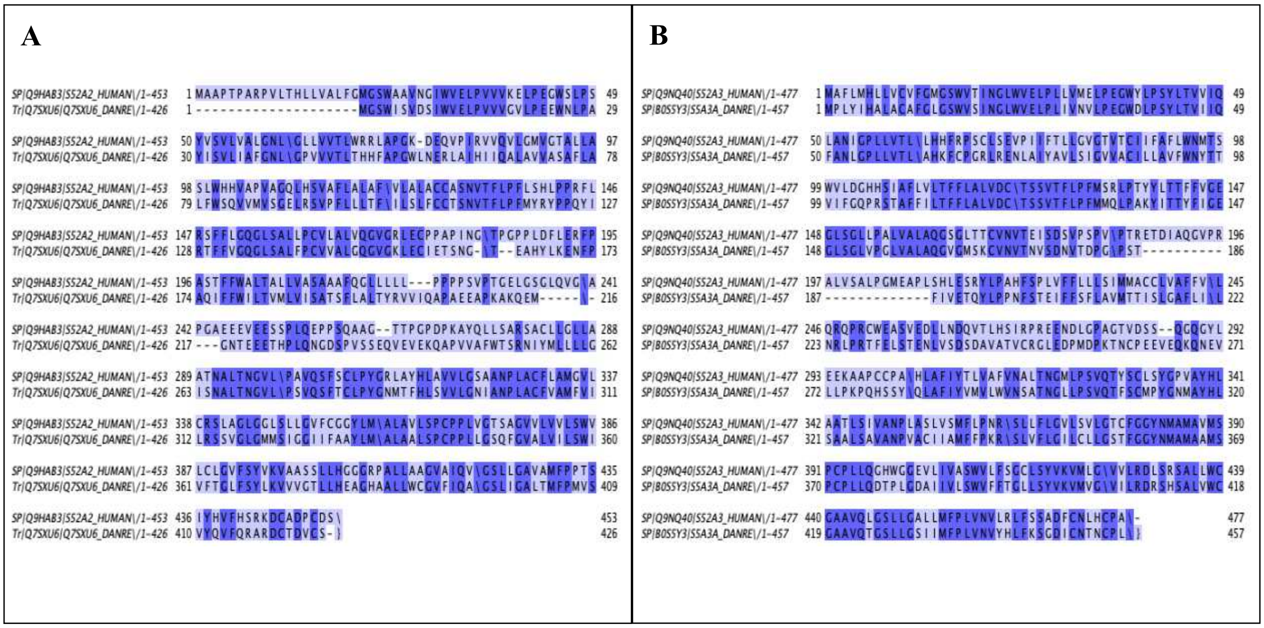

Figure 3.01 Protein sequence alignments for (A) human SLC52A2 with zebrafish ortholog slc52a2 and (B) human SLC52A3a with zebrafish ortholog slc52a3a. The first line of each row represents the human sequence, and the bottom line of each row represents the zebrafish sequence. Sequence identity is indicated by the dark purple boxes.

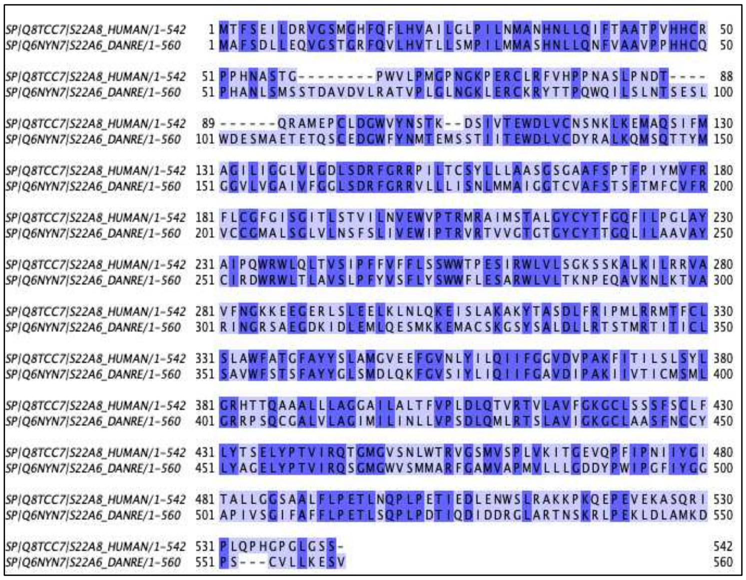

```
SP|Q8TCC7|S22A8_HUMAN/1-542    1 MTFSEILDRVGSMGHFQFLHVAILGLPILNMANHNLLQIFTAATPVHHCR  50
SP|Q6NYN7|S22A6_DANRE/1-560    1 MAFSDLLEQVGSTGRFQVLHVTLLSMPILMMASHNLLQNFVAAVPPHHCQ  50

SP|Q8TCC7|S22A8_HUMAN/1-542   51 PPHNASTG--------PWVLPMGPNGKPERCLRFVHPPNASLPNDT----  88
SP|Q6NYN7|S22A6_DANRE/1-560   51 PHANLSMSSTDAVDVLRATVPLGLNGKLERCKRYTTPQWQILSLNTSESL 100

SP|Q8TCC7|S22A8_HUMAN/1-542   89 ------QRAMEPCLDGWVYNSTK--DSIVTEWDLVCNSNKLKEMAQSIFM 130
SP|Q6NYN7|S22A6_DANRE/1-560  101 WDESMAETETQSCEDGWFYNMTEMSSTIITEWDLVCDYRALKQMSQTTYM 150

SP|Q8TCC7|S22A8_HUMAN/1-542  131 AGILIGGLVLGDLSDRFGRRPILTCSYLLLAASGSGAAFSPTFPIYMVFR 180
SP|Q6NYN7|S22A6_DANRE/1-560  151 GGVLVGAIVFGGLSDRFGRRVLLLISNLMMAIGGTCVAFSTSFTMFCVFR 200

SP|Q8TCC7|S22A8_HUMAN/1-542  181 FLCGFGISGITLSTVILNVEWVPTRMRAIMSTALGYCYTFGQFILPGLAY 230
SP|Q6NYN7|S22A6_DANRE/1-560  201 VCCGMALSGLVLNSFSLIVEWIPTRVRTVVGTGTGYCYTTGQLILAAVAY 250

SP|Q8TCC7|S22A8_HUMAN/1-542  231 AIPQWRWLQLTVSIPFFVFFLSSWWTPESIRWLVLSGKSSKALKILRRVA 280
SP|Q6NYN7|S22A6_DANRE/1-560  251 CIRDWRWLTLAVSLPFYVSFLYSWWFLESARWLVLTKNPEQAVKNLKTVA 300

SP|Q8TCC7|S22A8_HUMAN/1-542  281 VFNGKKEEGERLSLEELKLNLQKEISLAKAKYTASDLFRIPMLRRMTFCL 330
SP|Q6NYN7|S22A6_DANRE/1-560  301 RINGRSAEGDKIDLEMLQESMKKEMACSKGSYSALDLLRTSTMRTITICL 350

SP|Q8TCC7|S22A8_HUMAN/1-542  331 SLAWFATGFAYYSLAMGVEEFGVNLYILQIIFGGVDVPAKFITILSLSYL 380
SP|Q6NYN7|S22A6_DANRE/1-560  351 SAVWFSTSFAYYGLSMDLQKFGVSIYLIQIIFGAVDIPAKIIVTICMSML 400

SP|Q8TCC7|S22A8_HUMAN/1-542  381 GRHTTQAAALLLAGGAILALTFVPLDLQTVRTVLAVFGKGCLSSSFSCLF 430
SP|Q6NYN7|S22A6_DANRE/1-560  401 GRRPSQCGALVLAGIMILINLLVPSDLQMLRTSLAVIGKGCLAASFNCCY 450

SP|Q8TCC7|S22A8_HUMAN/1-542  431 LYTSELYPTVIRQTGMGVSNLWTRVGSMVSPLVKITGEVQPFIPNIIYGI 480
SP|Q6NYN7|S22A6_DANRE/1-560  451 LYAGELYPTVIRQSGMGWVSMMARFGAMVAPMVLLLGDDYPWIPGFIYGG 500

SP|Q8TCC7|S22A8_HUMAN/1-542  481 TALLGGSAALFLPETLNQPLPETIEDLENWSLRAKKPKQEPEVEKASQRI 530
SP|Q6NYN7|S22A6_DANRE/1-560  501 APIVSGIFAFFLPETLSQPLPDTIQDIDDRGLARTNSKRLPEKLDLAMKD 550

SP|Q8TCC7|S22A8_HUMAN/1-542  531 PLQPHGPGLGSS-                                      542
SP|Q6NYN7|S22A6_DANRE/1-560  551 PS---CVLLKESV                                      560
```

Figure 3.02 Protein sequence alignments for human SLC22A8 with zebrafish ortholog slc22a6. The first line of each row represents the human sequence, and the bottom line of each row represents the zebrafish sequence. Sequence identity is indicated by the dark purple boxes.

3.2 *slc52a2*, *slc52a3*, and *slc22a6l* are expressed in zebrafish during early development

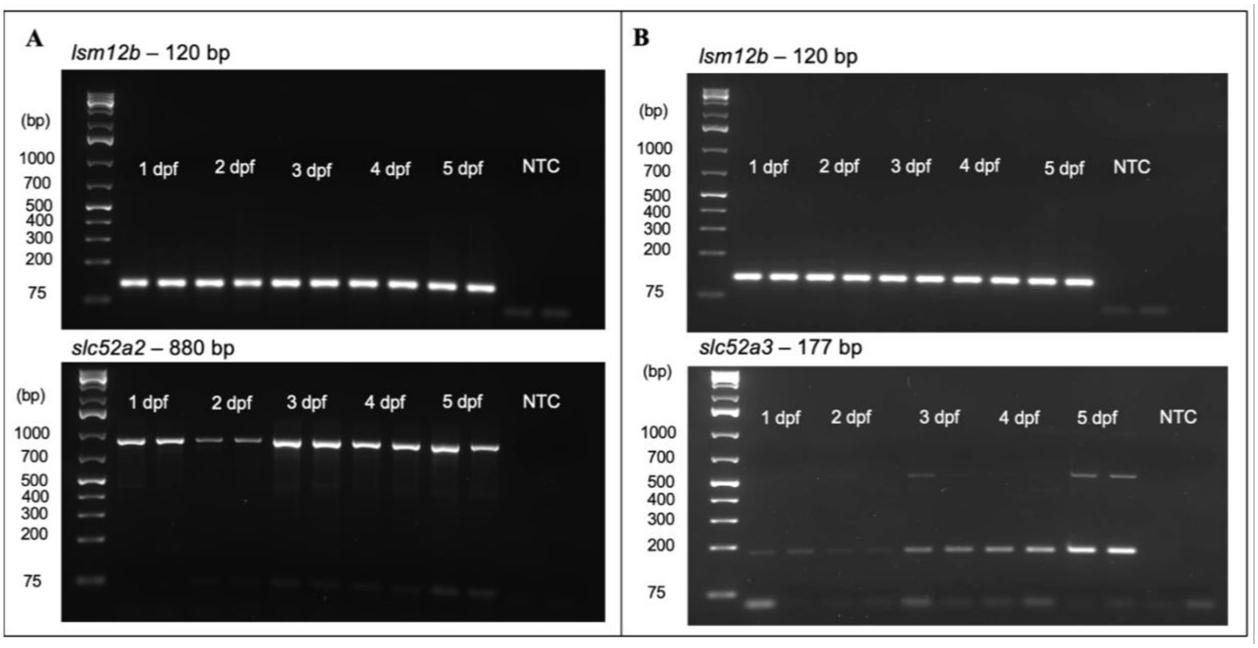

Figure 3.03 RT-PCR confirmation of (A) *slc52a2* and (B) *slc52a3* gene expression in wild-type zebrafish between 1-5 dpf. *lsm12b* was used as a control. RT-PCR reactions used 1:10 diluted cDNA. NTC indicates a well containing a non-template control sample.

To establish an expression profile for *slc52a2*, *slc52a3*, and *slc22a6l* during early zebrafish development, RT-PCR analysis was conducted using cDNA collected from wild-type zebrafish between 1-5 dpf. RT-PCR revealed that *slc52a2* is stably expressed in zebrafish between 1-5 dpf, with a decrease in expression detected at 2 dpf (Fig. 3.03). A time-dependent increase in *slc52a3* and *slc22a6l* expression was also observed, with the strongest expression of both genes detected at 5 dpf (Fig. 3.03, Fig. 3.04). Stable expression of *slc52a2* and *slc52a3* at these timepoints allows for confirmation of gene knockdown and knockout in response to morpholino- or CRISPR/Cas9-mediated gene targeting. Additionally, stable expression of *slc22a6l* at these timepoints indicates that probenecid has the potential to interact with zebrafish oat-3 and inhibit riboflavin excretion, provided there is adequate functional similarity between human OAT-3 and zebrafish oat-3.

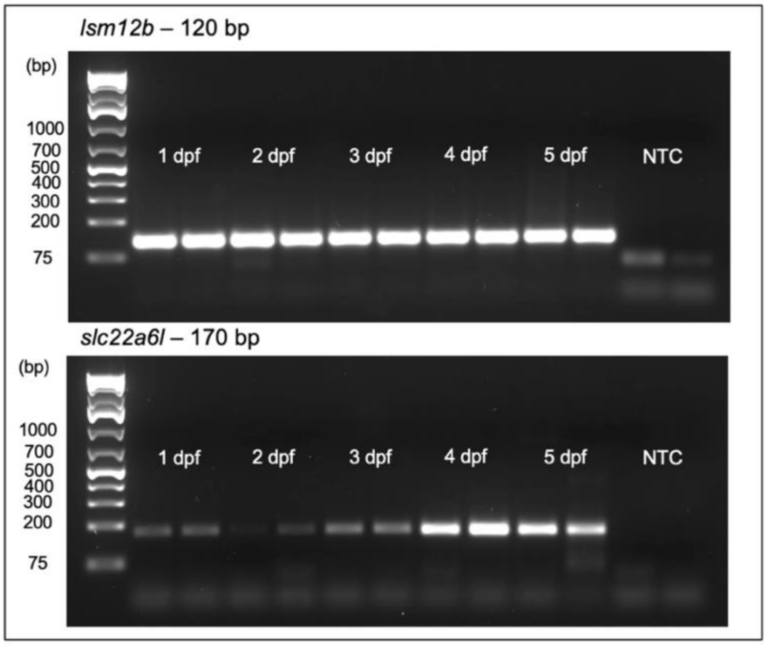

Figure 3.04 RT-PCR confirmation of *slc22a6l* gene expression in wild-type zebrafish between 1-5 dpf. *lsm12b* was used as a control. RT-PCR reactions used 1:10 diluted cDNA. NTC indicates a well containing a non-template control sample.

3.3 Morpholino-mediated knockdown of RTD disease genes *slc52a2* and/or *slc52a3*

3.3.1 *slc52a3* and *slc52a2*/*slc52a3* combined knockdown zebrafish recapitulate several characteristics of the human RTD phenotype

To assess the potential RTD-like phenotype resulting from *slc52a2* and/or *slc52a3* knockdown, morpholino-mediated knockdowns of these target genes were generated and phenotypically characterised. We achieved effective knockdown of *slc52a2* and *slc52a3* expression following MO microinjection according to section 2.3.3, as demonstrated by the absence of *slc52a2* and *slc52a3* expression in MO-injected fish at a MO dosage of 6 ng (Fig. 3.05).

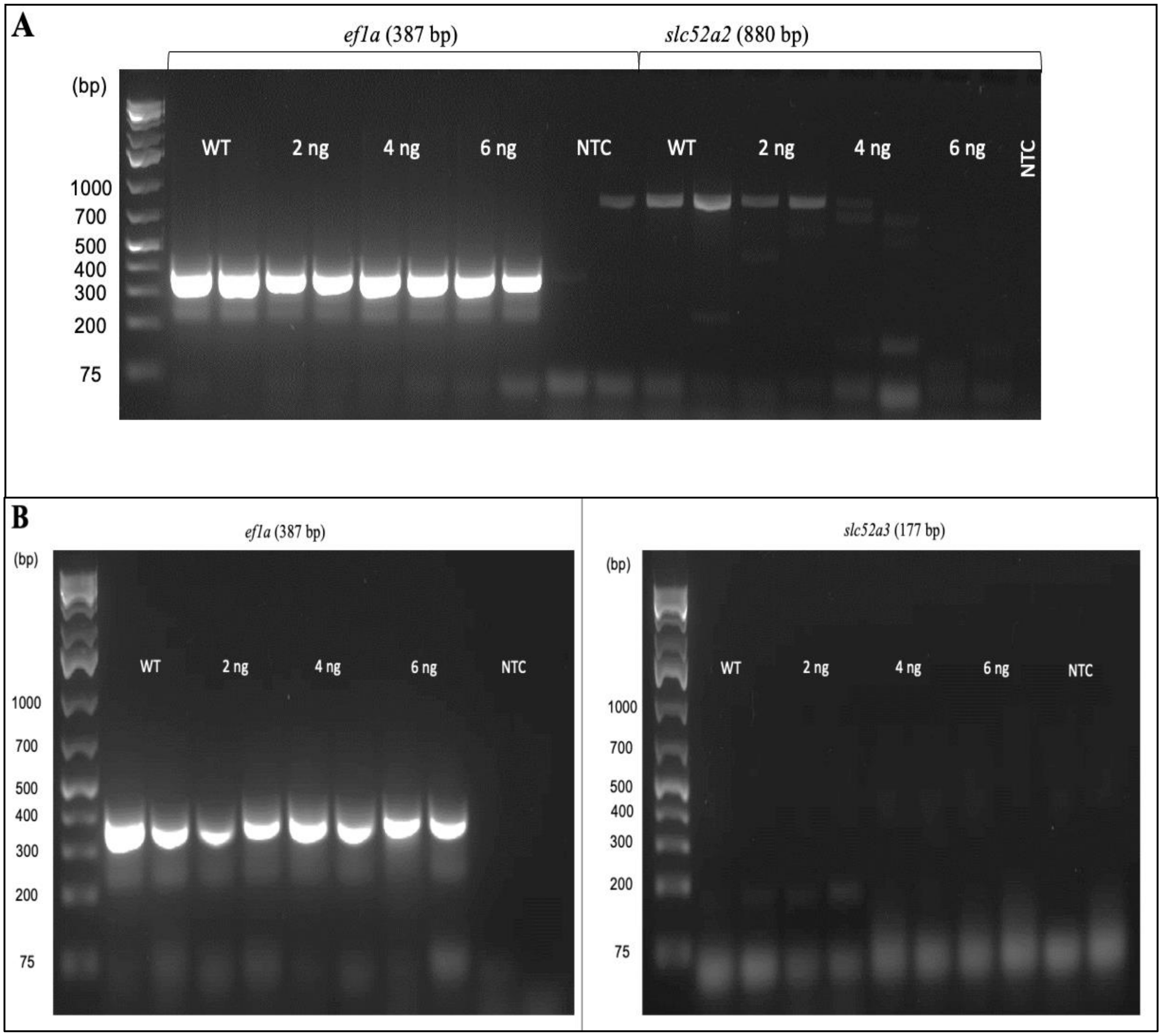

Figure 3.05 RT-PCR analysis of (A) *slc52a2* and (B) *slc52a3* gene expression using 1:10 diluted cDNA collected from morpholino-injected zebrafish at 3 dpf. Morpholinos were

administered at doses of 0 ng (WT), 2 ng, 4 ng, and 6 ng, with two wells for each dosage. *ef1a* was used as a control. NTC indicates a well containing a non-template control sample.

Following dose-response experiments, we chose a dosage of 8 ng for all subsequent MO experiments in this study. At this dosage, we observed multiple RTD-like phenotypic characteristics in *slc52a3* and *slc52a2*/*slc52a3* combined knockdown zebrafish, whereas no phenotypic differences were detected between control morphants and *slc52a2* morphants. Firstly, early neurodevelopment was examined using the spontaneous movement assay, which revealed that *slc52a3* and *slc52a2*/*slc52a3* combined morphants exhibited a higher frequency of spontaneous movements per minute at 24 hpf compared to their control MO-injected clutch mates (Fig. 3.06).

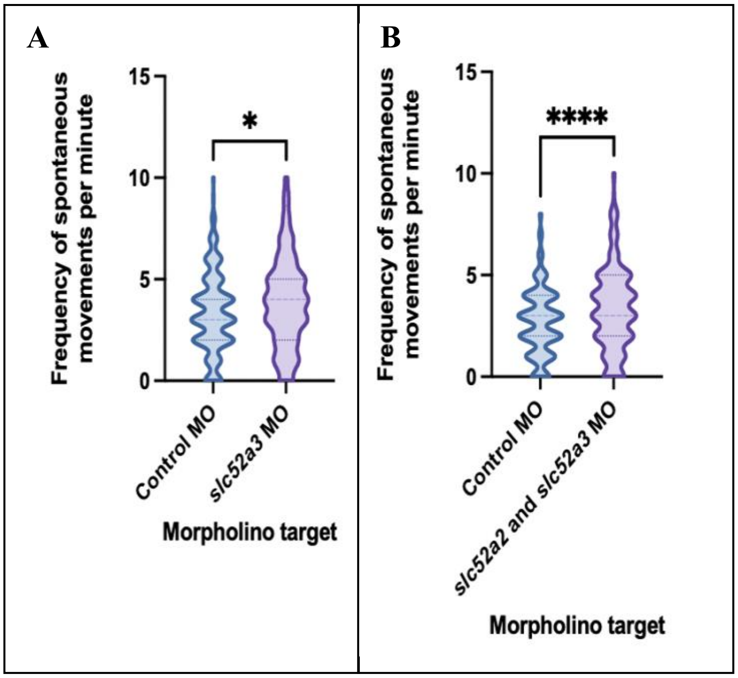

Figure 3.06 Frequency of spontaneous movements in *slc52a3* and *slc52a2/slc52a3* combined morphants at 24 hpf. (A) *slc52a3* (Control MO = 3 (2, 4), *slc52a3* MO = 4 (2, 5); Mann-Whitney test). Control MO *n* = 188, *slc52a3* MO *n* = 182. (B) *slc52a2/slc52a3* combined morphants (Control MO = 3 (2, 4), *slc52a2/slc52a3* MO = 3 (2, 5); Mann-Whitney test). Control MO *n* = 312 *slc52a2/slc52a3* MO *n* = 314. * = $p < 0.05$; **** = $p < 0.0001$.

At 3 dpf, *slc52a3* and *slc52a2*/*slc52a3* combined morphants demonstrated reduced body length, eye area, and otic vesicle area (Fig. 3.08, Fig. 3.09). The *slc52a3* and *slc52a2*/*slc52a3* combined morphants also exhibited an increased total phenotype score compared to their control MO-injected clutch mates, and since edema was not significantly increased in either knockdown group, this increased total phenotype score was attributed solely to an increase in spinal curvature (Fig. 3.10).

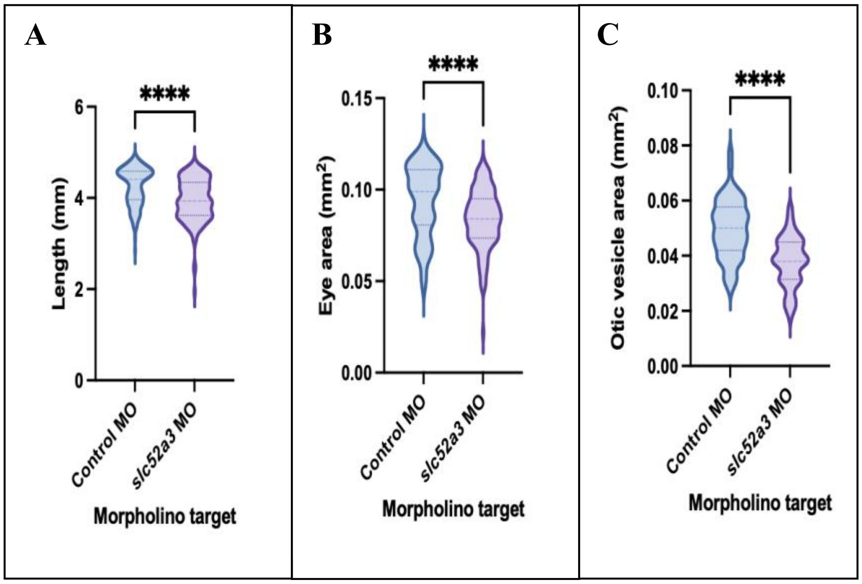

Figure 3.07 Morphological characteristics of *slc52a3* morphants at 3 dpf. (A) Body length (mm) (Control MO = 4.409 (3.961, 4.589), *slc52a3* MO = 3.933 (3.618, 4.345); Mann-Whitney test). Control MO *n* = 161, *slc52a3* MO *n* = 158. (B) eye area (mm^2) (Control MO = 0.099 (0.081, 0.111), *slc52a3* MO = 0.084 (0.074, 0.095); Mann-Whitney test). Control MO *n* = 119, *slc52a3* MO *n* = 129. (C) otic vesicle area (mm^2) (Control MO = 0.05 (0.042, 0.058), *slc52a3* MO = 0.038 (0.032, 0.045); Mann-Whitney test). Control MO *n* = 120, *slc52a3* MO *n* = 121. **** = $p < 0.0001$.

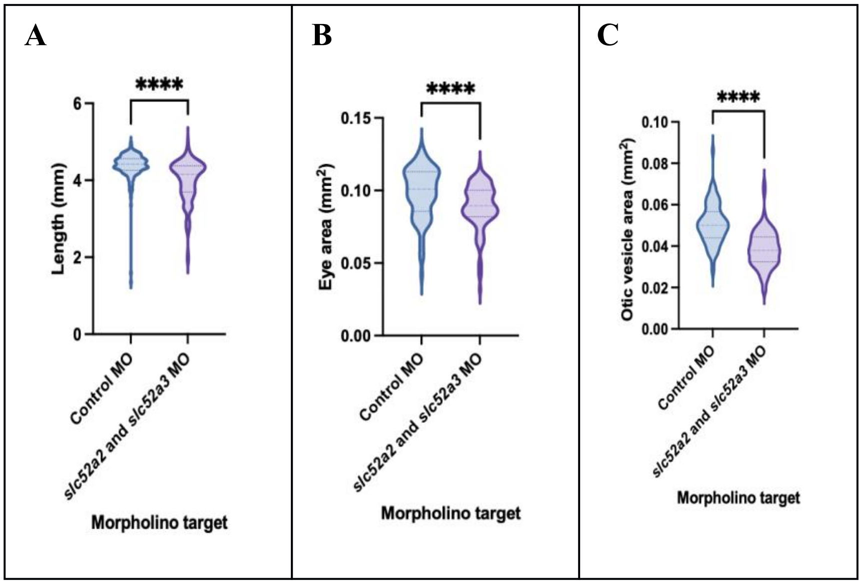

Figure 3.08 Morphological characteristics of *slc52a2*/*slc52a3* combined morphants at 3 dpf. (A) Body length (mm) (Control MO = 4.420 (4.262, 4.562), *slc52a2*/*slc52a3* MO = 4.159 (3.695, 4.380); Mann-Whitney test). Control MO *n* = 182, *slc52a2*/*slc52a3* MO *n* = 182. (B) eye area (mm^2) (Control MO = 0.10 (0.086, 0.113), *slc52a2*/*slc52a3* MO = 0.09 (0.082, 0.10); Mann-Whitney test) Control MO *n* = 86, *slc52a2*/*slc52a3* MO *n* = 118. (C) otic vesicle area (mm^2) (Control MO = 0.05 (0.044, 0.057), *slc52a2*/*slc52a3* MO = 0.038 (0.033, 0.045); Mann-Whitney test). Control MO *n* = 80, *slc52a2*/*slc52a3* MO *n* = 89. **** = $p < 0.0001$.

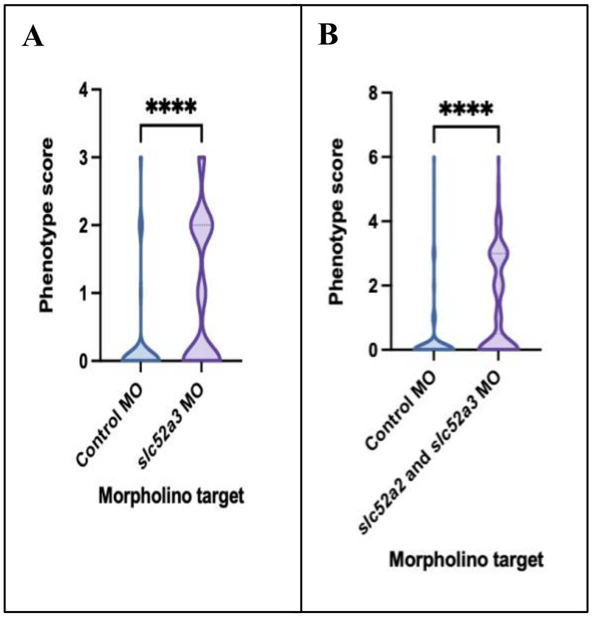

Figure 3.09 Total phenotype scores for *slc52a3* and *slc52a2/slc52a3* morphants at 3 dpf according to a scale ranking oedema and spinal curvature from 0 (normal) to 3 (severe). (A) *slc52a3* (Control MO = 0 (0, 0), *slc52a3* MO = 1 (0, 2); Mann-Whitney test). Control MO *n* = 161, *slc52a3* MO *n* = 156. (B) *slc52a2/slc52a3* combined morphants (Control MO = 0 (0, 0), *slc52a2/slc52a3* MO = 0.5 (0, 3); Mann-Whitney test). Control MO *n* = 185, *slc52a2/slc52a3* MO *n* = 186. **** = $p < 0.0001$.

Further, locomotor activity was impaired in *slc52a3* and *slc52a2*/*slc52a3* combined morphant larvae at 5 dpf, as shown by the results of the light-dark activity test. Compared to control morphants, *slc52a3* and *slc52a2*/*slc52a3* combined knockdown fish swam a shorter average distance during the entire 30-minute test, as well as a shorter total distance overall, a shorter total distance during each 30-second cycle-to-cycle transition, and a shorter total distance across all dark cycles – during which the voluntary movement is expected to increase (Fig. 3.11, Fig. 3.12). These *slc52a3* and *slc52a2*/*slc52a3* combined morphants also swam at a reduced velocity compared to their control MO-injected clutch mates (Fig. 3.11, Fig. 3.12). In addition, to examine the impact of the RTD-like phenotype on hearing in *slc52a3* and *slc52a2*/*slc52a3* combined knockdown larvae, the acoustic startle reflex assay was conducted between 5-7 dpf, revealing a reduction in the percent response of *slc52a3* and *slc52a2*/*slc52a3* combined knockdown larvae to 15 acoustic stimuli in comparison to control morphants (Fig. 3.13).

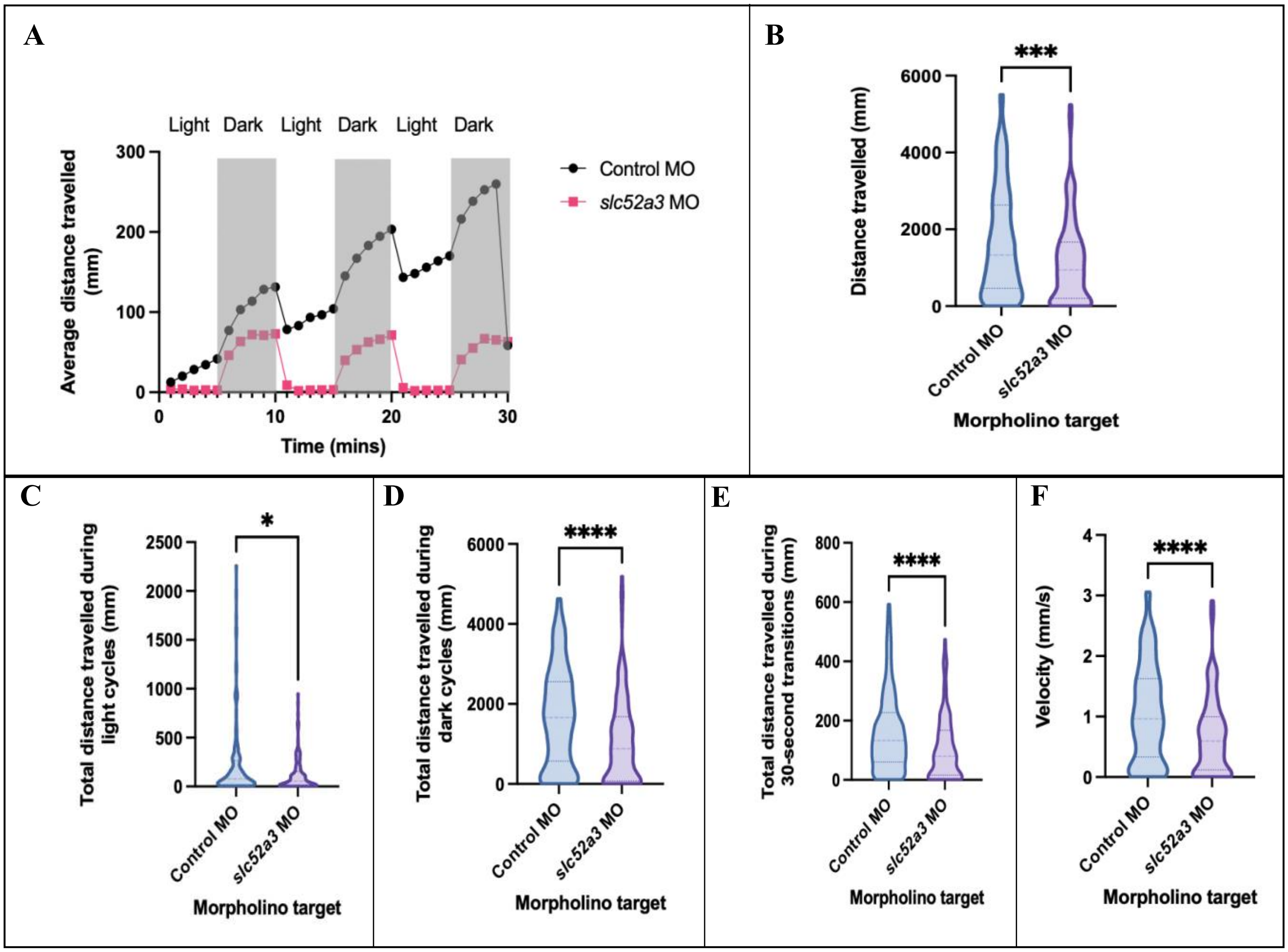

Figure 3.10 Voluntary locomotor activity performed by *slc52a3* morphants during light-dark activity test at 5 dpf. (A) Average distance travelled (mm) by *slc52a3* morphant zebrafish per minute during light-dark activity test (Control MO = 0.714 (0.154, 1.525), *slc52a3* MO = 0.428 (0.034, 1.109); Mann-Whitney test). Control MO *n* = 100, *slc52a3* MO *n* = 107. (B) Total distance travelled (mm) by *slc52a3* morphant zebrafish during light-dark activity test (Control MO = 1333 (462.2, 2633), *slc52a3* MO = 942.4 (200.9, 1668); Mann-Whitney test). Control MO *n* = 178, *slc52a3* MO *n* = 170. (C) Total distance travelled (mm) by *slc52a3* morphant zebrafish during light cycles in light-dark activity test (Control MO = 76.8 (19.6, 266.4), *slc52a3* MO = 56.15 (6.85, 152.3); Mann-Whitney test). Control MO *n* = 143, *slc52a3* MO *n* = 148. (D) Total distance

travelled (mm) by *slc52a3* morphant zebrafish during dark cycles in light-dark activity test (Control MO = 1663 (570.4, 2558), *slc52a3* MO = 880.1 (74.75, 1683); Mann-Whitney test). Control MO *n* = 143, *slc52a3* MO *n* = 148. (E) Total distance travelled (mm) by *slc52a3* morphant zebrafish during 30-second transitions between cycles in light-dark activity test (Control MO = 132.7 (60.3, 227.2), *slc52a3* MO = 79.65 (16.63, 167.6); Mann-Whitney test). Control MO *n* = 143, *slc52a3* MO *n* = 148. (E) Average velocity travelled (mm/s) by *slc52a3* morphant zebrafish during light-dark activity test (Control MO = 0.961 (0.33, 1.624), *slc52a3* MO = 0.595 (0.117, 0.997); Mann-Whitney test). Control MO *n* = 143, *slc52a3* MO *n* = 146. * = p < 0.05, ** = p < 0.01, *** = p < 0.001, **** = p < 0.0001.

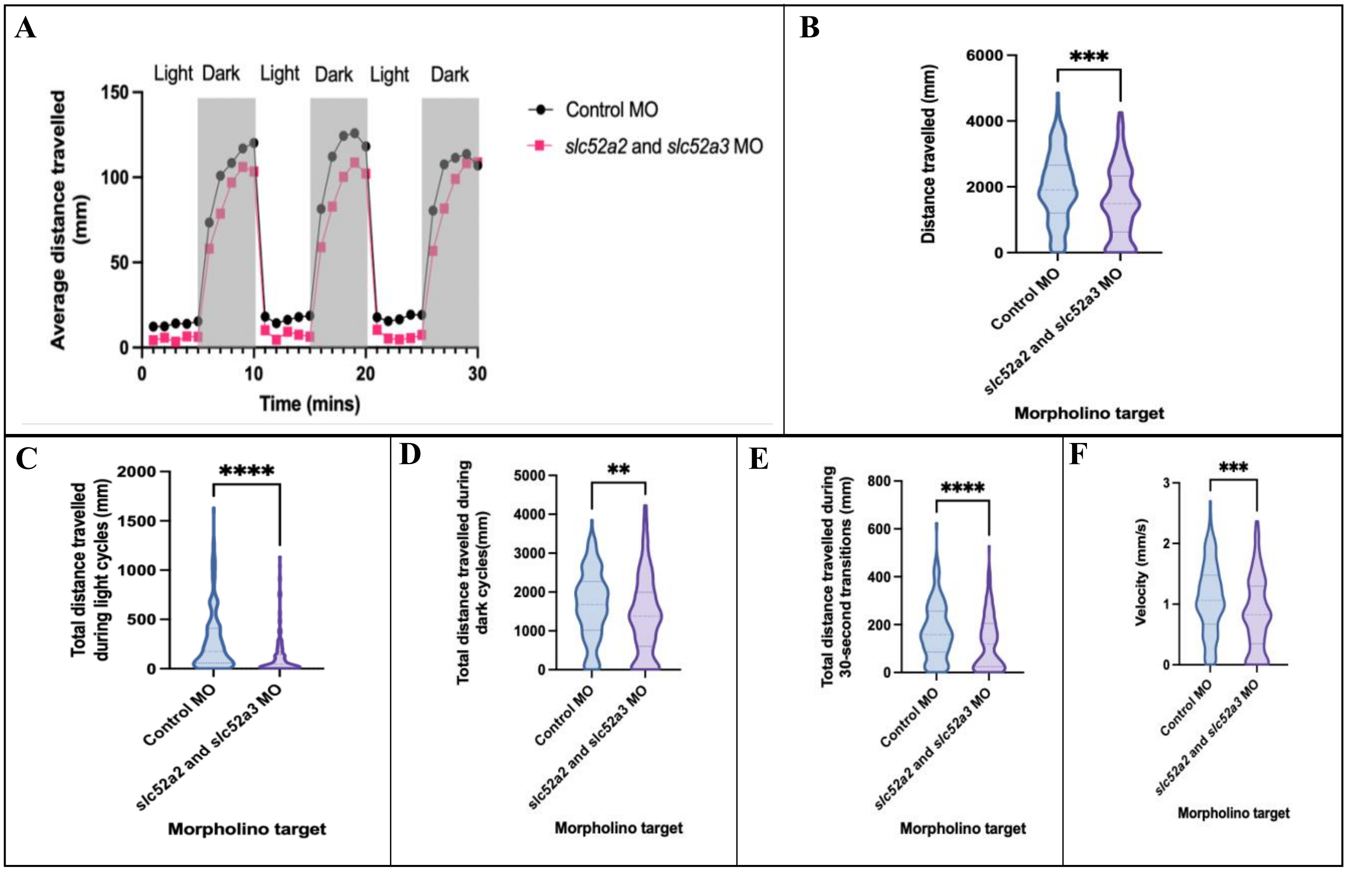

Figure 3.11 Voluntary locomotor activity performed by *slc52a2/slc52a3* combined morphants during light-dark activity test at 5 dpf. (A) Average distance travelled (mm) by *slc52a2/slc52a3* combined morphant zebrafish per minute during light-dark activity test (Control MO = 0.996 (0.251, 1.928), *slc52a2/slc52a3* MO = 0.678 (0.087, 1.621); Mann-Whitney test). Control MO *n* = 183, *slc52a2/slc52a3* MO *n* = 189. (B) Total distance travelled (mm) by *slc52a2/slc52a3* combined morphant zebrafish during light-dark activity test (Control MO = 1909 (1202, 2659), *slc52a2/slc52a3* MO = 1486 (629.6, 2334); Mann-Whitney test). Control MO *n* = 183, *slc52a2/slc52a3* MO *n* = 189. (C) Total distance travelled (mm) by *slc52a2/slc52a3* combined morphant zebrafish during light cycles in light-dark activity test (Control MO = 174.3 (57.4, 409.6), *slc52a2/slc52a3* MO = 45.2 (11.8, 144.2); Mann-Whitney test). Control MO *n* = 183, *slc52a2/slc52a3* MO *n* = 189. (D) Total distance travelled (mm) by *slc52a2/slc52a3* combined morphant zebrafish during dark cycles in light-dark activity test (Control MO = 1679 (1018, 2273), *slc52a2/slc52a3* MO = 1377 (601.1, 1994); Mann-Whitney test). Control MO *n* = 183,

slc52a2/slc52a3 MO *n* = 189. (E) Total distance travelled (mm) by *slc52a2/slc52a3* combined morphant zebrafish during 30-second transitions between cycles in light-dark activity test (Control MO = 158 (85.9, 256.3), *slc52a2/slc52a3* MO = 118.6 (24.15, 204.7); Mann-Whitney test). Control MO *n* = 183, *slc52a2/slc52a3* MO *n* = 189. (E) Average velocity travelled (mm/s) by *slc52a2/slc52a3* combined morphant zebrafish during light-dark activity test (Control MO = 1.061 (0.668, 1.477), *v* MO = 0.826 (0.350, 1.297); Mann-Whitney test). Control MO *n* = 183, *slc52a2/slc52a3* MO *n* = 189. ** = p < 0.01, *** = p < 0.001, **** = p < 0.0001.

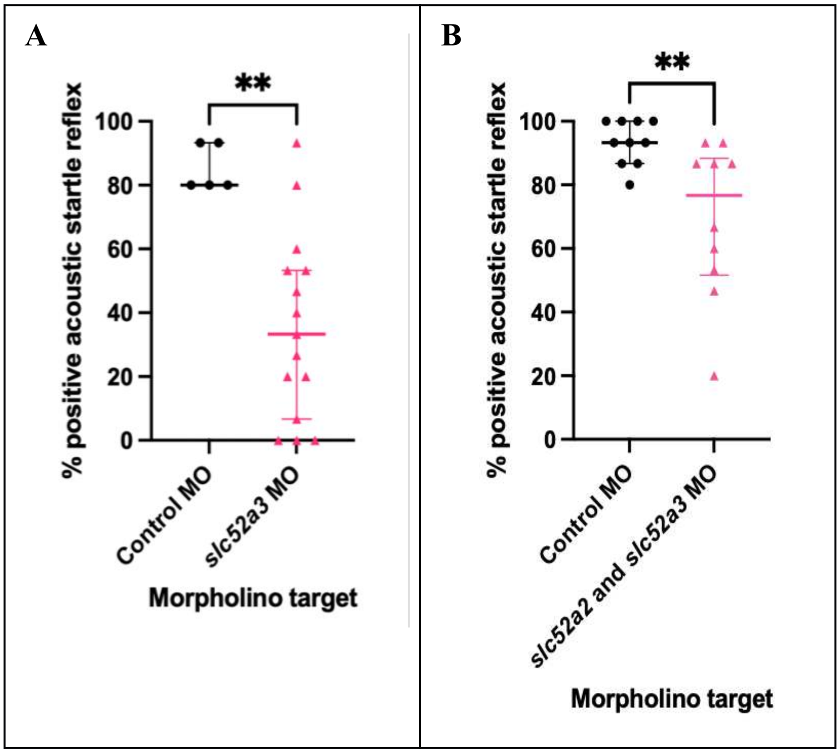

Figure 3.12 % positive acoustic startle reflex exhibited by *slc52a3* and *slc52a2/slc52a3* combined morphant zebrafish between 5-7 dpf. (A) *slc52a3* morphants (Control MO = 80 (80, 93.33), *slc52a3* MO = 33.33 (6.667, 53.33); Mann-Whitney test). Control MO *n* = 5 *slc52a3* MO *n* = 15. (B) *slc52a2/slc52a3* combined morphants (Control MO = 93.33 (86.67, 100), *slc52a2/slc52a3* MO = 76.67 (51.67, 88.33); Mann-Whitney test). Control MO *n* = 10 *slc52a2/slc52a3* MO *n* = 10. ** = p < 0.01.

Finally, immunological staining was conducted at 48 hpf to visualize any potential RTD-like impairments in neuromuscular junction morphology. Motor axon length and colocalization of the presynaptic channel with the postsynaptic channel were found to be significantly decreased in *slc52a3* morphants compared to control morphants (Fig. 3.14). Overall, *slc52a3* and *slc52a2/slc52a3* combined knockdown zebrafish demonstrated an RTD-like phenotype, presenting the possibility to progress with *p53* co-knockdown and rescue mRNA experiments as well as therapeutic screening to identify phenotypic ameliorations.

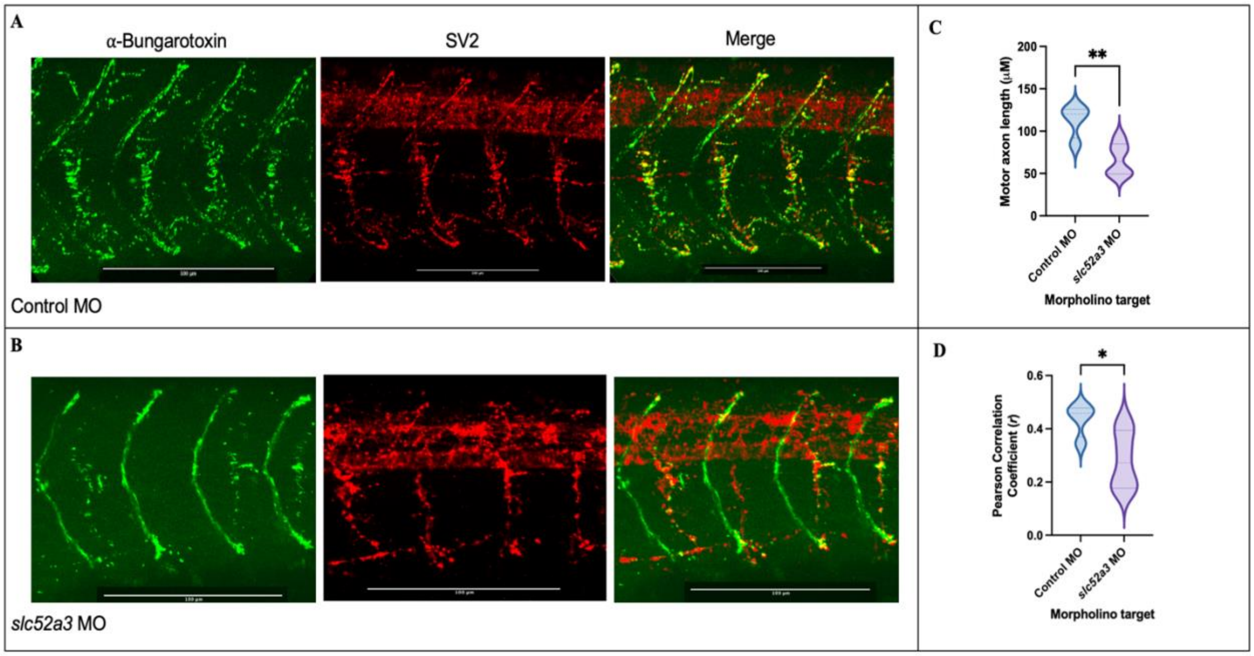

Figure 3.13 Neuromuscular junction morphology of *slc52a3* morphant zebrafish at 48 hpf. (A) Postsynaptic (α-Bungarotoxin)- and presynaptic (SV2) regions of (A) Control morphants and (B) *slc52a3* morphants. (C) Motor axon length of *slc52a3* morphants (Control MO = 112.6 (19.37), *slc52a3* MO = 67.03 (19.10); Unpaired t-test). Control MO *n* = 4 *slc52a3* MO *n* = 6. (D) Pearson Correlation Coefficient calculated as a measure of presynaptic (red, SV2) and postsynaptic (green, α-Bungarotoxin) colocalization (Control MO = 0.4356 (0.062), *slc52a3* MO = 0.284 (0.108); Unpaired t-test). Control MO *n* = 4 *slc52a3* MO *n* = 6. * = $p < 0.05$, ** = $p < 0.01$.
Scale bars are equivalent to 100 µm.

3.3.2 *p53/slc52a3* morpholino co-injection reinforces the specificity of the *slc52a3* morphant phenotype

To determine whether the slc52a3 morphant phenotype is due to the activation of tumor suppressor protein p53, *p53*/*slc52a3* MO-injected embryos were phenotypically characterised, revealing an overlapping phenotype with the *slc52a3* morphants. Compared to control morphants at 3 dpf, *p53*/*slc52a3* morphants exhibited shorter body length, smaller eye area and otic vesicle area, and an increased total phenotype score due to increased spinal curvature (Fig. 3.15). The *p53*/*slc52a3* morphants also demonstrated a higher frequency of spontaneous movements per minute than control morphants at 24 hpf (Fig. 3.15). Later, the light-dark activity test results indicated that *p53/slc52a3* morphants still showed impaired locomotor ability, with co-injected morphants swimming a shorter average distance, a shorter total distance overall, a shorter total distance during the light cycles and the dark cycles, and a shorter total distance across all the 30-second transition periods compared to control morphants (Fig. 3.16). The *p53/slc52a3* morphants also swam at a slower velocity than the control morphants (Fig. 3.16). Due to the maintenance of the *slc52a3* morphant phenotype in *p53/slc52a3* morphants, it can be deduced that the RTD-like phenotype exhibited by *slc52a3* morphants is specific and not a result of p53 activation.

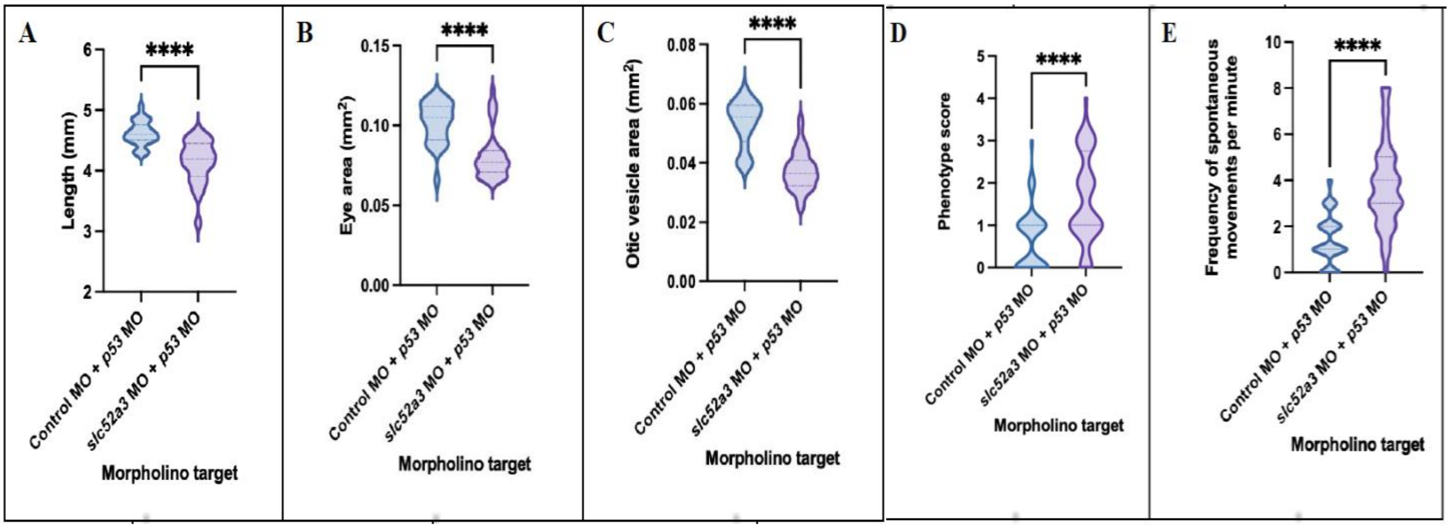

Figure 3.14 Phenotypic characteristics of *slc52a3* MO/*p53* co-injected morphants. (A) Body length (mm) of *slc52a3+p53* morphants (Control MO = 4.6 (4.505, 4.757), *slc52a3/p53* MO = 4.192 (3.901, 4.447); Mann-Whitney test). Control MO *n* = 42 *slc52a3/p53* MO *n* = 48. (B) Eye area (mm^2) of *slc52a3+p53* morphants (Control MO = 0.105 (0.091, 0.112), *slc52a3/p53* MO = 0.077 (0.071, 0.084); Mann-Whitney test). Control MO *n* = 23 *slc52a3/p53* MO *n* = 46. (C) Otic vesicle area (mm^2) of *slc52a3+p53* morphants (Control MO = 0.056 (0.047, 0.06), *slc52a3/p53* MO = 0.037 (0.032, 0.041); Mann-Whitney test). Control MO *n* = 16 *slc52a3/p53* MO *n* = 40. (D) Total phenotype scores for *slc52a3+p53* morphants according to a scale ranking oedema and spinal curvature on a scale from 0 (normal) to 3 (severe) (Control MO = 1 (0, 1), *slc52a3/p53* MO = 1 (1, 2.75); Mann-Whitney test). Control MO *n* = 48 *slc52a3/p53* MO *n* = 48. (E) Frequency of spontaneous movements in *slc52a3+p53* morphants (Control MO = 1 (1, 2), *slc52a3/p53* MO = 4 (3, 5); Mann-Whitney test). Control MO *n* = 69 *slc52a3/p53* MO *n* = 47. **** = $p < 0.0001$.

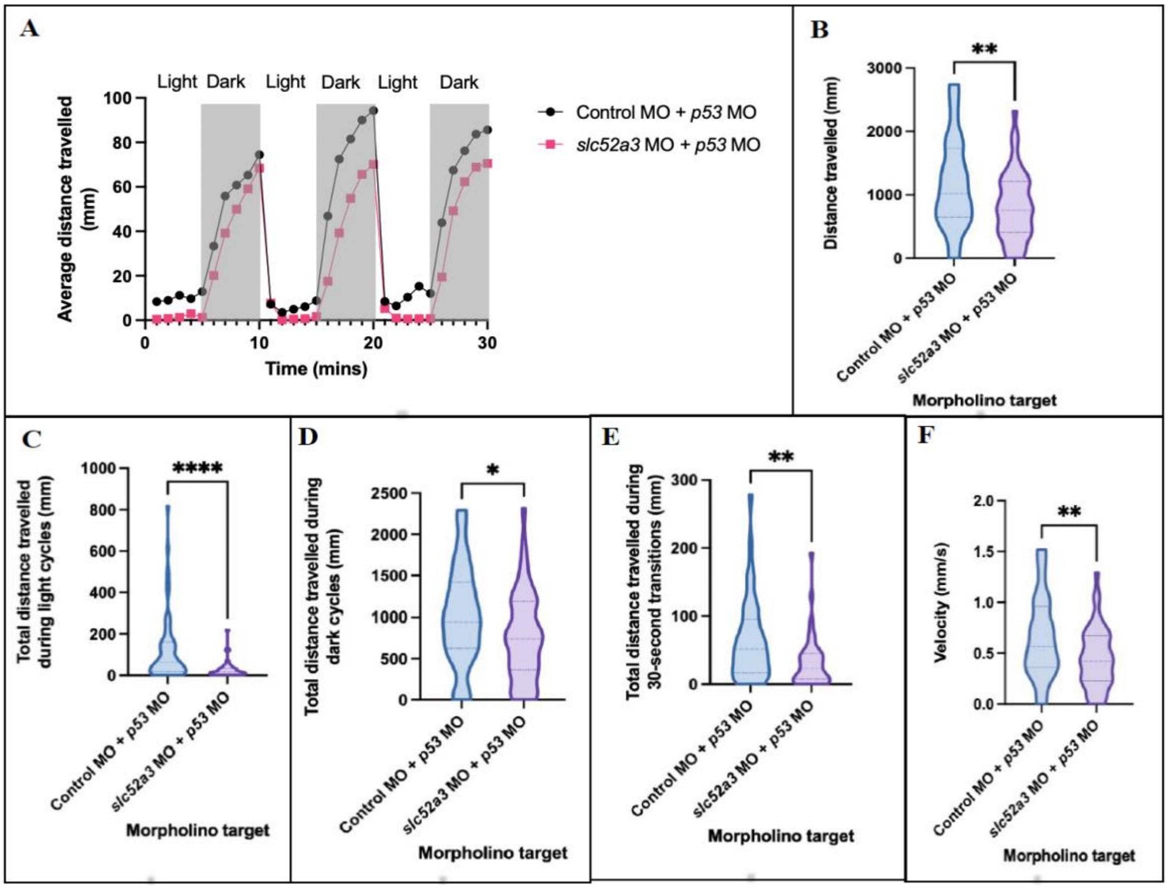

Figure 3.15 Voluntary locomotor activity performed by *slc52a3+p53* morphants during light-dark activity test at 5 dpf. (A) Average distance travelled (mm) by *slc52a3+p53* morphants per minute during light-dark activity test (Control MO+*p53* = 0.457 (0.106, 1.163), *slc52a3+p53* MO = 0.149 (0, 0.888); Mann-Whitney test). Control MO *n* = 47 *slc52a3+p53* MO *n* = 46. (B) Total distance travelled (mm) by *slc52a3+p53* morphants during light-dark activity test (Control MO+*p53* = 1171 (721.6), *slc52a3+p53* MO = 810.7 (532); Unpaired t-test). Control+*p53* MO *n* = 47 *slc52a3+p53* MO *n* = 46. (C) Total distance travelled (mm) by *slc52a3+p53* morphants during light cycles in light-dark activity test (Control MO+*p53* = 62.80 (17.9, 160.9), *slc52a3+p53* MO = 16.5 (7.575, 33.68); Mann-Whitney test). Control MO+*p53* *n* = 47 *slc52a3+p53* MO *n* = 46. (D) Total distance travelled (mm) by *slc52a3+p53* morphants during dark cycles in light-dark activity test (Control MO+*p53* = 998.6 (605), *slc52a3+p53* MO = 752.4 (538.8); Unpaired t-test). Control MO+*p53* *n* = 47 *slc52a3+p53* MO *n* = 46. (E) Total distance travelled (mm) by *slc52a3+p53* morphants during 30-second transitions between cycles in light-dark activity test (Control MO+*p53* = 51.8 (16.7, 95.3), *slc52a3+p53* MO = 23.31 (7.675, 45.18); Mann-Whitney test). Control MO+*p53* *n* = 47 *slc52a3+p53* MO *n* = 46. (E) Average velocity travelled (mm/s) by *slc52a3+p53* morphants during light-dark activity test (Control MO+*p53* = 0.651 (0.401), *slc52a3+p53* MO = 0.450 (0.296); Unpaired t-test). Control MO+*p53* *n* = 47 *slc52a3+p53* MO *n* = 46. * = $p < 0.05$, ** = $p < 0.01$, **** = $p < 0.0001$.

3.3.3 *SLC52A3* mRNA/*slc52a3* morpholino co-injection rescues the *slc52a3* morphant phenotype

To further confirm the specificity of the *slc52a3* morphant phenotype, full-length *SLC52A3* mRNA was co-injected into zebrafish embryos with slc52a3 MO, resulting in a rescue of the *slc52a3* morphant phenotype. At 3 dpf, body length, eye area, and otic vesicle area were significantly increased in co-injected embryos compared to *slc52a3* morphants (Fig. 3.17). Co-injected embryos also showed a lower total phenotype score than *slc52a3* morphants, which was attributed to a decreased spinal curvature score, and co-injected embryos exhibited a higher frequency of spontaneous movements per minute than the *slc52a3* morphants at 24 hpf (Fig. 3.17).

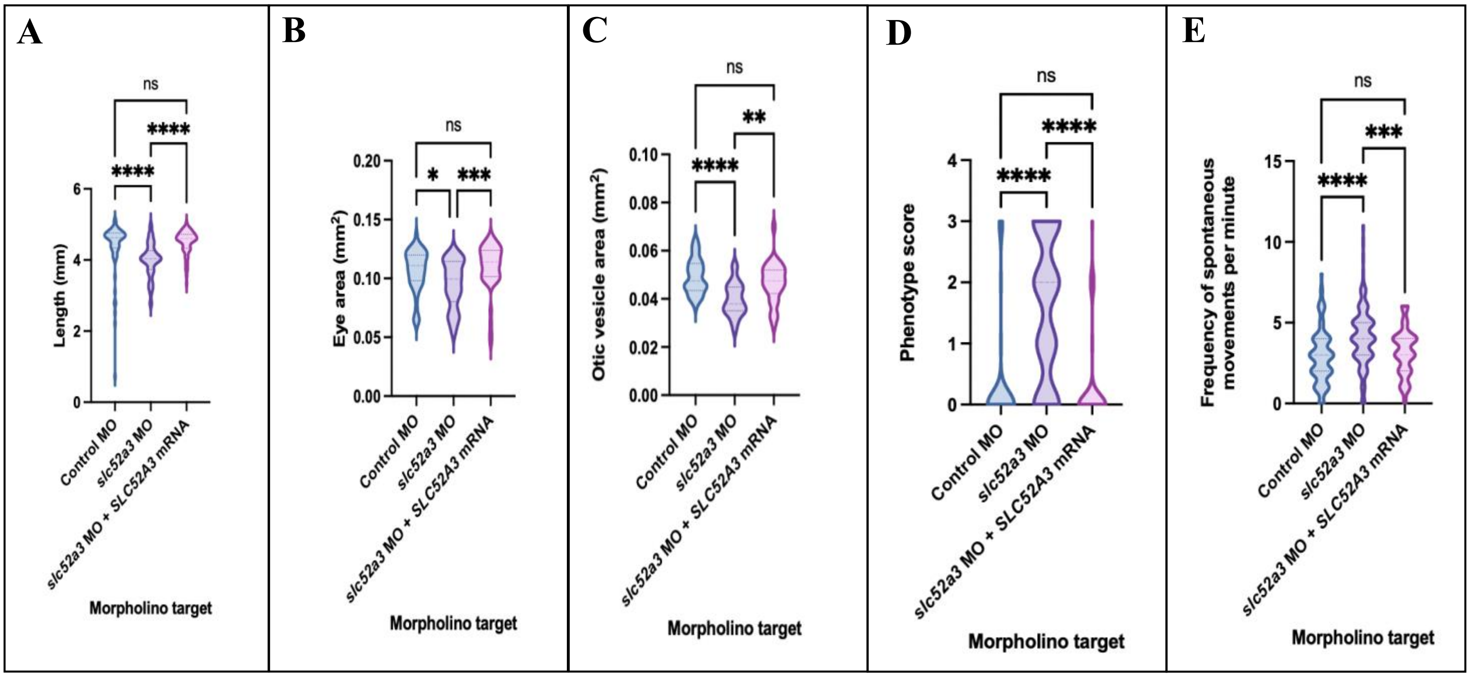

Figure 3.16 Phenotypic characteristics of *SLC52A3* mRNA/*slc52a3* MO co-injected morphants. (A) Body length (mm) of *SLC52A3* mRNA/*slc52a3* morphants (Control MO = 4.620 (4.337, 4.755), *slc52a3* MO = 4.032 (3.727, 4.264), *SLC52A3* mRNA/*slc52a3* MO = 4.595(4.332, 4.722); Kruskal-Wallis test with Dunn's multiple comparisons test). Control MO *n* = 67 *slc52a3* MO *n* = 61 *SLC52A3* mRNA/*slc52a3* MO *n* = 64 . (B) Eye area (mm^2) of *SLC52A3* mRNA/*slc52a3* morphants (Control MO = 0.111 (0.098, 0.120), *slc52a3* MO = 0.10 (0.08, 0.115), *SLC52A3* mRNA/*slc52a3* MO = 0.114(0.102, 0.124); Kruskal-Wallis test with Dunn's multiple comparisons test). Control MO *n* = 51 *slc52a3* MO *n* = 44 *SLC52A3* mRNA/*slc52a3* MO *n* = 49. (C) Otic vesicle area (mm^2) of *SLC52A3* mRNA/*slc52a3* morphants (Control MO =

0.048 (0.044, 0.055), *slc52a3* MO = 0.038 (0.035, 0.045), *SLC52A3* mRNA/*slc52a3* MO = 0.048(0.042, 0.052); Kruskal-Wallis test with Dunn's multiple comparisons test). Control MO *n* = 40 *slc52a3* MO *n* = 27 *SLC52A3* mRNA/*slc52a3* MO *n* = 32. (D) Total phenotype scores for *SLC52A3* mRNA/*slc52a3* morphants according to a scale ranking oedema and spinal curvature from 0 (normal) to 3 (severe) (Control MO = 0 (0, 2), *slc52a3* MO = 3 (1, 4), *SLC52A3* mRNA/*slc52a3* MO = 1(0, 1); Kruskal-Wallis test with Dunn's multiple comparisons test). Control MO *n* = 67 *slc52a3* MO *n* = 65 *SLC52A3* mRNA/*slc52a3* MO *n* = 65. (E) Frequency of spontaneous movements in *SLC52A3* mRNA/*slc52a3* morphants (Control MO = 3 (2, 4), *slc52a3* MO = 4 (3, 5), *SLC52A3* mRNA/*slc52a3* MO = 3(2, 4); Kruskal-Wallis test with Dunn's multiple comparisons test). Control MO *n* = 103 *slc52a3* MO *n* = 115 *SLC52A3* mRNA/*slc52a3* MO *n* = 105. ns = not significant, * = $p < 0.05$, ** = $p < 0.01$, *** = $p < 0.001$, **** = $p < 0.0001$.

At 5 dpf, *SLC52A3* mRNA/*slc52a3* MO co-injected embryos swam a greater average distance compared to *slc52a3* morphants during the light-dark activity test, as well as a greater total distance, a greater total distance during the light and dark cycles, and a greater total distance during the 30-second transition periods (Fig. 3.18). Compared to *slc52a3* morphants, *SLC52A3* mRNA/*slc52a3* MO co-injected embryos swam at a greater velocity (Fig. 3.18). From 5-7 dpf, co-injected embryos also demonstrated a higher positive response rate than *slc52a3* morphants during the acoustic startle reflex assay (Fig. 3.19). The rescue of the *slc52a3* morphant phenotype further reinforces the specificity of this model and provides more evidence that this RTD-like phenotype is not due to off-target effects of the morpholino.

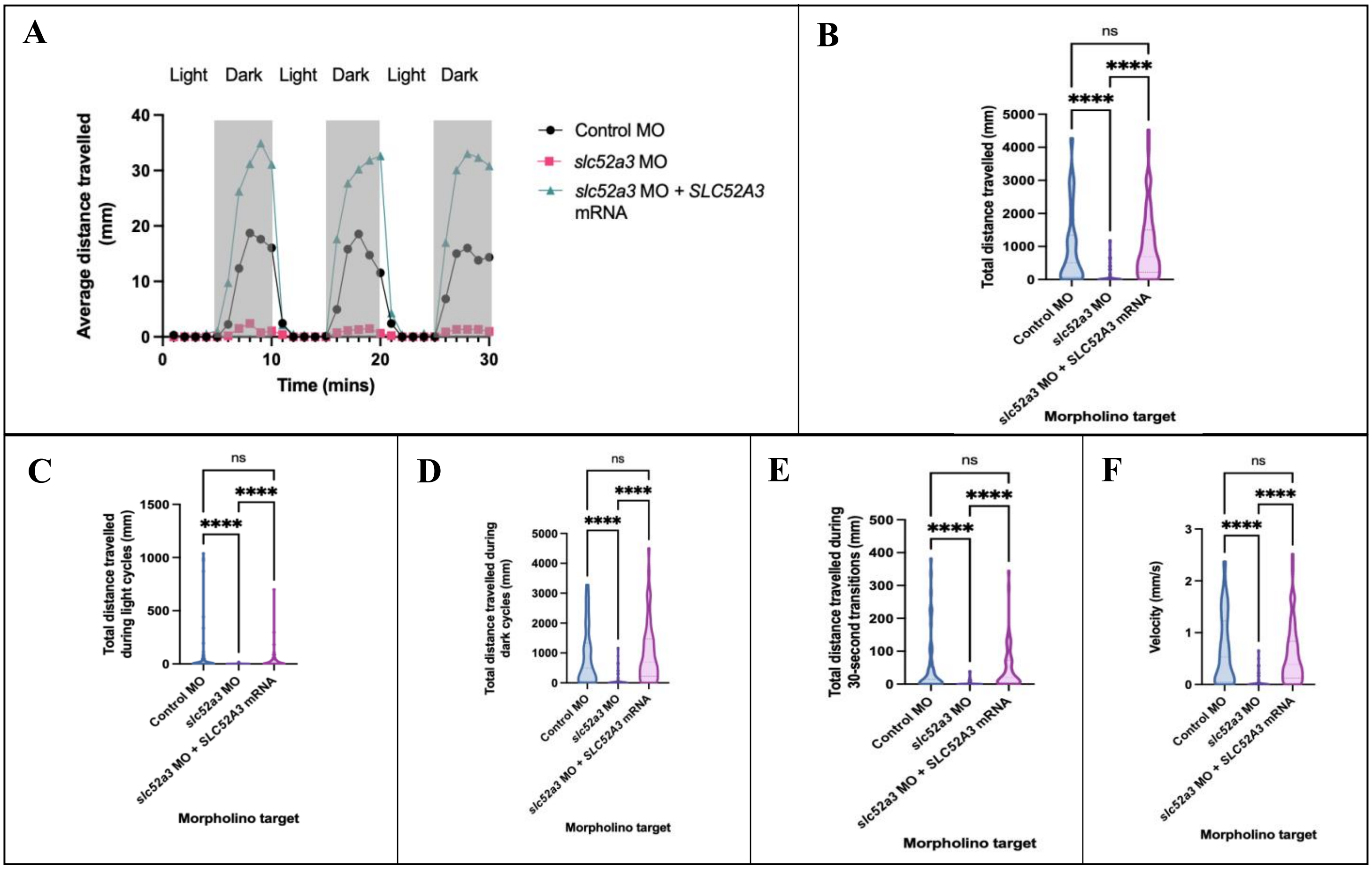

Figure 3.17 Voluntary locomotor activity performed by *SLC52A3* mRNA/*slc52a3* MO co-injected embryos during light-dark activity test at 5 dpf. (A) Average distance travelled (mm) by *slc52a3* morphants and *SLC52A3* mRNA/*slc52a3* MO co-injected embryos per minute during light-dark activity test (Control MO = 0 (0, 0.3), *slc52a3* MO = 0 (0, 0), *SLC52A3* mRNA/*slc52a3* MO = 0.081(0, 0.523); Kruskal-Wallis test with Dunn's multiple comparisons test). Control MO *n* = 56 *slc52a3* MO *n* = 55 *SLC52A3* mRNA/*slc52a3* MO *n* = 61. (B) Total distance travelled (mm) by *slc52a3* morphants and *SLC52A3* mRNA/*slc52a3* MO co-injected embryos during light-dark activity test (Control MO = 504.4 (63.10, 1343), *slc52a3* MO = 6.5 (0, 93.2), *SLC52A3* mRNA/*slc52a3* MO = 692.6(222.9, 1505); Kruskal-Wallis test with Dunn's multiple comparisons test). Control MO *n* = 56 *slc52a3* MO *n* = 55 *SLC52A3* mRNA/*slc52a3* MO *n* = 61. (C) Total distance travelled (mm) by *slc52a3* morphants and *SLC52A3* mRNA/*slc52a3* MO co-injected embryos during light cycles in light-dark activity test (Control MO = 7.7 (0, 40.25), *slc52a3* MO = 0 (0, 1.4), *SLC52A3* mRNA/*slc52a3* MO = 11.8(0, 29.8); Kruskal-Wallis test with Dunn's multiple comparisons test). Control MO *n* = 56 *slc52a3* MO *n* = 55 *SLC52A3* mRNA/*slc52a3* MO *n* = 61. (D) Total distance travelled (mm) by *slc52a3* morphants and *SLC52A3* mRNA/*slc52a3* MO co-injected embryos during dark cycles in light-dark activity test (Control MO = 497.7 (47.7, 1336), *slc52a3* MO = 4.2 (0, 93.2), *SLC52A3* mRNA/*slc52a3* MO = 692.6(222.9, 1470); Kruskal-Wallis test with Dunn's multiple comparisons test). Control MO *n* = 56 *slc52a3* MO *n* = 55 *SLC52A3* mRNA/*slc52a3* MO *n* = 61. (E) Total distance travelled (mm) by *slc52a3* morphants and *SLC52A3* mRNA/*slc52a3* MO co-injected embryos during 30-second transitions between cycles in light-dark activity test (Control MO = 14.45 (0, 51.4), *slc52a3* MO = 0 (0, 3), *SLC52A3* mRNA/*slc52a3* MO = 20.1(3.850, 71.9); Kruskal-Wallis test with Dunn's multiple comparisons test). Control MO *n* = 56 *slc52a3* MO *n* =

55 *SLC52A3* mRNA/*slc52a3* MO *n* = 61. (E) Average velocity travelled (mm/s) by *slc52a3* morphants and *SLC52A3* mRNA/*slc52a3* MO co-injected embryos during light-dark activity test (Control MO = 0.532 (0.045, 1.227), *slc52a3* MO = 0.004 (0, 0.052), *SLC52A3* mRNA/*slc52a3* MO = 0.385(0.124, 0.836); Kruskal-Wallis test with Dunn's multiple comparisons test). Control MO *n* = 56 *slc52a3* MO *n* = 55 *SLC52A3* mRNA/*slc52a3* MO *n* = 61. ns = not significant, * = p < 0.05, ** = p < 0.01, *** = p < 0.001, **** = p < 0.0001.

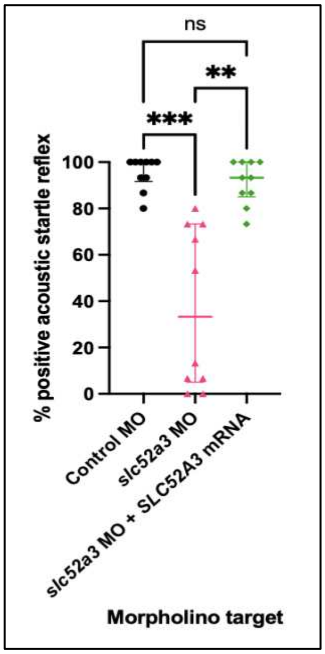

Figure 3.18 % positive acoustic startle reflex exhibited by *slc52a3* and *SLC52A3* mRNA/*slc52a3* MO co-injected zebrafish between 5-7 dpf (Control MO = 100 (91.67, 100), *slc52a3 MO* = 33.33 (85,100), *SLC52A3* mRNA/*slc52a3* MO = 93.33 (85, 100); Kruskal-Wallis test with Dunn's multiple comparisons test). Control MO *n* = 10 *slc52a3 MO n* = 10 *SLC52A3* mRNA/*slc52a3* MO *n* = 10. ** = p < 0.01, *** = p < 0.001.

3.4 CRISPR/Cas9-Mediated Mutation of *slc52a2* and *slc52a3*

3.4.1 CRISPR/Cas9-mediated mutations were successfully confirmed in *slc52a2*- and *slc52a3*-targeted embryos

To begin developing the *slc52a2* and *slc52a3* CRISPR/Cas9 knockout lines, four sgRNAs/target gene were screened for their ability to produce indels following co-injection with Cas9. The positive control group of *tyr*-targeted embryos displayed various degrees of hypopigmentation, indicating that the sgRNA/Cas9 microinjection process was successful.

CRISPR/Cas9-mediated mutations in *slc52a2* and *slc52a3* were detected using the HMA technique, which revealed multiple heteroduplex bands in each lane containing F0 crispant gDNA from *slc52a2*- and *slc52a3*-targeted embryos, compared to a single homoduplex band in lane containing wild-type gDNA (Fig. 3.20). This confirms the successful generation of indels resulting from co-injection of Cas9 with these sgRNA targets, allowing for phenotypic characterisation of the resulting crispants and enabling further development of the CRISPR/Cas9 knockout lines.

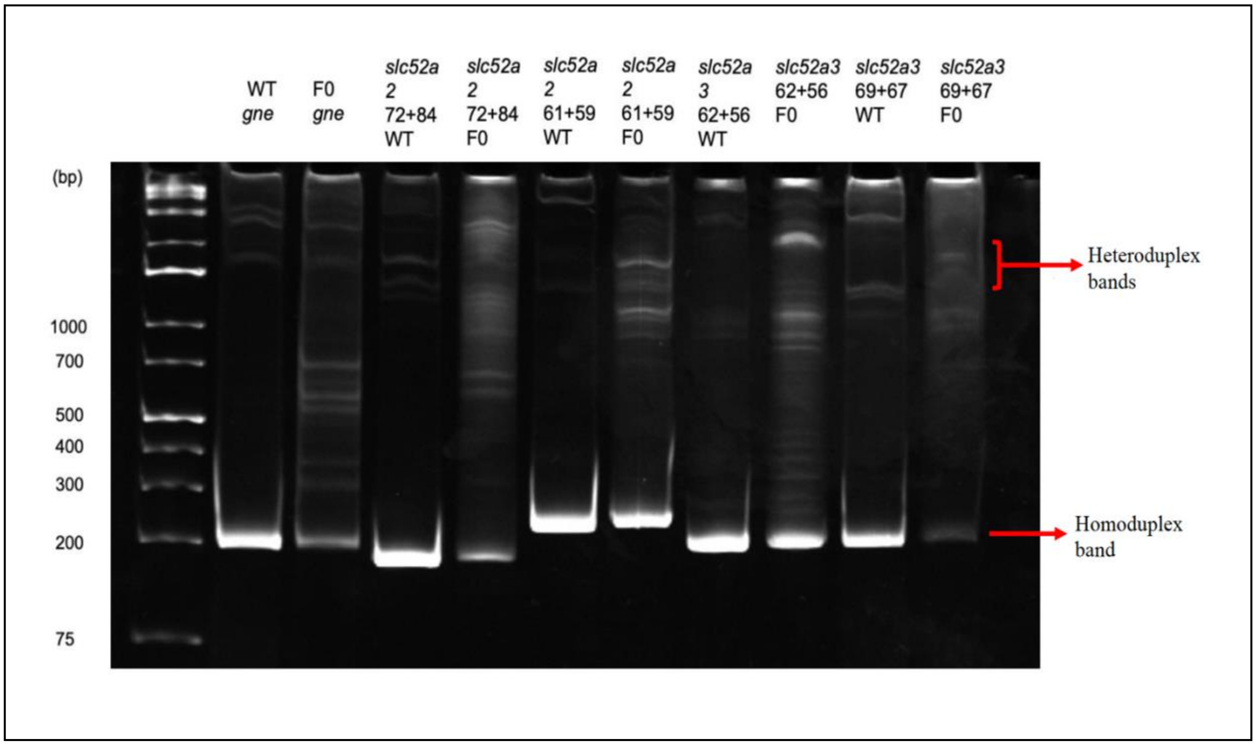

Figure 3.19 Heteroduplex mobility assay for genotyping of *slc52a2* and *slc52a3* crispants. F0 gDNA taken from *gne* crispants was used as a positive control. Each region amplified by PCR contains two sgRNA target sites (*slc52a2* targets: 72, 84, 61, 59 and *slc52a3* targets: 62, 56, 69, 67), and each of these regions is amplified from both wild-type (WT) and F0 gDNA (taken from 5 dpf-old zebrafish) to enable band pattern comparison. 500 ng of each gDNA sample were run on a 15% polyacrylamide gel.

3.4.2 *slc52a2*- and *slc52a3*-targeted F0 crispants demonstrated altered body length and/or frequency of spontaneous movements

Several morphological and behavioural assays were used to phenotypically characterise *slc52a2*- and *slc52a3*-targeted crispants. At 24 hpf, *slc52a2*-targeted F0 crispants exhibited a lower frequency of spontaneous movements per minute than *tyr*-targeted controls (Fig. 3.21). On the other hand, *slc52a3*-targeted F0 crispants demonstrated a higher frequency of spontaneous movements per minute compared to *tyr*-targeted controls (Fig. 3.21). Additionally, F0 *slc52a3*-targeted crispants displayed shorter body lengths than *tyr*-targeted controls at 3 dpf (Fig. 3.21). Overall, these results highlight the presence of RTD-like characteristics in the crispants and indicate some overlap with the *slc52a2* and *slc52a3* morphant phenotypes.

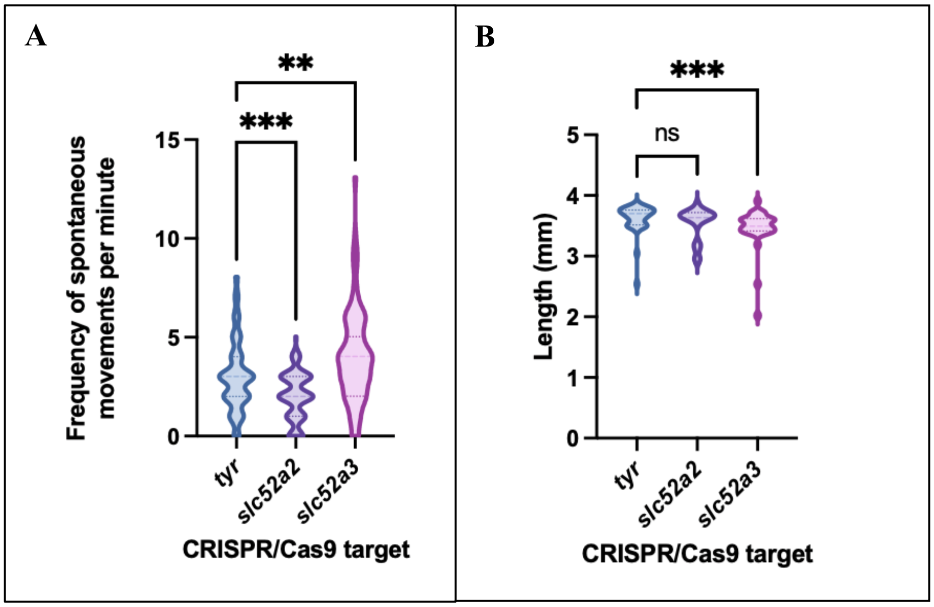

Figure 3.20 Phenotypic characteristics of *tyr-*, *slc52a2-*, and *slc52a3-targeted* crispants. (A) Frequency of spontaneous movements in *slc52a2* crispants and *slc52a3* crispants at 24 hpf (*tyr* = 3.015 (2.01, 4.02), *slc52a2* = 2.012 (1.006, 3.017), *slc52a3* = 4.026 (2.014, 5.035); Kruskal-Wallis test with Dunn's multiple comparisons test). *tyr n* = 102 *slc52a2 n* = 91 *slc52a3 n* = 91. (B) Body length (mm) of *slc52a2* crispants and *slc52a3* crispants (*tyr* = 3.7 (3.515, 3.760), *slc52a2* = 3.635 (3.445, 3.720), *slc52a3* = 3.495 (3.415, 3.620); Kruskal-Wallis test with Dunn's multiple comparisons test). *tyr n* = 37 *slc52a2 n* = 22 *slc52a3 n* = 30. ns = not significant, ** = $p < 0.01$, *** = $p < 0.001$.

3.5 Therapeutic Screening of Riboflavin and Probenecid

3.5.1 OAT-3 and oat-3 Have Similar Predicted Protein Structures

To determine whether riboflavin and probenecid may interact similarly with human OAT-3 and zebrafish oat-3, the three-dimensional structures of human OAT-3 and zebrafish oat-3 were predicted by ColabFold. The top-ranked OAT-3 protein structure prediction generated by ColabFold had a pLDDT score of 85.2, and the top-ranked oat-3 protein structure prediction had a pLDDT score of 83.8 (Fig. 3.22). Using the "super" command in PyMOL, the two predicted protein structures were superimposed and a rmsd score of 0.520 Å was calculated (Fig. 3.22). This indicates high similarity between human OAT-3 and zebrafish oat-3 predicted protein structures.

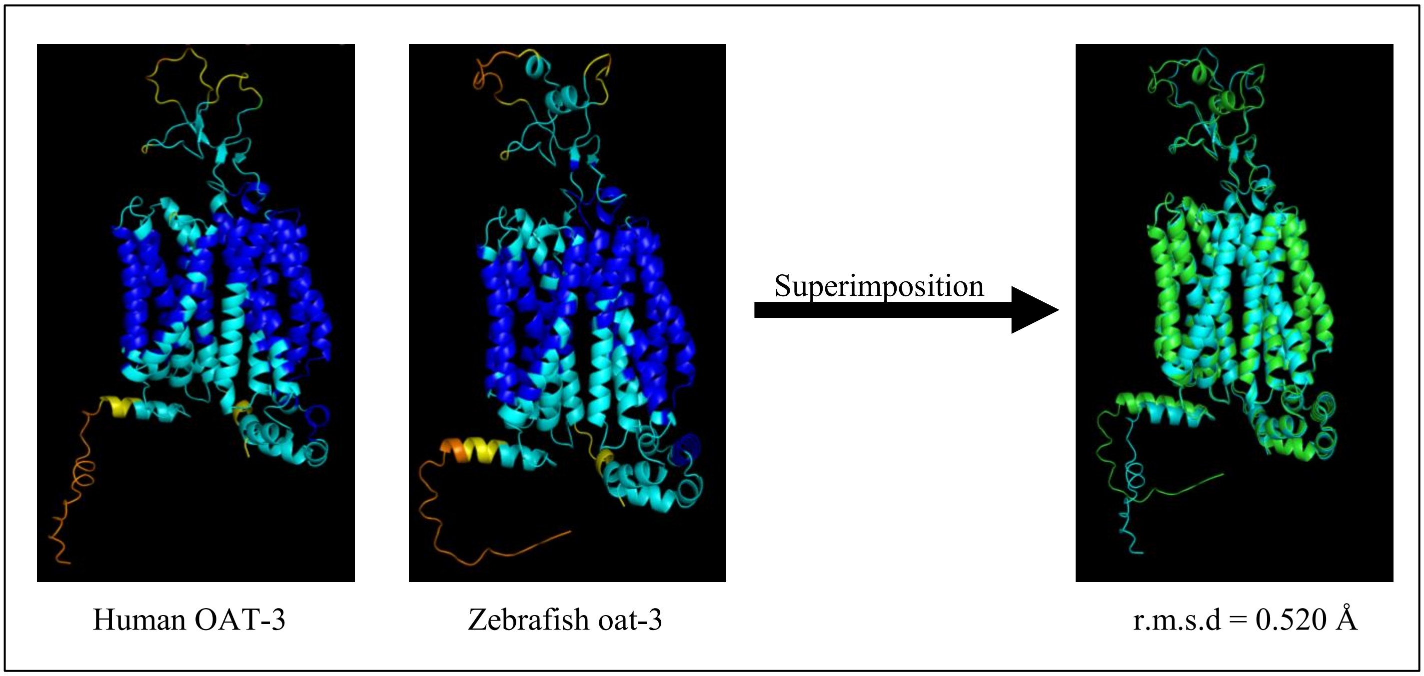

Figure 3.21 Human OAT-3 and zebrafish oat-3 protein structure predictions produced by ColabFold. Both structures were superimposed to calculate the r.m.s.d score (human OAT-3 in green and zebrafish oat-3 in blue). Individual protein structures are colour-coded by pLDDT score (dark blue: high score, light blue: confident score, yellow: low score, orange: very low score)[94].

3.5.2 OAT-3 and oat-3 Ligand Docking Reveals Similar Sites of Interaction

Following protein structure prediction, the interactions of riboflavin and probenecid with human OAT-3 and zebrafish oat-3 were further examined by individually docking both ligands onto both predicted protein structures using SwissDock. Considering the top 3 OAT-3-riboflavin poses, riboflavin docked to a similar region on both OAT-3 and oat-3 (Fig. 3.23). Probenecid was predicted to interact with OAT-3 at a different region compared to riboflavin, and this predicted region of interaction was similar across all top 3 OAT-3-probenecid poses (Fig. 3.24). However, while the top-ranked oat-3-probenecid pose showed probenecid docking to a similar site as on OAT-3, probenecid was found to dock to a different region in the second and third oat-3-probenecid poses (Fig. 3.24). These results indicate the potential for riboflavin and probenecid to interact similarly with both human OAT-3 and zebrafish oat-3, but drug screening is needed to properly determine the extent of the similarity between these protein-ligand interactions.

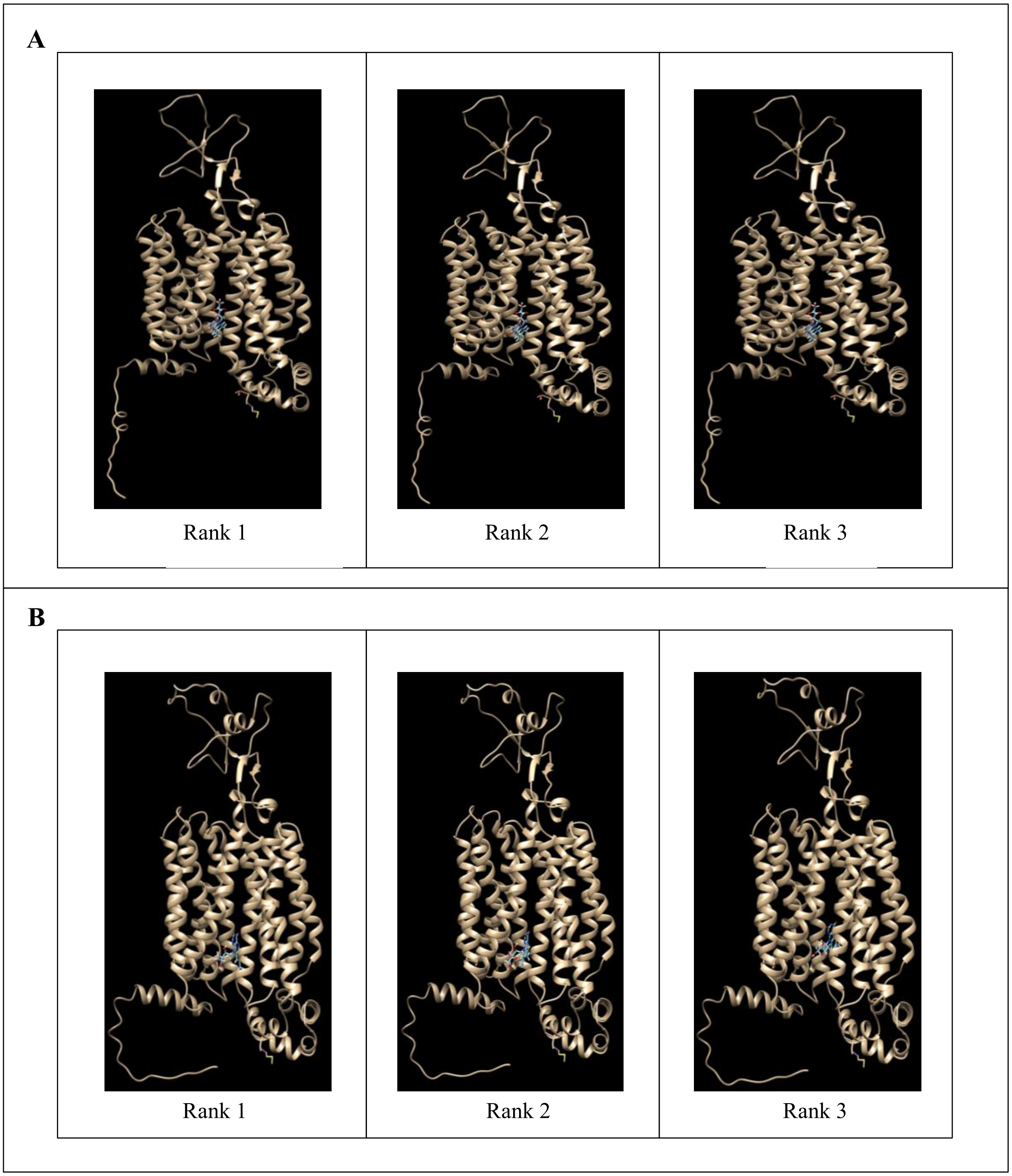

Figure 3.22 Top docking positions for riboflavin on (A) OAT-3 and (B) oat-3. Poses were simulated using SwissDock and ranked in order of ascending Gibbs free energy change (ΔG) from rank 1-3.

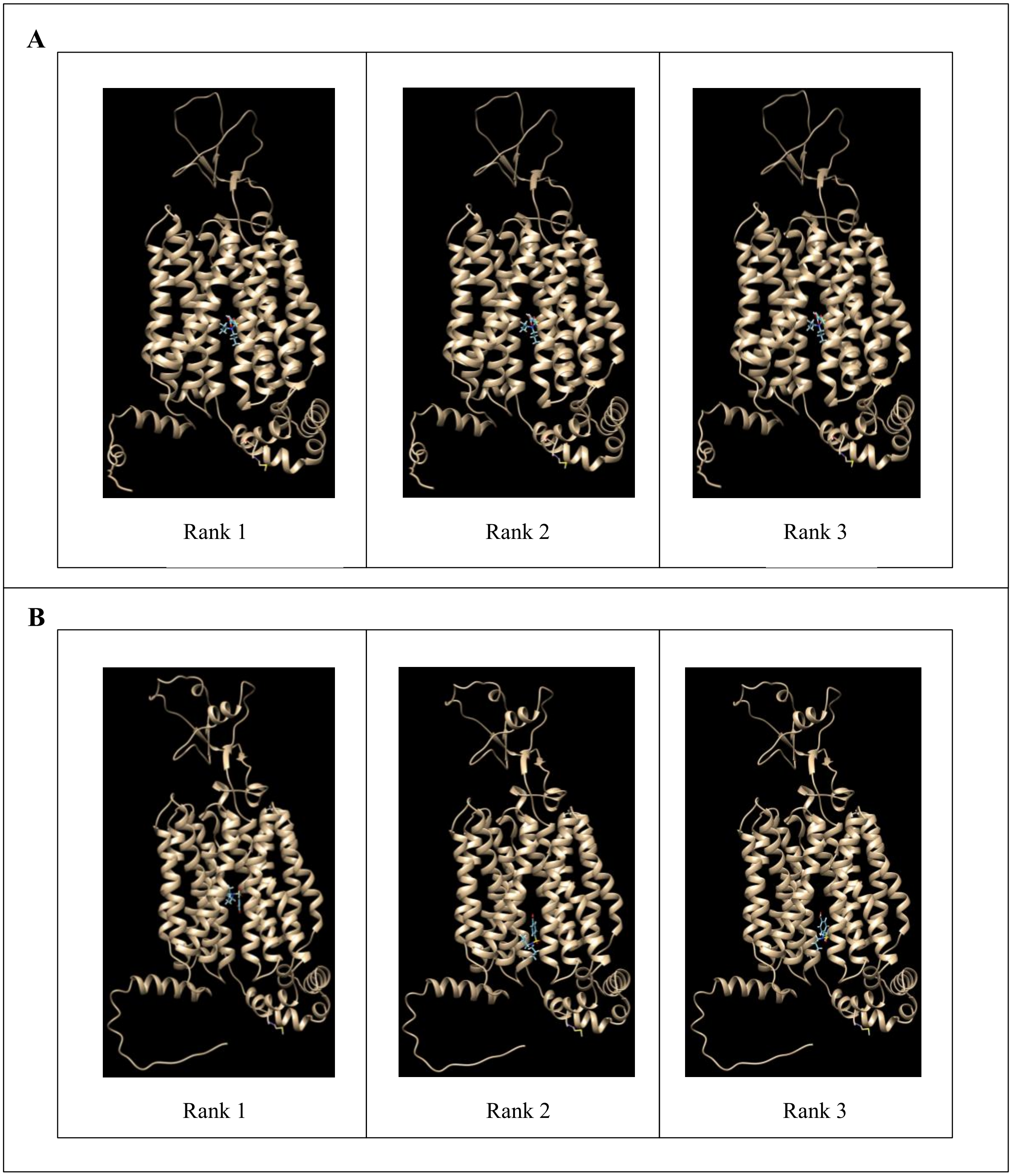

Figure 3.23 Top docking positions for probenecid on (A) OAT-3 and (B) oat-3. Poses were simulated using SwissDock and ranked in order of ascending Gibbs free energy change (ΔG) from rank 1-3.

3.5.3 Therapeutic Screening of Riboflavin and Probenecid in HEK-293T Cells

To establish non-toxic dosages of riboflavin and probenecid, several concentrations of each drug were used to treat HEK-293T cells. Following both 1.5 hours and 24 hours of exposure, none of the concentrations of riboflavin tested significantly affected survival of HEK-293T cells, as measured by the trypan blue assay (Fig. 3.25A, Fig. 3.25B). Conversely, following 24 hours of exposure, 10 mM of probenecid was shown to significantly decrease HEK-293T cell survival (Fig. 3.25C). Riboflavin dosages of 0.1 μM to 100 μM and probenecid dosages of 1 μM to 1 mM were therefore identified as non-toxic and used in subsequent *in vivo* drug screening experiments.

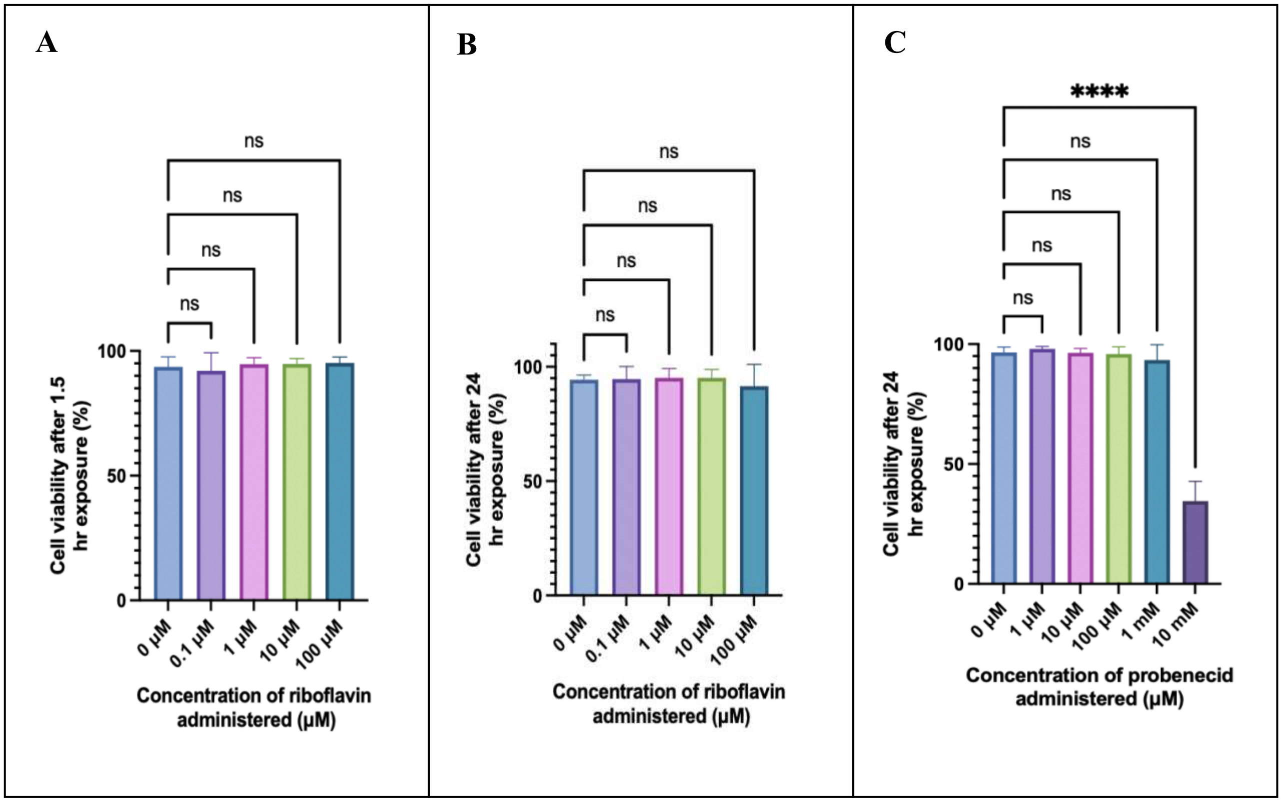

Figure 3.24 % HEK-293T cell viability following exposure to riboflavin or probenecid. (A) 1.5 hours of exposure to riboflavin (0 μM = 93.6 (4.037), 0.1 μM = 92 (7.254), 1 μM = 94.7 (2.564), 10 μM = 94.8 (2.197), 100 μM = 95.2 (2.308); One-way ANOVA with multiple comparisons). 0 μM *n* = 3 0.1 μM *n* = 3 1 μM *n* = 3 10 μM *n* = 3 100 μM *n* = 3. (B) 24 hours of exposure to riboflavin (0 μM = 94.33 (2.082), 0.1 μM = 94.67 (5.485), 1 μM = 95.17 (4.072), 10 μM = 95.17 (3.686), 100 μM = 91.5 (9.579); One-way ANOVA with multiple comparisons). 0 μM *n* = 3 0.1 μM *n* = 3 1 μM *n* = 3 10 μM *n* = 3 100 μM *n* = 3. (C) 24 hours of exposure to probenecid (0 μM = 96.5 (2.291), 1 μM = 98 (1), 10 μM = 96.33 (1.893), 100 μM = 95.83 (3.055), 1 mM = 93.33

(6.429), 10 mM = 34.5 (8.322); One-way ANOVA with multiple comparisons). 0 µM *n* = 3 1 µM *n* = 3 10 µM *n* = 3 100 µM *n* = 3 1 mM *n* = 3 10 mM *n* = 3. Cell viability was measured using the trypan blue assay. ns = not significant, **** = $p < 0.0001$. One-way ANOVA with multiple comparisons).

3.5.4 Therapeutic Screening of Riboflavin and Probenecid in Wild-type Zebrafish

To ensure that the dose ranges previously identified in HEK-293T cells are non-toxic in zebrafish, these dose ranges for riboflavin and probenecid were used to treat wild-type zebrafish from 0-4 dpf. Similarly to the results obtained in HEK-293T cells, all zebrafish treated with all concentrations of riboflavin survived for the duration of the trial (Fig. 3.26). Zebrafish treated with between 1-100 µM of probenecid demonstrated a survival rate of >90% by the end of the trial, while only 64.4% of zebrafish treated with 1 mM of probenecid survived for the entire trial and all zebrafish treated with 10 mM of probenecid died within 24 hours of the first treatment (Fig. 3.26). These results mostly corroborate the findings obtained in HEK-293T cells. However, 1 mM of probenecid was found to impact zebrafish survival, so this dosage was excluded from the range for future therapeutic screening.

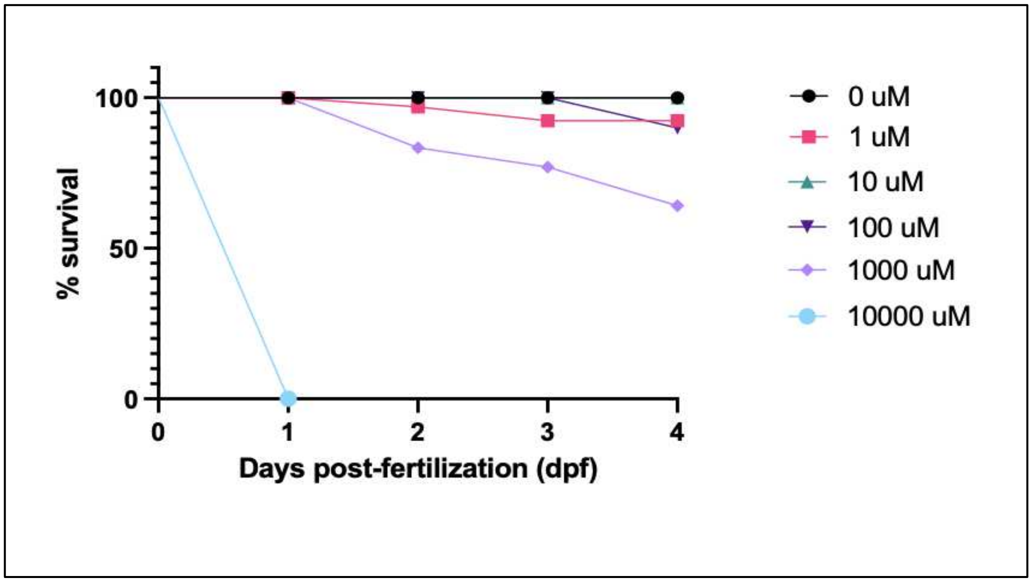

Figure 3.25 % survival of wild-type zebrafish in response to various concentrations of riboflavin or probenecid from 0-4 dpf. Riboflavin 0 µM *n* = 11 0.1 µM *n* = 10 1 µM *n* = 11 10 µM *n* = 12 100 µM *n* = 12. Probenecid 0 µM *n* = 11 1 µM *n* = 12 10 µM *n* = 11 100 µM *n* = 10 1 mM *n* = 11 10 mM *n* = 11.

3.5.5 Therapeutic Screening of Riboflavin and Probenecid in *slc52a3* knockdown Zebrafish

To explore the potential amelioration of the RTD-like phenotype in *slc52a3* morphants in response to riboflavin and/or probenecid treatment, these drugs were used to treat *slc52a3* morphants from 0-7 dpf. Following dose-response experiments, it was decided that 100 µM of riboflavin and 200 µM of probenecid were optimal non-toxic drug dosages for therapeutic screening. These dosages were tested individually on zebrafish from 0-5 dpf, but this testing resulted in minimal improvement to the RTD-like phenotype in the zebrafish. Riboflavin-treated *slc52a3* knockdown fish demonstrated a non-significant increase in body length, increase in otic vesicle area and reduction in spinal curvature (Figure 3.27). Conversely, probenecid treatment did not result in any morphological ameliorations to the RTD-like phenotype (Figure 3.28). Riboflavin-treated fish also exhibited a significant increase in average distance travelled compared to *slc52a3* knockdown fish at 5 dpf during the light-dark activity test, as well as non-significant increases in total distance travelled, total distance travelled during light cycles, and average velocity (Figure 3.29). While probenecid-treated fish swam a significantly greater average distance compared to *slc52a3* knockdown fish during the light-dark activity test, they did not show any other improvements to the locomotor phenotype (Figure 3.30). Therefore, riboflavin exerts a minimal and largely non-significant morphological and behavioural benefit on *slc52a3* morphants, and probenecid-treated fish only demonstrated an increase in average distance travelled compared to *slc52a3* morphants.

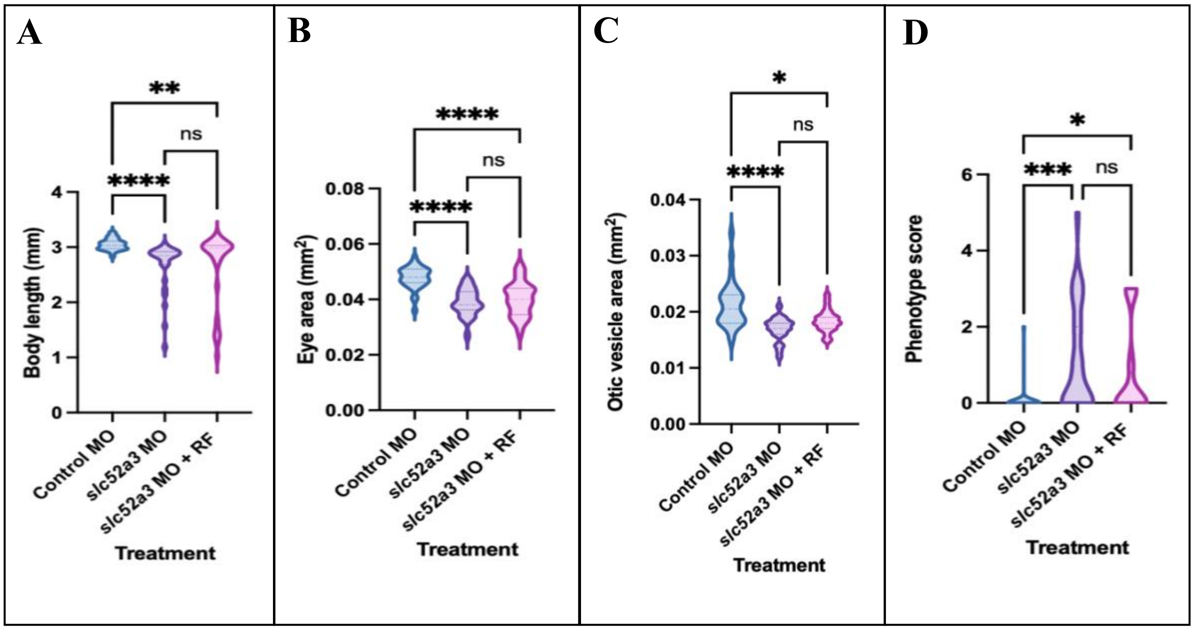

Figure 3.26 Phenotypic characteristics of *slc52a3* MO and riboflavin-treated *slc52a3* MO zebrafish. (A) Body length (mm) of *slc52a3* MO and riboflavin-treated *slc52a3* MO zebrafish (Control MO = 3.033(2.971, 3.107), *slc52a3* MO = 2.845(2.685, 2.919), riboflavin-treated *slc52a3* MO = 2.984(2.607, 3.033); Kruskal-Wallis test with Dunn's multiple comparisons test). Control MO $n = 35$ *slc52a3* MO $n = 27$ riboflavin-treated *slc52a3* MO $n = 30$. (B) Eye area (mm^2) of *slc52a3* MO and riboflavin-treated *slc52a3* MO zebrafish (Control MO = 0.048 (0.004), *slc52a3* MO = 0.039 (0.005), riboflavin-treated *slc52a3* MO = 0.04(0.006); One-way ANOVA with multiple comparisons). Control MO $n = 34$ *slc52a3* MO $n = 24$ riboflavin-treated *slc52a3* MO $n = 28$. (C) Otic vesicle area (mm^2) of *slc52a3* MO and riboflavin-treated *slc52a3* MO zebrafish (Control MO = 0.021(0.018, 0.023), *slc52a3* MO = 0.017(0.016, 0.018), riboflavin-treated *slc52a3* MO = 0.018(0.017, 0.019); Kruskal-Wallis test with Dunn's multiple comparisons test). Control MO $n = 30$ *slc52a3* MO $n = 22$ riboflavin-treated *slc52a3* MO $n = 23$. (D) Total phenotype scores for *slc52a3* MO and riboflavin-treated *slc52a3* MO zebrafish according to a scale ranking oedema and spinal curvature from 0 (normal) to 3 (severe) (Control MO = 0(0,0), *slc52a3* MO = 0(0, 2), riboflavin-treated *slc52a3* MO = 0(0, 1.5); Kruskal-Wallis test with Dunn's multiple comparisons test). Control MO $n = 35$ *slc52a3* MO $n = 27$ riboflavin-treated *slc52a3* MO $n = 30$. ns = not significant, * = $p < 0.05$, ** = $p < 0.01$, *** = $p < 0.001$, **** = $p < 0.0001$.

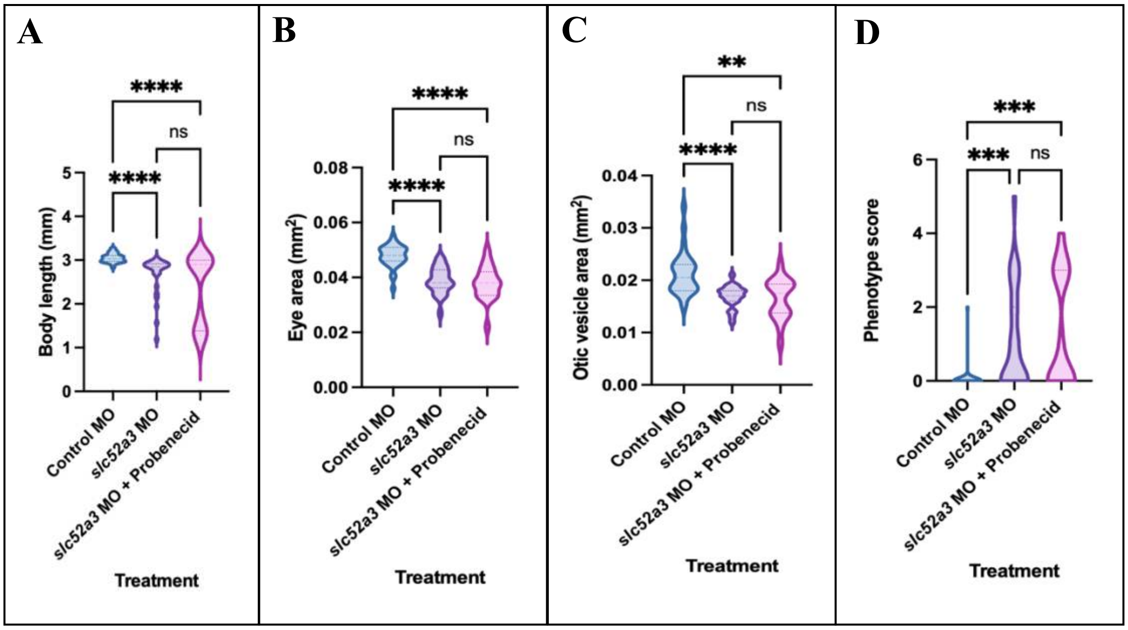

Figure 3.27 Phenotypic characteristics of *slc52a3* MO and probenecid-treated *slc52a3* MO zebrafish. (A) Body length (mm) of *slc52a3* MO and probenecid-treated *slc52a3* MO zebrafish (Control MO = 3.033(2.971, 3.107), *slc52a3* MO = 2.845(2.685, 2.919), probenecid-treated *slc52a3* MO = 2.903(1.386, 2.998); Kruskal-Wallis test with Dunn's multiple comparisons test). Control MO *n* = 35 *slc52a3* MO *n* = 27 probenecid -treated *slc52a3* MO *n* = 28. (B) Eye area (mm^2) of *slc52a3* MO and probenecid-treated *slc52a3* MO zebrafish (Control MO = 0.048(0.004), *slc52a3* MO = 0.039(0.005), probenecid-treated *slc52a3* MO = 0.038(0.006); One-way ANOVA with multiple comparisons). Control MO *n* = 34 *slc52a3* MO *n* = 24 probenecid-treated *slc52a3* MO *n* = 21. (C) Otic vesicle area (mm^2) of *slc52a3* MO and probenecid-treated *slc52a3* MO zebrafish (Control MO = 0.021(0.018, 0.023), *slc52a3* MO = 0.017(0.016, 0.018), probenecid-treated *slc52a3* MO = 0.018(0.014, 0.019); Kruskal-Wallis test with Dunn's multiple comparisons test). Control MO *n* = 30 *slc52a3* MO *n* = 22 probenecid-treated *slc52a3* MO *n* = 18. (D) Total phenotype scores for *slc52a3* MO and probenecid-treated *slc52a3* MO zebrafish according to a scale ranking oedema and spinal curvature from 0 (normal) to 3 (severe) (Control MO = 0(0, 0), *slc52a3* MO = 0(0, 2), probenecid-treated *slc52a3* MO = 0(0, 3); Kruskal-Wallis test with Dunn's multiple comparisons test). Control MO *n* = 35 *slc52a3* MO *n* = 27 probenecid-treated *slc52a3* MO *n* = 28. ns = not significant, ** = $p < 0.01$, **** = $p < 0.0001$.

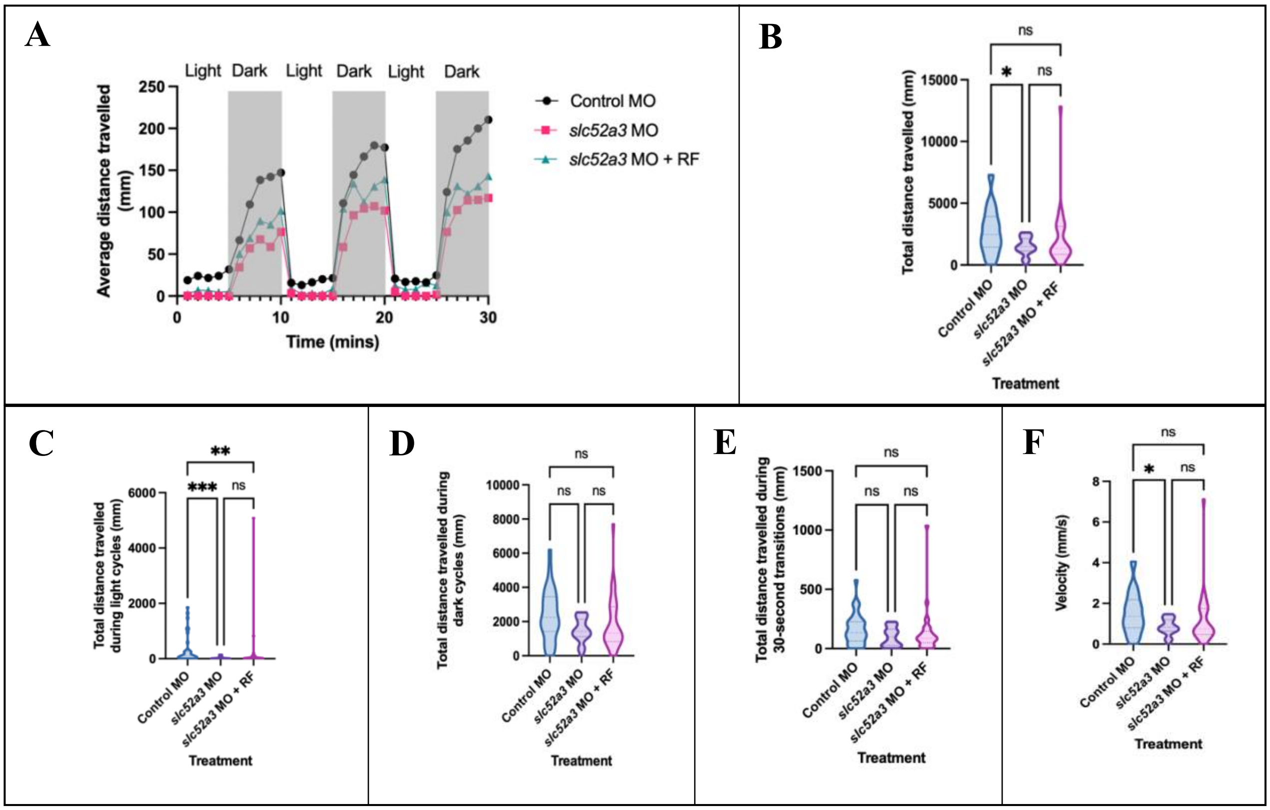

Figure 3.28 Voluntary locomotor activity performed by riboflavin-treated *slc52a3* MO embryos during light-dark activity test at 5 dpf. (A) Average distance travelled (mm) by *slc52a3* MO and riboflavin-treated *slc52a3* MO embryos per minute during light-dark activity test (Control MO = 1.025(0.25, 2.588), *slc52a3* MO = 0.15(0, 1.55), riboflavin-treated *slc52a3* MO = 0.6(0, 1.95); Kruskal-Wallis test with Dunn's multiple comparisons test). Control MO *n* = 35 *slc52a3* MO *n* = 24 riboflavin-treated *slc52a3* MO *n* = 30. (B) Total distance travelled (mm) by *slc52a3* MO and riboflavin-treated *slc52a3* MO embryos during light-dark activity test (Control MO = 2470(1448, 3928), *slc52a3* MO = 1489(1146, 2137), riboflavin-treated *slc52a3* MO = 1347(852, 3132); Kruskal-Wallis test with Dunn's multiple comparisons test). Control MO *n* = 35 *slc52a3* MO *n* = 24 riboflavin-treated *slc52a3* MO *n* = 30. (C) Total distance travelled (mm) by *slc52a3* MO and riboflavin-treated *slc52a3* MO embryos during light cycles in light-dark activity test (Control MO = 101.5(34.3, 262), *slc52a3* MO = 11.7 (5.1, 46.13), riboflavin-treated *slc52a3* MO = 18.8(8.85, 76.35); Kruskal-Wallis test with Dunn's multiple comparisons test). Control MO *n* = 35 *slc52a3* MO *n* = 24 riboflavin-treated *slc52a3* MO *n* = 30. (D) Total distance travelled (mm) by *slc52a3* MO and riboflavin-treated *slc52a3* MO embryos during dark cycles in light-dark activity test (Control MO = 2246(1419, 3443), *slc52a3* MO = 1425(1118, 2130), riboflavin-treated *slc52a3* MO = 1329(832.3, 2867); Kruskal-Wallis test with Dunn's multiple comparisons test). Control MO *n* = 35 *slc52a3* MO *n* = 24 riboflavin-treated *slc52a3* MO *n* = 30. (E) Total distance travelled (mm) by *slc52a3* MO and riboflavin-treated *slc52a3* MO embryos during 30-second transitions between cycles in light-dark activity test (Control MO = 134(64.2, 226.6), *slc52a3* MO = 98(25.6, 164.5), riboflavin-treated *slc52a3* MO = 88.2(49.85, 145.6); Kruskal-Wallis test with Dunn's multiple comparisons test). Control MO *n* = 35 *slc52a3* MO *n* = 25 riboflavin-treated *slc52a3* MO *n* = 30. (E) Average velocity travelled (mm/s) by *slc52a3* MO and riboflavin-treated *slc52a3* MO embryos during light-dark activity test (Control

MO = 1.372(0.804, 2.182), *slc52a3* MO = 0.83(0.64, 1.19), riboflavin-treated *slc52a3* MO = 0.749(0.474, 1.74); Kruskal-Wallis test with Dunn's multiple comparisons test). Control MO *n* = 35 *slc52a3* MO *n* = 24 riboflavin-treated *slc52a3* MO *n* = 30. ns = not significant, * = $p < 0.05$, ** = $p < 0.01$, *** = $p < 0.001$, **** = $p < 0.0001$.

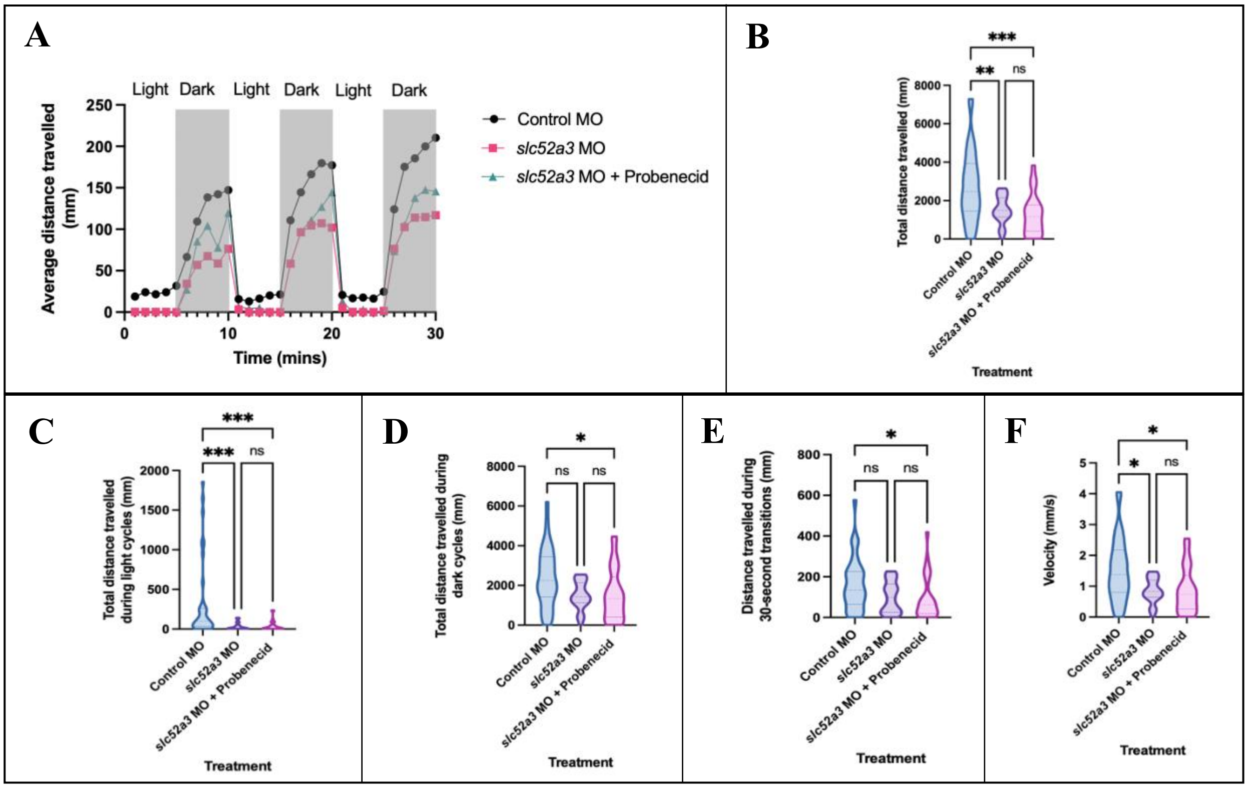

Figure 3.29 Voluntary locomotor activity performed by probenecid-treated *slc52a3* MO embryos during light-dark activity test at 5 dpf. (A) Average distance travelled (mm) by *slc52a3* MO and probenecid-treated *slc52a3* MO embryos per minute during light-dark activity test (Control MO = 1.025(0.25, 2.588), *slc52a3* MO = 0.15(0, 1.55), probenecid-treated *slc52a3* MO = 0.3(0, 1.75); Kruskal-Wallis test with Dunn's multiple comparisons test). Control MO *n* = 35 *slc52a3* MO *n* = 24 probenecid -treated *slc52a3* MO *n* = 26. (B) Total distance travelled (mm) by *slc52a3* MO and probenecid-treated *slc52a3* MO embryos during light-dark activity test (Control MO = 2470(1448, 3928), *slc52a3* MO = 1489(1146, 2137), probenecid-treated *slc52a3* MO = 1162(407.9, 1769); Kruskal-Wallis test with Dunn's multiple comparisons test). Control MO *n* = 35 *slc52a3* MO *n* = 24 probenecid -treated *slc52a3* MO *n* = 26. (C) Total distance travelled (mm) by *slc52a3* MO and probenecid-treated *slc52a3* MO embryos during light cycles in light-dark activity test (Control MO = 101.5(34.3, 262), *slc52a3* MO = 11.7(5.1, 46.13), probenecid-treated *slc52a3* MO = 13.2(4.65, 52.95); Kruskal-Wallis test with Dunn's multiple comparisons test). Control MO *n* = 35 *slc52a3* MO *n* = 24 probenecid -treated *slc52a3* MO *n* = 29. (D) Total distance travelled (mm) by *slc52a3* MO and probenecid-treated *slc52a3* MO embryos during dark cycles in light-dark activity test (Control MO = 2246(1419, 3443), *slc52a3* MO = 1425(1118, 2130), probenecid-treated *slc52a3* MO = 1335(400.2, 2429); Kruskal-Wallis test with Dunn's multiple comparisons test). Control MO *n* = 35 *slc52a3* MO *n* = 24 probenecid -treated *slc52a3* MO *n* = 29. (E) Total distance travelled (mm) by *slc52a3* MO and probenecid-treated *slc52a3* MO embryos during 30-second transitions between cycles in light-dark activity test (Control MO = 134(64.2, 226.6), *slc52a3* MO = 98(25.6, 164.5), probenecid-treated *slc52a3* MO = 62.3(19.55, 142);

Kruskal-Wallis test with Dunn's multiple comparisons test). Control MO $n = 35$ *slc52a3* MO $n = 25$ probenecid -treated *slc52a3* MO $n = 29$. (E) Average velocity travelled (mm/s) by *slc52a3* MO and probenecid-treated *slc52a3* MO embryos during light-dark activity test (Control MO = 1.372(0.804, 2.182), *slc52a3* MO = 0.83(0.64, 1.19), probenecid-treated *slc52a3* MO = 0.741(0.255, 1.351); Kruskal-Wallis test with Dunn's multiple comparisons test). Control MO $n = 35$ *slc52a3* MO $n = 24$ probenecid -treated *slc52a3* MO $n = 29$. ns = not significant, * = $p < 0.05$, ** = $p < 0.01$, *** = $p < 0.001$, **** = $p < 0.0001$.

To assess whether co-treatment of *slc52a3* knockdown fish with riboflavin and probenecid may exert a synergistic effect on the RTD-like phenotype, a combination of 100 uM of riboflavin and 200 uM of probenecid was then used to treat *slc52a3* knockdown fish from 0-5 dpf. However, combined treatment of riboflavin and probenecid failed to ameliorate most features of the *slc52a3* morphant phenotype. Riboflavin/probenecid co-treated *slc52a3* morphants exhibited a non-significant decrease in body length and non-significant increases in eye area and otic vesicle area (Figure 3.31). However, co-treated *slc52a3* morphants also demonstrated a significant reduction in average distance travelled during the light-dark activity test compared to control morphants and untreated *slc52a3* morphants, as well as non-significant reductions in total distance travelled, total distance travelled during light cycles, total distance travelled during dark cycles, total distance travelled during 30-second transitions, and average velocity (Figure 3.32). Finally, riboflavin/probenecid co-treated *slc52a3* morphants showed a non-significant decrease in % positive acoustic startle reflex between 5-7 dpf compared to untreated *slc52a3* morphants (Figure 3.33). These results indicate that the combination of riboflavin and probenecid does not exert a synergistic effect on the slc52a3 knockdown phenotype, as the RTD-like characteristics of the model either remained unchanged or worsened in response to the treatment. However, larger sample sizes and potentially more doses are needed to confirm these findings.

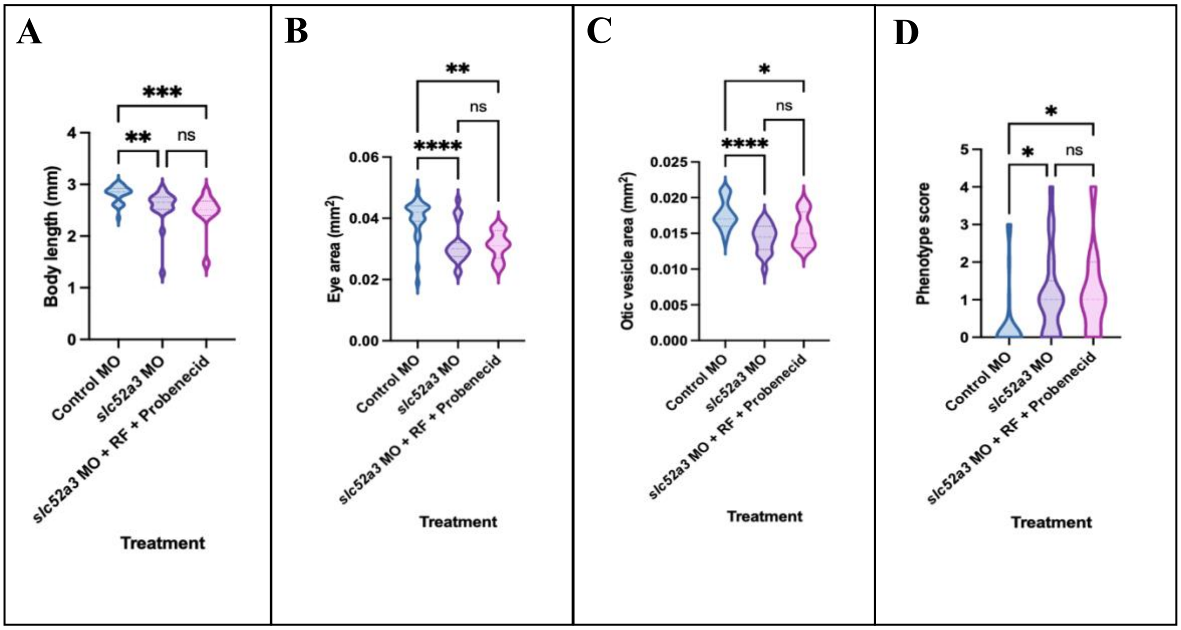

Figure 3.30 Phenotypic characteristics of *slc52a3* MO and riboflavin/probenecid co-treated *slc52a3* MO zebrafish. (A) Body length (mm) of *slc52a3* MO and riboflavin/probenecid co-treated *slc52a3* MO zebrafish (Control MO = 2.856(2.695, 2.925), *slc52a3* MO = 2.657(2.518, 2.754), riboflavin/probenecid co-treated *slc52a3* MO = 2.509(2.397, 2.679); Kruskal-Wallis test with Dunn's multiple comparisons test). Control MO *n* = 28 *slc52a3* MO *n* = 21 riboflavin/probenecid co-treated *slc52a3* MO *n* = 11. (B) Eye area (mm^2) of *slc52a3* MO and riboflavin/probenecid co-treated *slc52a3* MO zebrafish (Control MO = 0.042(0.039, 0.044), *slc52a3* MO = 0.03(0.028, 0.032), riboflavin/probenecid co-treated *slc52a3* MO = 0.031(0.027, 0.036); Kruskal-Wallis test with Dunn's multiple comparisons test). Control MO *n* = 28 *slc52a3* MO *n* = 21 riboflavin/probenecid co-treated *slc52a3* MO *n* = 11. (C) Otic vesicle area (mm^2) of *slc52a3* MO and riboflavin/probenecid co-treated *slc52a3* MO zebrafish (Control MO = 0.017(0.016, 0.019), *slc52a3* MO = 0.015(0.013, 0.016), riboflavin/probenecid co-treated *slc52a3* MO = 0.015(0.013, 0.018); Kruskal-Wallis test with Dunn's multiple comparisons test). Control MO *n* = 26 *slc52a3* MO *n* = 18 riboflavin/probenecid co-treated *slc52a3* MO *n* = 11. (D) Total phenotype scores for *slc52a3* MO and riboflavin/probenecid co-treated *slc52a3* MO zebrafish according to a scale ranking oedema and spinal curvature from 0 (normal) to 3 (severe) (Control MO = 0(0, 0), *slc52a3* MO = 1(0, 2), riboflavin/probenecid co-treated *slc52a3* MO = 1(0, 2); Kruskal-Wallis test with Dunn's multiple comparisons test). Control MO *n* = 28 *slc52a3* MO *n* = 21 riboflavin/probenecid co-treated *slc52a3* MO *n* = 11. ns = not significant, * = $p < 0.05$, ** = $p < 0.01$, *** = $p < 0.001$, **** = $p < 0.0001$.

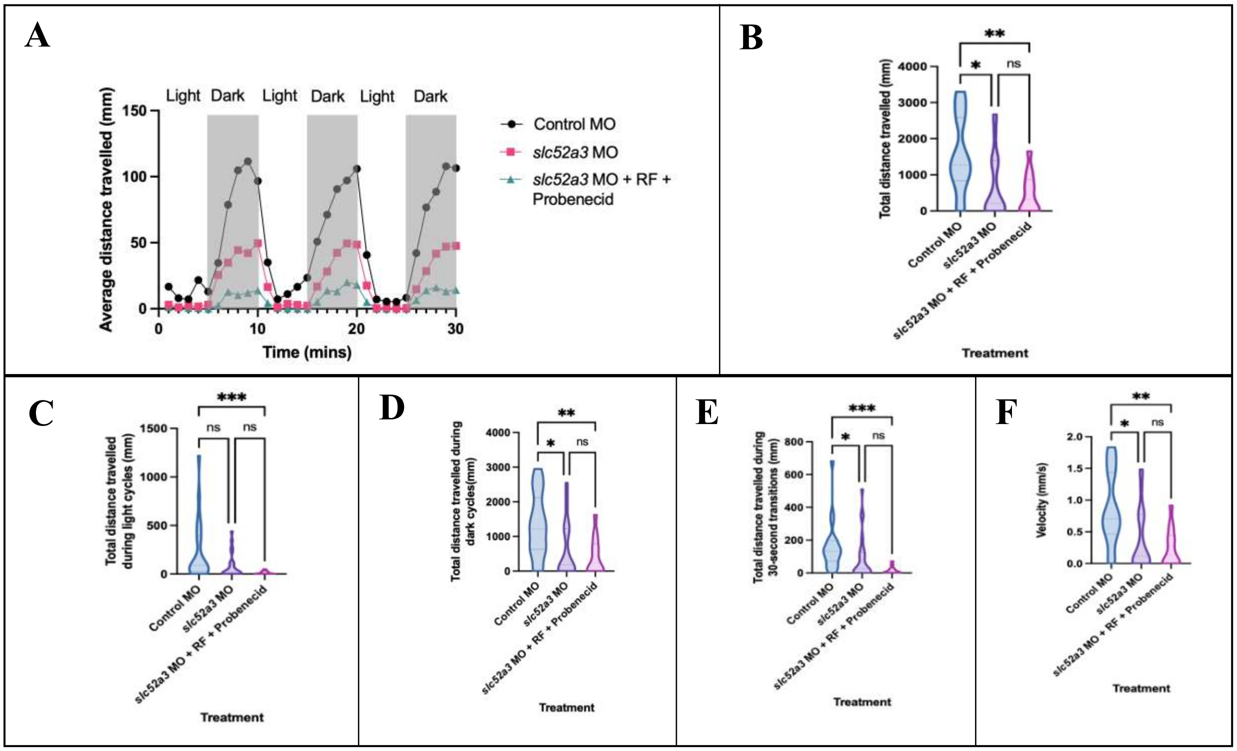

Figure 3.31 Voluntary locomotor activity performed by riboflavin/probenecid co-treated *slc52a3* MO embryos during light-dark activity test at 5 dpf (A) Average distance travelled (mm) by *slc52a3* MO and riboflavin/probenecid co-treated *slc52a3* MO embryos per minute during light-dark activity test (Control MO = 0.6(0.1, 1.5), *slc52a3* MO = 0.183(0, 0.654), riboflavin/probenecid co-treated *slc52a3* MO = 0(0,0); Kruskal-Wallis test with Dunn's multiple comparisons test). Control MO *n* = 22 *slc52a3* MO *n* = 24 riboflavin/probenecid co-treated *slc52a3* MO *n* = 12. (B) Total distance travelled (mm) by *slc52a3* MO and riboflavin/probenecid co-treated *slc52a3* MO embryos during light-dark activity test (Control MO = 1273(836, 2590), *slc52a3* MO = 213.9(0, 1390), riboflavin/probenecid co-treated *slc52a3* MO = 313.4(0, 863.6); Kruskal-Wallis test with Dunn's multiple comparisons test). Control MO *n* = 22 *slc52a3* MO *n* = 24 riboflavin/probenecid co-treated *slc52a3* MO *n* = 12. (C) Total distance travelled (mm) by *slc52a3* MO and riboflavin/probenecid co-treated *slc52a3* MO embryos during light cycles in light-dark activity test (Control MO = 89.3(25.3, 396), *slc52a3* MO = 20.2(0, 107.3), riboflavin/probenecid co-treated *slc52a3* MO = 6(0, 24); Kruskal-Wallis test with Dunn's multiple comparisons test). Control MO *n* = 22 *slc52a3* MO *n* = 24 riboflavin/probenecid co-treated *slc52a3* MO *n* = 13. (D) Total distance travelled (mm) by *slc52a3* MO and riboflavin/probenecid co-treated *slc52a3* MO embryos during dark cycles in light-dark activity test (Control MO = 1212(630.6, 2126), *slc52a3* MO = 184.5(0, 1229), riboflavin/probenecid co-treated *slc52a3* MO = 236(0, 784.5); Kruskal-Wallis test with Dunn's multiple comparisons test). Control MO *n* = 22 *slc52a3* MO *n* = 24 riboflavin/probenecid co-treated *slc52a3* MO *n* = 13. (E) Total distance travelled (mm) by *slc52a3* MO and riboflavin/probenecid co-treated *slc52a3* MO embryos during 30-second transitions between cycles in light-dark activity test (Control MO = 131.6(72.33, 198.4), *slc52a3* MO = 24.3(0, 126.4), riboflavin/probenecid co-treated *slc52a3* MO = 8.1(0, 25.2); Kruskal-Wallis test with Dunn's multiple comparisons test). Control MO *n* = 22 *slc52a3* MO *n* = 24 riboflavin/probenecid co-treated *slc52a3* MO *n* = 13. (E) Average velocity travelled (mm/s) by *slc52a3* MO and

riboflavin/probenecid co-treated *slc52a3* MO embryos during light-dark activity test (Control MO = 0.707(0.465, 1.439), *slc52a3* MO = 0.119(0, 0.772), riboflavin/probenecid co-treated *slc52a3* MO = 0.141(0, 0.443); Kruskal-Wallis test with Dunn's multiple comparisons test). Control MO *n* = 22 *slc52a3* MO *n* = 24 riboflavin/probenecid co-treated *slc52a3* MO *n* = 13. ns = not significant; * = p < 0.05, ** = p < 0.01, *** = p < 0.001, **** = p < 0.0001.

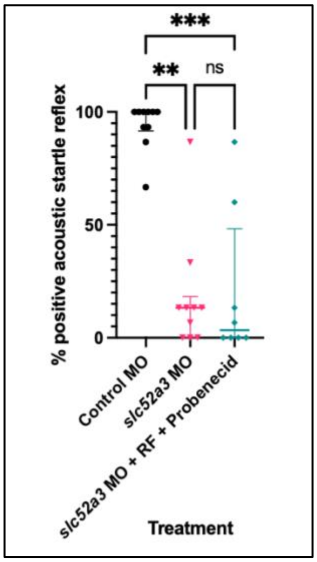

Figure 3.32 % positive acoustic startle reflex exhibited by *slc52a3* and riboflavin/probenecid co-treated *slc52a3* MO zebrafish between 5-7 dpf (Control MO = 100 (91.67, 100), *slc52a3* MO = 13.33 (0, 18.33), riboflavin and probenecid co-treated *slc52a3* MO = 3.333(0, 48.33); Kruskal-Wallis test with Dunn's multiple comparisons test). Control MO *n* = 10 *slc52a3* MO *n* = 10 riboflavin and probenecid co-treated *slc52a3* MO *n* = 8. ns = not significant; ** = p < 0.01; *** = p < 0.001.

4. Discussion

4.1 Protein analysis reveals potential functional similarity between SLC52A2/slc52a2, SLC52A3/slc52a3, and SLC22A8/slc22a6l

Protein sequence alignment of SLC52A2/slc52a2 and SLC52A3/slc52a3 revealed a sequence identity of >50% in both cases. According to a previous report, homologous proteins that share a sequence identity of 50% or greater show a reduced proportion of divergent functions, indicating that there may be an overlap between the human RTD phenotype and the zebrafish *slc52a2*/*slc52a3* knockdown phenotype, and therefore lending support to the use of zebrafish as a model organism for RTD[95]. While *slc52a2* knockdown zebrafish did not exhibit an RTD-like phenotype, the implications of the SLC52A3/slc52a3 protein sequence alignment are reinforced by the phenotype resulting from *slc52a3* knockdown, which includes several RTD characteristics that are highly similar to the human RTD phenotype. The successful rescue of the *slc52a3* knockdown phenotype using *SLC52A3* mRNA further shows evidence of shared functionality between SLC52A3 and slc52a3.

SLC22A8/slc22a6l share a protein sequence identity of 49.54%, which falls slightly below the 50% threshold, suggesting that human OAT-3 and zebrafish oat-3 may share some functional similarity. This was further supported by the ColabFold and SwissDock findings. The protein structures predicted for SLC22A8 and slc22a6l by ColabFold were generated with pLDDT scores above 80, indicating high confidence that these predicted structures would closely align with experimentally confirmed structures[80]. Superimposition of SLC22A8 and slc22a6l resulted in a rmsd score of 0.520 Å, which represents good structural similarity between both models[82–85]. The SLC22A8/slc22a6l rmsd scores and similarity in SwissDock-generated docking predictions suggest that riboflavin and probenecid may interact similarly with human OAT-3 and zebrafish oat-3.

4.2 *slc52a3* and *slc52a2/slc52a3* combined knockdown phenotypes successfully recapitulate the human RTD phenotype

Several key morphological and behavioural aspects of the human RTD phenotype are successfully recapitulated in *slc52a3* and *slc52a2/slc52a3* combined morphants. Spontaneous movements, the earliest characteristic observed in this study, are increased in *slc52a3* and *slc52a2/slc52a3* combined morphants at 24 hpf. The period of spontaneous movements in early zebrafish development overlaps with the axonal outgrowth process, with movements starting at 17 hpf and becoming more frequent until 27 hpf[47,75]. Increased spontaneous movements at 24 hpf compared to control morphants may be indicative of a delay in the axonal outgrowth process which may be causing the spontaneous movement period to begin and end at later timepoints than those typically observed during normal neurodevelopment. The neurodegenerative nature of human RTD, demonstrated in these *slc52a3* morphants via their shortened motor axons, could be reflected in this finding, as neurodegeneration may potentially disrupt the axon outgrowth process and lead to abnormal frequencies of spontaneous movements in *slc52a3* and *slc52a2/slc52a3* combined morphants. Colocalization of the presynaptic and postsynaptic regions of NMJs was significantly decreased in *slc52a3* morphants compared to control morphants, indicating potentially abnormal NMJ morphology which may be a result of abnormal axonal outgrowth due to RTD-associated neurodegeneration[96]. Reduced colocalization of presynaptic and postsynaptic regions of the NMJ has been previously observed in *smn* mutant zebrafish lines with a spinal muscular atrophy-like phenotype – a disease causing neurodegeneration of motor neurons in the anterior horn of the spinal cord, similar to RTD which is also characterised by motor neuron degeneration in the spinal cord and can involve anterior horn cells[6,25,96]. Measurement of voluntary locomotor activity at 5 dpf in response to alternating light and dark cycles revealed that *slc52a3* and *slc52a2/slc52a3* morphants travel a shorter distance at a slower velocity during the 30-minute test. These locomotor impairments are possibly attributed to muscle weakness in the knockdown fish as a result of neurodegeneration and subsequent muscle atrophy, which is observed in human RTD[6].

Sensorineural hearing loss is another aspect of the human phenotype that is reflected in the *slc52a3* and *slc52a2/slc52a3* morphant models. The otic vesicle area in both morphant models was found to be reduced compared to control morphants, which has previously been observed in a zebrafish morphant model of nonsyndromic X-linked sensorineural deafness also exhibiting sensory hair cell loss and impaired otic vesicle-mediated responses to vibrational stimuli[50]. The zebrafish otic vesicle houses the sensory hair cells responsible for transducing mechanical vibrations evoked by sound into electrical impulses, and these hair cells are similarly found in the mammalian inner ear[97–100]. The sensorineural hearing loss observed in RTD patients results from degeneration of nuclei in cranial nerve VIII, which functions similarly to cranial nerve VIII in zebrafish to innervate the hair cells of the inner ear and transmit sound-evoked electrical impulses to the brain[6,101–104]. This neurodegeneration combined with the potential loss of sensory hair cells may be contributing to the decrease in otic vesicle area observed in the *slc52a3* and *slc52a2/slc52a3* morphants[6,50]. Similar to the aforementioned model of nonsyndromic X-linked sensorineural deafness which demonstrated impaired response to vibrational stimuli, *slc52a3* and *slc52a2/slc52a3* morphants exhibited a reduction in percent positive acoustic startle reflex compared to control morphants[38]. Degeneration of cranial nerve VIII and loss of sensory hair cells may be responsible for this reduced response rate by impairing induction of sound-evoked vibrations and subsequent impulse transmission to the brain[6,50]. To further examine the impact of *slc52a3* and *slc52a2/slc52a3* gene knockdown on otic vesicle morphology and hearing, phalloidin immunostaining of the stereocilia as performed by Koleilat et al. (2020) will allow for analysis of stereocilia organization within the otic vesicle[105].

Multiple additional morphological characteristics of this zebrafish RTD model are also reflective of human RTD characteristics, including decreased eye area, decreased body length and increased spinal curvature. Decreased eye area observed in *slc52a3* and *slc52a2/slc52a3* morphants may be attributed to optic atrophy, which is a feature of the human RTD phenotype[26]. A zebrafish model of mitochondrial membrane protein associated neurodegeneration – another genetic disorder associated with optic atrophy – has also demonstrated reduced eye area[54]. Further experiments to better determine whether optic atrophy is affecting *slc52a3* and *slc52a2/slc52a3* morphants could include retinal ganglion cell axon immunostaining as previously performed by Abrams et al. (2015) to determine any differences in their innervation of the optic tectum, the main structure responsible for receiving signals from retinal ganglion cells in fish[53,106]. Decreased body length could be a result of muscle atrophy, which is a key characteristic of RTD in human patients. Both decreased body length and increased spinal curvature have both been observed in a previous zebrafish model of Parkinson's disease, a neurodegenerative disease characterised by neurodegeneration of dopaminergic neurons in the midbrain of the brainstem[107–110]. Neurodegeneration in RTD patients has also been reported to occur in the midbrain of the brainstem, and this similarity in disease pathogenesis may be responsible for the morphological overlap between these models[6].

4.3 *slc52a3* knockdown phenotype is independent of p53 apoptotic pathway activation and is successfully rescued by *SLC52A3* mRNA co-injection

To address the potential for off-target effects that may confound the *slc52a3* morphant phenotype, we confirmed that this phenotype was independent of neural death resulting from p53 apoptotic pathway activation via coinjection of embryos with *slc52a3* morpholino and *p53* morpholino[67,111,112]. Co-injected embryos demonstrated the same differences from control morphants as observed in *slc52a3* knockdown embryos regarding the morphological and behavioural characteristics measured, increasing our confidence in the specificity of the *slc52a3* morphant phenotype[112]. Additionally, to confirm that the *slc52a3* morphant phenotype is not arising as a result of off-target alterations in expression of other genes in the zebrafish genome, we co-injected embryos with full-length human *SLC52A3* mRNA and *slc52a3* morpholino, allowing for a complete rescue of the morphological and behavioural *slc52a3* morphant characteristics that we tested[111–113]. This lends further support for the specificity of our *slc52a3* knockdown phenotype, and also points towards the potentially conserved function of zebrafish *slc52a3*-encoded protein and human RFVT3, which highlights the potential applicability of this study's findings to RTD patients[114,115]. Immunofluorescent staining of motor axons in *slc52a3* MO/*SLC52A3* mRNA co-injected embryos will help to establish whether the RTD-like neuronopathy phenotype is also successfully rescued and therefore specific to *slc52a3* knockdown.

4.4 *slc52a2*- and *slc52a3*-targeted F0 crispants exhibit partial phenotypic overlap with *slc52a2* and *slc52a3* morpholino-mediated knockdowns

F0 crispants did not fully replicate the *slc52a2* and *slc52a3* knockdown phenotypes, however, there were some similarities between the crispant and morphant models. While *slc52a2* morphants did not show any differences from control morphants in any behavioural or morphological assay performed, *slc52a2*-targeted crispants demonstrated a reduction in frequency of spontaneous movements compared to *tyr*-targeted controls. However, *slc52a2*-targeted crispants did reflect the *slc52a2* morphant model with respect to body length, which did not differ between *slc52a2* crispants and *tyr*-targeted controls. The *slc52a3*-targeted crispants, on the other hand, were more similar to the *slc52a3* morphant model, with both models exhibiting increased frequency of spontaneous movements and decreased body length in comparison to their respective controls. No other phenotypic differences between *tyr*-targeted controls and *slc52a2*- or *slc52a3*-targeted crispants were observed. The milder crispant phenotype and differences identified between the crispant and morphant *slc52a2*- and *slc52a3*-targeted zebrafish may be attributed to several reasons. Due to the rescue of the *slc52a3* morphant phenotype following *SLC52A3* mRNA co-injection, it is unlikely that the crispant and morphant phenotypic divergence is due to off-target effects of the morpholino[116]. A potential cause of this variation is genetic compensation, whereby off-target genes modulate their expression in response to CRISPR/Cas9-mediated editing[114–116]. This phenomenon has been shown to result in mutant lines with milder phenotypes than their corresponding morpholino-mediated knockdown zebrafish models[114–116]. Although genetic compensation mechanisms have previously been reported in stable mutant lines rather than F0 crispants, potential triggers for genetic compensation include the production of a mutant transcript and DNA lesion, both of which are expected to occur in F0 individuals following sgRNA/Cas9 microinjection[119,120]. Therefore, it is possible that genetic compensation is affecting the phenotype observed in *slc52a2*- and *slc52a3*-targeted F0 zebrafish.

Further characterisation of *slc52a2*- and *slc52a3*-targeted crispants will provide a more comprehensive view of the similarities and differences between the morphant and crispant phenotypes. Additionally, continuing to work towards the development of stable CRISPR/Cas9 *slc52a2* and *slc52a3* knockout lines will allow for comparison between morphant phenotypes and F1 and F2 phenotypes. Development of these stable mutant lines will also enable identification of potential genetic compensation mechanisms that may be occurring in F0, F1, and F2 individuals, and will present opportunities for therapeutic screening of candidate drugs on more zebrafish models of RTD to better determine the potential for amelioration of the disease phenotype.

4.5 Riboflavin and/or probenecid supplementation provides minimal benefit to *slc52a3* knockdown zebrafish

Riboflavin-treated *slc52a3* knockdown zebrafish demonstrated non-significant increases in body length and otic vesicle area, as well as a non-significant decrease in spinal curvature. Riboflavin-treated *slc52a3* knockdowns also exhibited some improvements in locomotor ability including a significant increase in average distance travelled and non-significant increases in total distance travelled, total distance travelled during light cycles, and average velocity during the light-dark activity test. Over 70% of RTD patients have improved in response to riboflavin supplementation, with these patients showing amelioration of symptoms including muscle weakness, respiratory function, hearing, and vision[25,121]. However, this treatment is rapidly excreted from the body above doses of 30 mg and plasma concentrations of 0.5 µM, meaning some patients do not improve and either stabilize or continue to deteriorate during treatment[3,6,17,24,33]. Although riboflavin-treated *slc52a3* knockdown fish show less amelioration of the RTD-like phenotype than RTD patients, these findings do reflect the fact that riboflavin treatment is not always effective and justifies the addition of probenecid to assess its potential inhibitory effect on riboflavin excretion. To better determine the extent of the benefit exerted by riboflavin on *slc52a3* morphants, therapeutic screening of riboflavin must be conducted on a larger sample size of fish. It is possible that rather than treating the fish every 24 hours, *slc52a3* morphants require more frequent treatments in order to display a more pronounced benefit on the disease phenotype, as riboflavin has a short half-life of 1.1 hours[122].

Despite the high degree of similarity between human OAT-3 and zebrafish oat-3 predicted structures as well as riboflavin and probenecid docking positions on these predicted structures, phenotypic analysis of probenecid- and riboflavin/probenecid co-treated zebrafish embryos was not indicative of a similarity in function between human OAT-3 and zebrafish oat-3. However, this cannot be properly confirmed without further therapeutic screening of probenecid using more dosages and a larger sample size of fish to better elucidate the probenecid/zebrafish oat-3 interaction. Phenotypic characterisation of *slc22a6l* and *slc52a3* co-knockdowns could be an additional method of determining whether oat-3 plays a role in riboflavin excretion in zebrafish. These additional experiments are needed to determine whether the findings obtained from therapeutic screening of probenecid in *slc52a3* morphants may be indicative of how probenecid will affect the human RTD phenotype.

A potential reason for the minimal impact of riboflavin and probenecid treatment on *slc52a3* morphants is the chosen mode of drug delivery. In this study, candidate drugs were added to the well plates housing the zebrafish embryos, which is the same method employed in previous riboflavin and probenecid screening studies in zebrafish[123–125]. However, intravenous injection of probenecid has been performed in zebrafish and may be a worthwhile alternative to our current method of riboflavin and probenecid delivery, potentially helping to exert a greater benefit on the *slc52a3* morphant phenotype[126].

According to the *slc22a6l* expression profile from 1-5 dpf, *slc22a6l* expression begins to increase from 3 dpf to 5 dpf, corresponding to maturation of the blood-brain barrier which occurs from 3 dpf to 10 dpf[127]. This means that inhibition of oat-3 via probenecid treatment may not effectively prevent riboflavin elimination from CSF until 3 dpf, at which point the RTD-associated neurodegeneration may have already caused irreversible damage to the CNS in zebrafish with an RTD-like phenotype. This is another potential reason why riboflavin/probenecid co-treated *slc52a3* morphant embryos did not exhibit an amelioration in phenotype. If this is the case, an alternative therapeutic must be considered that can participate in its mechanistic pathway at an earlier timepoint in zebrafish development to help minimize the effect of *slc52a3* knockdown on the zebrafish phenotype. Probenecid is also a non-specific inhibitor with reported inhibitory effects on not only OAT-3, but also organic anion transporter-1 (OAT-1) and pannexin-1 (PANX-1), all of which have zebrafish orthologs[60,61,128]. Probenecid could possibly be exerting off-target inhibitory effects on these proteins, which combined with the existing *slc52a3* morphant phenotype, may be preventing additional riboflavin retention or worsening the RTD-like phenotype. If further dose-response experiments and changes in mode of delivery do not yield promising results, perhaps an alternative drug with a more specific mechanism of action should be considered for therapeutic screening in these models.

Mass spectrometry analysis, which has been widely used to analyse a range of metabolites in zebrafish at various timepoints, would be a useful tool enabling the measurement of riboflavin, FAD, and FMN levels in *slc52a3* and *slc52a2/slc52a3* knockdown embryos and CRISPR/Cas9-mediated mutants[129]. Furthermore, as GSH is dependent on riboflavin for its reduction from GSSG to GSH, GSH levels are correlated with flavin levels and can also be measured by mass spectrometry, allowing us to examine the impact of the disease phenotype on free-radical scavenging and protection against oxidative stress[1,8,10]. Analysis of these targets will help to determine if flavin homeostasis is affected in the zebrafish RTD-like phenotype as observed in RTD patients, and could also enable us to assess the impact of candidate drugs on flavin content and redox status across our RTD models[1,8,24].

4.6 Conclusion

This study represents the first attempt to model RTD in zebrafish, which is a promising next step in RTD research following previously reported embryonic lethality and neonatal lethality associated with constitutive knockout of RTD disease gene orthologues *Slc52a2* and *Slc52a3* in mice. Due to the shortcomings of riboflavin supplementation as a treatment for RTD, modelling of this disease in zebrafish presents a promising avenue for the discovery of novel therapeutic combinations allowing for increased riboflavin retention and ameliorated disease phenotype. RTD-like phenotypes have been observed in *slc52a3* and *slc52a2/slc52a3* combined knockdown zebrafish, characterised by altered spontaneous chorion movements, decreased motor axon length, increased spinal curvature, shortened body length, decreased eye area and otic vesicle area, altered locomotor ability, and impaired acoustic startle reflex. This RTD-like phenotype was found to be specific and independent of p53 activation, as well as rescuable upon co-injection of *slc52a3* MO/*SLC52A3* mRNA, providing strong support for the applicability of this study's findings to RTD patients. CRISPR/Cas9-mediated *slc52a2*- and *slc52a3*-targeted crispants demonstrated partial phenotypic overlap with their respective morphant models, and further characterisation and development of these stable knockout lines will allow for more therapeutic screening opportunities over a longer time-period.

Strengths of *slc52a3* MO model	**Weaknesses of *slc52a3* MO model**
Recapitulate phenotypic characteristics of RTD	RTD-like phenotype is transient and cannot be observed long-term
Reproducible RTD-like phenotype	RTD-like phenotype does not phenocopy *slc52a2* and *slc52a3* F0 crispant phenotype
RTD-like phenotype is independent of p53 activation and rescuable upon *slc52a3* MO/*SLC52A3* mRNA coinjection	There is the potential for unidentified off-target effects induced by MO injection to be confounding the RTD-like phenotype

Table 4-1 Strengths and weaknesses of *slc52a3* MO RTD model.

Upon treatment with riboflavin, the *slc52a3* morphant phenotype demonstrated minimal improvement, corroborating clinical outcomes observed in RTD patients and prompting the addition of probenecid treatment, which exerted even less benefit on the morphant phenotype individually, and did not improve the phenotype in combination with riboflavin. Further optimization of the therapeutic screening process as well as consideration of alternative therapeutics for the treatment of the RTD-like phenotype will help to further efforts to enhance the disease course for RTD patients in the future.

4.7 Statement on contributions of collaborators

I would like to recognize the valuable contributions to this project by several members of the Lochmüller lab. Thank you to Dr. Emily O' Connor (lab alumna), who collected RNA from 1-5 day-old zebrafish and synthesized cDNA samples for RT-PCR. Dr. O' Connor also designed primers for *slc52a2* and *slc52a3* RT-PCR detection and performed zebrafish microinjections of sgRNA/Cas9 complexes used for F0 *tyr*, *slc52a2* and *slc52a3* characterization. I would also like to thank Jarred Lau for his help performing *slc52a3* MO microinjections and dose-response testing of *slc52a3* MO + *SLC52A3* mRNA co-injections. Finally, I would like to extend my gratitude to Dr. Romane Idoux for generating *slc52a3* MO knockdown zebrafish used for riboflavin and probenecid combined treatment.

5. References

1. Suwannasom, N., Kao, I., Pruß, A., Georgieva, R. & Bäumler, H. Riboflavin: The Health Benefits of a Forgotten Natural Vitamin. *Int. J. Mol. Sci.* **21**, 950 (2020).
2. Balasubramaniam, S., Christodoulou, J. & Rahman, S. Disorders of riboflavin metabolism. *J. Inherit. Metab. Dis.* **42**, 608–619 (2019).
3. Powers, H. J. Riboflavin (vitamin B-2) and health. *Am. J. Clin. Nutr.* **77**, 1352–60 (2003).
4. Mosegaard, S. *et al.* Riboflavin deficiency—implications for general human health and inborn errors of metabolism. *Int. J. Mol. Sci.* **21**, (2020).
5. Jarrett, H. *et al.* Vitamin B-6 and riboflavin, their metabolic interaction, and relationship with MTHFR genotype in adults aged 18–102 years. *Am. J. Clin. Nutr.* **116**, 1767–1778 (2022).
6. O'Callaghan, B., Bosch, A. M. & Houlden, H. An update on the genetics, clinical presentation, and pathomechanisms of human riboflavin transporter deficiency. *J. Inherit. Metab. Dis.* **42**, 598–607 (2019).
7. Ashoori, M. & Saedisomeolia, A. Riboflavin (vitamin B $_2$) and oxidative stress: a review. *Br. J. Nutr.* **111**, 1985–1991 (2014).
8. ZITKA, O. *et al.* Redox status expressed as GSH:GSSG ratio as a marker for oxidative stress in paediatric tumour patients. *Oncol. Lett.* **4**, 1247–1253 (2012).
9. Mulherin, D. M., Thurnham, D. I. & Situnayake, R. D. Glutathione reductase activity, riboflavin status, and disease activity in rheumatoid arthritis. *Ann. Rheum. Dis.* **55**, 837–840 (1996).
10. Massarsky, A., Kozal, J. S. & Di Giulio, R. T. Glutathione and zebrafish: Old assays to address a current issue. *Chemosphere* **168**, 707–715 (2017).

11. Knovich, M. A., Storey, J. A., Coffman, L. G. & Torti, S. V. Ferritin for the Clinician. *Blood Rev.* **23**, 95–104 (2009).

12. Shi, Z. *et al.* Inadequate Riboflavin Intake and Anemia Risk in a Chinese Population: Five-Year Follow Up of the Jiangsu Nutrition Study. *PLOS ONE* **9**, e88862 (2014).

13. Colasuonno, F. *et al.* New Insights into the Neurodegeneration Mechanisms Underlying Riboflavin Transporter Deficiency (RTD): Involvement of Energy Dysmetabolism and Cytoskeletal Derangement. *Biomedicines* **10**, 1329 (2022).

14. Udhayabanu, T., Gandhimathi, K., Varalakshmi, P. & Ashokkumar, B. Functional Genomics of Riboflavin Transport. in *Current Developments in Biotechnology and Bioengineering* 79–102 (Elsevier, 2017). doi:10.1016/B978-0-444-63667-6.00004-3.

15. Kaur, C., Rathnasamy, G. & Ling, E.-A. The Choroid Plexus in Healthy and Diseased Brain. *J. Neuropathol. Exp. Neurol.* **75**, 198–213 (2016).

16. Kadry, H., Noorani, B. & Cucullo, L. A blood–brain barrier overview on structure, function, impairment, and biomarkers of integrity. *Fluids Barriers CNS* **17**, 69 (2020).

17. Spector, R. Vitamin Transport Diseases of Brain: Focus on Folates, Thiamine and Riboflavin. *Brain Disord. Ther.* **03**, (2014).

18. Srimaroeng, C., Cecile, J. P., Walden, R. & Pritchard, J. B. Regulation of Renal Organic Anion Transporter 3 (SLC22A8) Expression and Function by the Integrity of Lipid Raft Domains and their Associated Cytoskeleton. *Cell. Physiol. Biochem.* **31**, 565–578 (2013).

19. Zhang, J., Wang, H., Fan, Y., Yu, Z. & You, G. Regulation of organic anion transporters: role in physiology, pathophysiology, and drug elimination. *Pharmacol. Ther.* **217**, 107647 (2021).

20. Spector, R. Riboflavin Homeostasis in the Central Nervous System. *J. Neurochem.* **35**, 202–209 (1980).

21. Pillai, N. R. *et al.* Hematologic presentation and the role of untargeted metabolomics analysis in monitoring treatment for riboflavin transporter deficiency. *Am. J. Med. Genet. A.* **182**, 2781–2787 (2020).
22. Subramanian, V. S., Kapadia, R., Ghosal, A. & Said, H. M. Identification of residues/sequences in the human riboflavin transporter-2 that is important for function and cell biology. *Nutr. Metab.* **12**, 13 (2015).
23. Subramanian, V. S., Sabui, S., Teafatiller, T., Bohl, J. A. & Said, H. M. Structure/functional aspects of the human riboflavin transporter-3 (SLC52A3): role of the predicted glycosylation and substrate-interacting sites. *Am. J. Physiol. - Cell Physiol.* **313**, 228–238 (2017).
24. Frederick, A. L. *et al.* To Be or No B2: A Rare Cause of Stridor and Weakness in a Toddler. *Child Neurol. Open* **8**, 2329048X2110307 (2021).
25. Spagnoli, C., Pitt, M. C., Rahman, S. & De Sousa, C. Brown-Vialetto-van Laere syndrome: A riboflavin responsive neuronopathy of infancy with singular features. *Eur. J. Paediatr. Neurol.* **18**, 231–234 (2014).
26. Amir, F. *et al.* The Clinical Journey of Patients with Riboflavin Transporter Deficiency Type 2. *J. Child Neurol.* **35**, 283–290 (2020).
27. Carreau, C. *et al.* Late-onset riboflavin transporter deficiency: A treatable mimic of various motor neuropathy aetiologies. *J. Neurol. Neurosurg. Psychiatry* **92**, 27–35 (2021).
28. Colasuonno, F., Bertini, E., Tartaglia, M., Compagnucci, C. & Moreno, S. Mitochondrial abnormalities in induced pluripotent stem cells-derived motor neurons from patients with riboflavin transporter deficiency. *Antioxidants* **9**, 1–10 (2020).

29. Niceforo, A. *et al.* Altered cytoskeletal arrangement in induced pluripotent stem cells (iPSCs) and motor neurons from patients with riboflavin transporter deficiency. *Dis. Model. Mech.* dmm.046391 (2021) doi:10.1242/dmm.046391.

30. Rizzo, F. *et al.* Genome-wide RNA-seq of iPSC-derived motor neurons indicates selective cytoskeletal perturbation in Brown–Vialetto disease that is partially rescued by riboflavin. *Sci. Rep.* **7**, 46271 (2017).

31. Colasuonno, F. *et al.* Mitochondrial and Peroxisomal Alterations Contribute to Energy Dysmetabolism in Riboflavin Transporter Deficiency. *Oxid. Med. Cell. Longev.* **2020**, (2020).

32. Ayala, A., Muñoz, M. F. & Argüelles, S. Lipid Peroxidation: Production, Metabolism, and Signaling Mechanisms of Malondialdehyde and 4-Hydroxy-2-Nonenal. *Oxid. Med. Cell. Longev.* **2014**, 360438 (2014).

33. Koy, A. *et al.* Brown-Vialetto-Van Laere syndrome: A riboflavin-unresponsive patient with a novel mutation in the C20orf54 gene. *Pediatr. Neurol.* **46**, 407–409 (2012).

34. Woodcock, I. R. *et al.* Genetic, Radiologic, and Clinical Variability in Brown-Vialetto-van Laere Syndrome. *Semin. Pediatr. Neurol.* **26**, 2–9 (2018).

35. Marioli, C. *et al.* Antioxidant Amelioration of Riboflavin Transporter Deficiency in Motoneurons Derived from Patient-Specific Induced Pluripotent Stem Cells. *Int. J. Mol. Sci.* **21**, 7402 (2020).

36. Yoshimatsu, H. *et al.* Disruption of Slc52a3 gene causes neonatal lethality with riboflavin deficiency in mice. *Sci. Rep.* **6**, 27557 (2016).

37. Jin, C. *et al.* Complete Deletion of *Slc52a2* Causes Embryonic Lethality in Mice. *Biol. Pharm. Bull.* **44**, 283–286 (2021).

38. Tolomeo, M., Nisco, A., Leone, P. & Barile, M. Development of Novel Experimental Models to Study Flavoproteome Alterations in Human Neuromuscular Diseases: The Effect of Rf Therapy. *Int. J. Mol. Sci.* **21**, 5310 (2020).

39. Manole, A. *et al.* Clinical, pathological and functional characterization of riboflavin-responsive neuropathy. *Brain* **140**, 2820–2837 (2017).

40. Haynes, E. M., Ulland, T. K. & Eliceiri, K. W. A Model of Discovery: The Role of Imaging Established and Emerging Non-mammalian Models in Neuroscience. *Front. Mol. Neurosci.* **15**, (2022).

41. Giacomotto, J. & Ségalat, L. High-throughput screening and small animal models, where are we? *Br. J. Pharmacol.* **160**, 204–216 (2010).

42. Naert, T. & Vleminckx, K. CRISPR/Cas9 disease models in zebrafish and Xenopus: The genetic renaissance of fish and frogs. *Drug Discov. Today Technol.* **28**, 41–52 (2018).

43. Letamendia, A. *et al.* Development and Validation of an Automated High-Throughput System for Zebrafish In Vivo Screenings. *PLOS ONE* **7**, e36690 (2012).

44. Timme-Laragy, A. R., Karchner, S. I. & Hahn, M. E. Gene knockdown by morpholino-modified oligonucleotides in the zebrafish (danio rerio) model: Applications for developmental toxicology. *Methods Mol. Biol.* **889**, 51–71 (2012).

45. Sidik, H., Ang, C. J. & Pouladi, M. A. Huntingtin confers fitness but is not embryonically essential in zebrafish development. *Dev. Biol.* **458**, 98–105 (2020).

46. Bose, P. *et al.* The Novel Small Molecule TRVA242 Stabilizes Neuromuscular Junction Defects in Multiple Animal Models of Amyotrophic Lateral Sclerosis. *Neurotherapeutics* **16**, 1149–1166 (2019).

47. O'Connor, E. *et al.* Modulation of Agrin and RhoA Pathways Ameliorates Movement Defects and Synapse Morphology in MYO9A-Depleted Zebrafish. *Cells* **8**, (2019).

48. Pellerin, D. *et al.* Novel Recessive TNNT1 Congenital Core-Rod Myopathy in French Canadians. *Ann. Neurol.* **87**, 568–583 (2020).

49. Babin, P. J., Goizet, C. & Raldúa, D. Zebrafish models of human motor neuron diseases: Advantages and limitations. *Prog. Neurobiol.* **118**, 36–58 (2014).

50. DeSmidt, A. A. *et al.* Zebrafish Model for Nonsyndromic X-Linked Sensorineural Deafness, DFNX1. *Anat. Rec.* **303**, 544–555 (2020).

51. Chen, Z. *et al.* Tmc proteins are essential for zebrafish hearing where Tmc1 is not obligatory. *Hum. Mol. Genet.* **29**, 2004–2021 (2020).

52. Sztal, T. E. *et al.* Zebrafish models for nemaline myopathy reveal a spectrum of nemaline bodies contributing to reduced muscle function. *Acta Neuropathol. (Berl.)* **130**, 389–406 (2015).

53. Abrams, A. J. *et al.* Mutations in SLC25A46, encoding a UGO1-like protein, cause an optic atrophy spectrum disorder. *Nat. Genet.* **47**, 926–932 (2015).

54. Mignani, L., Zizioli, D., Borsani, G., Monti, E. & Finazzi, D. The Downregulation of c19orf12 Negatively Affects Neuronal and Musculature Development in Zebrafish Embryos. *Front. Cell Dev. Biol.* **8**, (2020).

55. Elmonem, M. *et al.* Genetic Renal Diseases: The Emerging Role of Zebrafish Models. *Cells* **7**, 130 (2018).

56. Jd, M. Guide for Morpholino Users: Toward Therapeutics. 13.

57. Li, J. & Ge, W. Zebrafish as a model for studying ovarian development: Recent advances from targeted gene knockout studies. *Mol. Cell. Endocrinol.* **507**, 110778 (2020).

58. Cunningham, R. F., Israili, Z. H. & Dayton, P. G. Clinical pharmacokinetics of probenecid. *Clin. Pharmacokinet.* **6**, 135–151 (1981).

59. Ragab, G., Elshahaly, M. & Bardin, T. Gout: An old disease in new perspective – A review. *J. Adv. Res.* **8**, 495–511 (2017).

60. Silverman, W., Locovei, S. & Dahl, G. Probenecid, a gout remedy, inhibits pannexin 1 channels. *Am. J. Physiol. - Cell Physiol.* **295**, C761–C767 (2008).

61. Perwitasari, O. *et al.* Targeting Organic Anion Transporter 3 with Probenecid as a Novel Anti-Influenza A Virus Strategy. *Antimicrob. Agents Chemother.* **57**, 475–483 (2013).

62. Christensen, S. Renal Excretion of Riboflavin in the Rat. *Acta Pharmacol. Toxicol. (Copenh.)* **29**, 428–440 (2009).

63. Sievers, F. *et al.* Fast, scalable generation of high-quality protein multiple sequence alignments using Clustal Omega. *Mol. Syst. Biol.* **7**, 539 (2011).

64. Waterhouse, A. M., Procter, J. B., Martin, D. M. A., Clamp, M. & Barton, G. J. Jalview Version 2—a multiple sequence alignment editor and analysis workbench. *Bioinformatics* **25**, 1189–1191 (2009).

65. Kos, R., Tucker, R. P., Hall, R., Duong, T. D. & Erickson, C. A. Methods for introducing morpholinos into the chicken embryo. *Dev. Dyn.* **226**, 470–477 (2003).

66. Dever, D. P. *et al.* CRISPR/Cas9 β-globin gene targeting in human haematopoietic stem cells. *Nature* **539**, 384–389 (2016).

67. Robu, M. E. *et al.* p53 Activation by Knockdown Technologies. *PLoS Genet.* **3**, e78 (2007).

68. Hu, Y., Xie, S. & Yao, J. Identification of Novel Reference Genes Suitable for qRT-PCR Normalization with Respect to the Zebrafish Developmental Stage. *PLOS ONE* **11**, e0149277 (2016).

69. McCurley, A. T. & Callard, G. V. Characterization of housekeeping genes in zebrafish: male-female differences and effects of tissue type, developmental stage and chemical treatment. *BMC Mol. Biol.* **9**, 102 (2008).

70. Moreno-Mateos, M. A. *et al.* CRISPRscan: designing highly efficient sgRNAs for CRISPR-Cas9 targeting in vivo. *Nat. Methods* **12**, 982–988 (2015).

71. Jao, L. E., Wente, S. R. & Chen, W. Efficient multiplex biallelic zebrafish genome editing using a CRISPR nuclease system. *Proc. Natl. Acad. Sci. U. S. A.* **110**, 13904–13909 (2013).

72. Varshney, G. K. *et al.* A High-Throughput functional genomics workflow based on CRISPR/Cas9-mediated targeted mutagenesis in zebrafish. *Nat. Protoc.* **11**, 2357–2375 (2016).

73. Burger, A. *et al.* Maximizing mutagenesis with solubilized CRISPR-Cas9 ribonucleoprotein complexes. *Development* **143**, 2025–2037 (2016).

74. Sorlien, E. L., Witucki, M. A. & Ogas, J. Efficient Production and Identification of CRISPR/Cas9-generated Gene Knockouts in the Model System Danio rerio. *JoVE J. Vis. Exp.* e56969 (2018) doi:10.3791/56969.

75. Saint-Amant, L. & Drapeau, P. Time course of the development of motor behaviors in the zebrafish embryo. *J. Neurobiol.* **37**, 622–632 (1998).

76. Glazer, L. & Brennan, C. H. Developmental Exposure to Low Concentrations of Methylmercury Causes Increase in Anxiety-Related Behaviour and Locomotor Impairments in Zebrafish. *Int. J. Mol. Sci.* **22**, 10961 (2021).

77. Dunn, K. W., Kamocka, M. M. & McDonald, J. H. A practical guide to evaluating colocalization in biological microscopy. *Am. J. Physiol. - Cell Physiol.* **300**, C723–C742 (2011).

78. Morrice, J. R., Gregory-Evans, C. Y. & Shaw, C. A. Modeling Environmentally-Induced Motor Neuron Degeneration in Zebrafish. *Sci. Rep.* **8**, 4890 (2018).

79. Mirdita, M. *et al.* ColabFold: making protein folding accessible to all. *Nat. Methods* **19**, 679–682 (2022).

80. Tunyasuvunakool, K. *et al.* Highly accurate protein structure prediction for the human proteome. *Nature* **596**, 590–596 (2021).

81. Mariani, V., Biasini, M., Barbato, A. & Schwede, T. lDDT: a local superposition-free score for comparing protein structures and models using distance difference tests. *Bioinformatics* **29**, 2722–2728 (2013).

82. Griffith, A. R. *et al.* Predicting glycosaminoglycan surface protein interactions and implications for studying axonal growth. *Proc. Natl. Acad. Sci. U. S. A.* **114**, 13697–13702 (2017).

83. Carugo, O. & Pongor, S. A normalized root-mean-spuare distance for comparing protein three-dimensional structures. *Protein Sci. Publ. Protein Soc.* **10**, 1470–1473 (2001).

84. Xu, X. & Zou, X. Dissimilar Ligands Bind in a Similar Fashion: A Guide to Ligand Binding-Mode Prediction with Application to CELPP Studies. *Int. J. Mol. Sci.* **22**, 12320 (2021).

85. Ramírez, D. & Caballero, J. Is It Reliable to Take the Molecular Docking Top Scoring Position as the Best Solution without Considering Available Structural Data? *Mol. J. Synth. Chem. Nat. Prod. Chem.* **23**, 1038 (2018).

86. Pantsar, T. & Poso, A. Binding Affinity via Docking: Fact and Fiction. *Mol. J. Synth. Chem. Nat. Prod. Chem.* **23**, 1899 (2018).

87. Tachoua, W., Kabrine, M., Mushtaq, M. & Ul-Haq, Z. An in-silico evaluation of COVID-19 main protease with clinically approved drugs. *J. Mol. Graph. Model.* **101**, 107758 (2020).

88. Du, X. *et al.* Insights into Protein–Ligand Interactions: Mechanisms, Models, and Methods. *Int. J. Mol. Sci.* **17**, 144 (2016).

89. In Silico Analysis of Forskolin as a Potential Inhibitor of SARS-CoV-2. *Journal of Pure and Applied Microbiology* https://microbiologyjournal.org/in-silico-analysis-of-forskolin-as-a-potential-inhibitor-of-sars-cov-2/ (2021).

90. Strober, W. Trypan Blue Exclusion Test of Cell Viability. *Curr. Protoc. Immunol.* **111**, (2015).

91. Zempleni, J., Galloway, J. R. & McCormick, D. B. Pharmacokinetics of orally and intravenously administered riboflavin in healthy humans. *Am. J. Clin. Nutr.* **63**, 54–66 (1996).

92. Yanagawa, N., Shih, R. N. G., Jo, O. D. & Said, H. M. Riboflavin transport by isolated perfused rabbit renal proximal tubules. *Am. J. Physiol.-Cell Physiol.* **279**, C1782–C1786 (2000).

93. de Marchi, F. O. *et al.* P2X7R and PANX-1 channel relevance in a zebrafish larvae copper-induced inflammation model. *Comp. Biochem. Physiol. Part C Toxicol. Pharmacol.* **223**, 62–70 (2019).

94. Shao, C., Bittrich, S., Wang, S. & Burley, S. K. Assessing PDB macromolecular crystal structure confidence at the individual amino acid residue level. *Structure* **30**, 1385-1394.e3 (2022).

95. Sangar, V., Blankenberg, D. J., Altman, N. & Lesk, A. M. Quantitative sequence-function relationships in proteins based on gene ontology. *BMC Bioinformatics* **8**, 294 (2007).

96. Boon, K.-L. *et al.* Zebrafish survival motor neuron mutants exhibit presynaptic neuromuscular junction defects. *Hum. Mol. Genet.* **18**, 3615–3625 (2009).

97. Hu, Z. -y *et al.* Gene miles-apart is required for formation of otic vesicle and hair cells in zebrafish. *Cell Death Dis.* **4**, e900–e900 (2013).

98. Pais-Roldán, P., Singh, A. P., Schulz, H. & Yu, X. High magnetic field induced otolith fusion in the zebrafish larvae. *Sci. Rep.* **6**, 24151 (2016).
99. Gleason, M. R. *et al.* The transmembrane inner ear (Tmie) protein is essential for normal hearing and balance in the zebrafish. *Proc. Natl. Acad. Sci.* **106**, 21347–21352 (2009).
100. Pickett, S. B. & Raible, D. W. Water Waves to Sound Waves: Using Zebrafish to Explore Hair Cell Biology. *JARO J. Assoc. Res. Otolaryngol.* **20**, 1–19 (2019).
101. Schwarzer, S. *et al.* Neurogenesis in the inner ear: the zebrafish statoacoustic ganglion provides new neurons from a Neurod/Nestin-positive progenitor pool well into adulthood. *Development* **147**, dev176750 (2020).
102. Sheets, L., Holmgren, M. & Kindt, K. S. How Zebrafish Can Drive the Future of Genetic-based Hearing and Balance Research. *J. Assoc. Res. Otolaryngol.* **22**, 215–235 (2021).
103. Filova, I. *et al.* ISL1 is necessary for auditory neuron development and contributes toward tonotopic organization. *Proc. Natl. Acad. Sci.* **119**, e2207433119 (2022).
104. Bordoni, B., Mankowski, N. L. & Daly, D. T. Neuroanatomy, Cranial Nerve 8 (Vestibulocochlear). in *StatPearls* (StatPearls Publishing, 2023).
105. Koleilat, A. *et al.* L-type voltage-gated calcium channel agonists mitigate hearing loss and modify ribbon synapse morphology in the zebrafish model of usher syndrome type 1. *DMM Dis. Models Mech.* **13**, (2020).
106. Zaichikova, A. A., Damjanović, I., Maximov, P. V., Aliper, A. T. & Maximova, E. M. Neurons in the Optic Tectum of Fish: Electrical Activity and Selection of Appropriate Stimulation. *Neurosci. Behav. Physiol.* **51**, 993–1001 (2021).
107. Anichtchik, O. *et al.* Loss of PINK1 Function Affects Development and Results in Neurodegeneration in Zebrafish. *J. Neurosci.* **28**, 8199–8207 (2008).

108. Wang, J. & Cao, H. Zebrafish and Medaka: Important Animal Models for Human Neurodegenerative Diseases. *Int. J. Mol. Sci.* **22**, 10766 (2021).

109. Damier, P., Hirsch, E. C., Agid, Y. & Graybiel, A. M. The substantia nigra of the human brain: I. Nigrosomes and the nigral matrix, a compartmental organization based on calbindin D28K immunohistochemistry. *Brain* **122**, 1421–1436 (1999).

110. Ruchalski, K. & Hathout, G. M. A medley of midbrain maladies: a brief review of midbrain anatomy and syndromology for radiologists. *Radiol. Res. Pract.* **2012**, 258524 (2012).

111. Bill, B. R., Petzold, A. M., Clark, K. J., Schimmenti, L. A. & Ekker, S. C. A Primer for Morpholino Use in Zebrafish. *Zebrafish* **6**, 69–77 (2009).

112. Colombo, E. A. *et al.* A zebrafish model of Poikiloderma with Neutropenia recapitulates the human syndrome hallmarks and traces back neutropenia to the myeloid progenitor. *Sci. Rep.* **5**, 15814 (2015).

113. Stainier, D. Y. R. *et al.* Guidelines for morpholino use in zebrafish. *PLoS Genet.* **13**, e1007000 (2017).

114. Braems, E. *et al.* HNRNPK alleviates RNA toxicity by counteracting DNA damage in C9orf72 ALS. *Acta Neuropathol. (Berl.)* **144**, 465–488 (2022).

115. Ray, M. K. *et al.* CAT7 and cat7l Long Non-coding RNAs Tune Polycomb Repressive Complex 1 Function during Human and Zebrafish Development. *J. Biol. Chem.* **291**, 19558–19572 (2016).

116. Morcos, P. A., Vincent, A. C. & Moulton, J. D. Gene Editing Versus Morphants. *Zebrafish* **12**, 319 (2015).

117. Rossi, A. *et al.* Genetic compensation induced by deleterious mutations but not gene knockdowns. *Nature* **524**, 230–233 (2015).

118. Buglo, E. *et al.* Genetic compensation in a stable slc25a46 mutant zebrafish: A case for using F0 CRISPR mutagenesis to study phenotypes caused by inherited disease. *PLoS ONE* **15**, e0230566 (2020).

119. Cavodeassi, F. & Wilson, S. W. Looking to the future of zebrafish as a model to understand the genetic basis of eye disease. *Hum. Genet.* **138**, 993–1000 (2019).

120. El-Brolosy, M. A. & Stainier, D. Y. R. Genetic compensation: A phenomenon in search of mechanisms. *PLoS Genet.* **13**, e1006780 (2017).

121. Chaya, S. *et al.* The First Case of Riboflavin Transporter Deficiency in sub-Saharan Africa. *Semin. Pediatr. Neurol.* **26**, 10–14 (2018).

122. Jusko, W. J. & Levy, G. Absorption, Metabolism, and Excretion of Riboflavin-5′-phosphate in Man. *J. Pharm. Sci.* **56**, 58 (1967).

123. Nath, A. K. *et al.* Chemical and metabolomic screens identify novel biomarkers and antidotes for cyanide exposure. *FASEB J.* **27**, 1928–1938 (2013).

124. Gusso, D. *et al.* Pannexin channel 1, P2×7 receptors, and Dimethyl Sulfoxide mediate pain responses in zebrafish. *Behav. Brain Res.* **423**, 113786 (2022).

125. de Marchi, F. O. *et al.* P2X7R and PANX-1 channel relevance in a zebrafish larvae copper-induced inflammation model. *Comp. Biochem. Physiol. Toxicol. Pharmacol. CBP* **223**, 62–70 (2019).

126. Bolten, J. S., Pratsinis, A., Alter, C. L., Fricker, G. & Huwyler, J. Zebrafish (Danio rerio) larva as an in vivo vertebrate model to study renal function. *Am. J. Physiol.-Ren. Physiol.* **322**, F280–F294 (2022).

127. Fleming, A., Diekmann, H. & Goldsmith, P. Functional Characterisation of the Maturation of the Blood-Brain Barrier in Larval Zebrafish. *PLOS ONE* **8**, e77548 (2013).

128. Dragojević, J., Mihaljević, I., Popović, M. & Smital, T. Zebrafish (Danio rerio) Oat1 and Oat3 transporters and their interaction with physiological compounds. *Comp. Biochem. Physiol. B Biochem. Mol. Biol.* **236**, 110309 (2019).

129. da Silva, K. M. *et al.* Mass Spectrometry-Based Zebrafish Toxicometabolomics: A Review of Analytical and Data Quality Challenges. *Metabolites* **11**, 635 (2021).